REFERENCE ONLY

UNIVERSITY OF LONDON THESIS

Degree PhD Year 2007 Name of Author WU, Wei

Exchange calculations between donors in silicon and metal-phthalocyanine dimer

Wei Wu

Department of Physics and Astronomy
University College London

Thesis submitted for the degree of Doctor of Philosophy
Supervisors: Andrew J. Fisher and Anthony H. Harker

July 17, 2007

ProQuest LLC
789 East Eisenhower Parkway
P.O. Box 1346
Ann Arbor, MI 48106-1346

ABSTRACT

This thesis describes the calculation of exchange interactions for systems of electrons, and their potential uses for quantum information processing. The first part treats exchange between donor impurities (including especially deep donors) in silicon, while the second describes exchange in copper and manganese phthalocyanines.

Part I uses the quantum defect method and a model central-cell correction to evaluate the exchange interaction between two deep donors by a Heitler-London-type approach. This part also describes calculations of the exchange in a three-donor complex, where one donor plays the role of a 'control atom' whose optical excitation switches the coupling strengths, and the other two are qubits embodying the quantum information. Variational calculations are described which give the control electron freedom to reside on different parts of the complex; it is found that the exchange between two qubits is increased when the control electron becomes delocalized, and that it is possible for the exchange to become ferromagnetic. These observations are rationalised in terms of multi-centre exchange processes using Green's function perturbation theory.

In Part II, exchange interactions between copper(II) phthalocyanine (Cu(II)Pc) and manganese (II) phthalocyanine dimers (Mn(II)Pc)are described; these systems have both long excited-state lifetimes and tunable magnetic properties. The theoretical studies described include both a model Green's function calculation, to understand the roles of the competing exchange processes, and *ab initio* density functional theory calculations. The model calculations of Cu(II)Pc show that the dominant contribution comes from so-called indirect exchange, and depends strongly on the stacking angle. The magnitude of the exchange interaction from the *ab initio* calculations of Cu(II)Pc roughly agrees with the experiment.

CONTENTS

Part I

EXCHANGE COUPLINGS AMONG DONORS IN SEMICONDUCTORS

1. INTRODUCTION

1.1 Quantum Information Processing

On the atomic scale matter obeys the rules of quantum mechanics, which are quite different from the classical rules that determine the properties of conventional logic gates. So if computers are to become smaller in the future, quantum technology must in any case replace or supplement what we have now. But there is also a second, more radical, change possibly using quantum mechanics: a quantum system can support an entirely new kind of computation with qualitatively new algorithms based entirely on quantum principles. Among other changes, this involves replacing the 'bit' as a carrier of classical binary information (0 or 1) by the quantum bit or 'qubit', which can exist in the arbitrary superposition state $\alpha|0\rangle + \beta|1\rangle$.

Quantum computation is very promising because it is efficient in a number of specific applications, for example, factorizing very large integers [1]. It is also closely related to quantum *communication*, which allows — for example — the unconditionally secure exchange of ordinary (classical) information, or the 'teleportation' of an unknown quantum state. But the implementation of quantum computation is extremely difficult. In the past ten years many diverse proposals have been made for the implementation of quantum computation. The first quantum algorithms were implemented using nuclear spins as qubits [2, 3, 4] and one of the most successful current technologies is the ion trap [5, 6]. There are some clear advantages in using nearly isolated ions or atoms as qubits, possibly combining them with some form of solid-state technology in the form of an 'atom chip' in which atoms or ions are trapped close to a solid-state system which provides optics, control electrodes etc [7]. But there has also been growing interest in the possibility of all-solid-state approaches, using a range of possible qubits from nuclear spins [8], to the charge degrees of freedom of double quantum dots [9, 10].

1.2 Proposals for solid-state quantum information processing

1.2.1 The Di Vincenzo Checklist

A successful quantum computer has to satisfy the well-known 'DiVincenzo checklist' [11]. David DiVincenzo's list was an attempt to enumerate the tests that any proposal for performing quantum information process would have to pass before it could be considered credible. The requirements are:

1. a well-defined Hilbert space within which the quantum information can be represented (typically in form of a number of two-level qubits);
2. a means of preparing pure states within this set;
3. a means of performing arbitrary unitary transformations on the states of qubits (typically by implementing arbitrary single-qubit operations and at least one type of non-trivial two-qubit operation);
4. avoiding decoherence for long enough to compute;
5. some means of reading out the state of qubits at the end of the calculation.

Some of the proposals reached the point of demonstrating the coherent motion of individual quantum bits although that is extremely challenging. According to the type of excitation used for the qubits we can classify these solid-state proposals:

1.2.2 Collective excitations: qubits in superconductors

The many-electron wavefunction in a superconducting structure provides several degrees of freedom which can be used to embody quantum information.

- The number of superconducting electrons can be used as the qubit variable (a 'charge qubit'). A structure which uses this idea is the 'Cooper pair box', in which one part of the material is weakly coupled to the rest and can be placed in a superposition of occupation-number states [12, 13].
- The magnetic flux through a superconducting circuit (typically a ring containing a weak link), can be used for the qubit [14].
- Finally the quantum-mechanical phase difference between parts of a superconducting circuit (for example, across a Josephson junction), and the resulting current flow, can be used to define the qubit [14, 15, 16].

Considerable progress has been made in all three implementation types. Coherent evolution of a Cooper-pair box was originally demonstrated by Nakamura *et al.* [12]; greatly enhanced decoherence times were then obtained by operating the qubit near a saddle-point in the energy surfaces, so that it was decoupled (to first order) from electromagnetic fluctuations in its environment [13]. Indirect evidence for the achievement of a two-qubit gate operation was provided by Yamamoto [17], although at that stage without full characterization of the final state. An important step forward in achieving high-fidelity single-shot readout from phase qubits was made by Katz *et al.* [16], who also studied through detailed tomography the evolution of the qubit state during the measurement. Most recently, the same group [15] demonstrated entanglement of two phase qubits through full state tomography.

1.2.3 Double quantum dots

Quantum dots are another promising approach to implement quantum computation. In 2003, Hayashi *et al.* [10] demonstrated in the time domain the coherent oscillation of an electron between two adjacent quantum dots. They proposed that if quantum information is carried by the charge distribution in the double-dot system, this process could be used to implement single-qubit operations. The qubit could be manipulated using high-speed voltage pulses, and its state read out by current measurements. However, the observed decoherence time was only slightly longer than the oscillation time.

Recently, the research group led by Marcus [18] not only considered the situation where a single electron occupies the double quantum dot, but also examined double-occupancy. In the single-qubit situation they use a microwave field to manipulate the qubit (by contrast to the high-speed voltage pulse used in [10]), and in the two-electron situation they measure the singlet-triplet relaxation rate of different charge configurations—information that is very important for readout and initialization.

1.2.4 Qubits based on nuclear spin

The best developed proposal for a solid-state nuclear spin quantum computer comes from Kane [8]. This envisages depositing phosphorus (P) nuclei near the surface of an isotopically pure Si crystal. The quantum information is supposed to be carried by the nuclear spins, and can be manipulated by a combination of an external magnetic field and the hyperfine interaction with the shallow donor electron state associated with the P impurity.

Recently, Clark's group [19] has been using two controlled implanted phosphorus atoms in silicon to implement quantum computation; a positional accuracy of 20 nm

was achieved. Similar to the quantum computation scheme, implemented by double quantum dots an electron can transfer from one impurity to another. The charge state of these two impurities controlled by the external voltage carries the quantum information. They have demonstrated gate-controlled charge transfer event and tried to exploit this controlled implantation technique to implement quantum computation.

1.2.5 *Qubits based on electron spins*

An alternative qubit is the electron spin; since the Bohr magneton is much larger than the nuclear magneton ($\mu_B/\mu_N = m_p/m_e$) where m_e, m_p are respectively the mass of an electron and a proton, and μ_B, μ_N are respectively Bohr magneton and proton magneton. Electron spins can be manipulated in electron paramagnetic resonance experiments much more rapidly than nuclei in Nuclear Magnetic Resonance (NMR). However, the decoherence times are also faster. One of the first among such proposals was to use electron spins at quantum dots [20] as qubits, and couple them by the effective exchange interaction.

Another family of proposals use the electron spins in molecular cages for the qubits; one promising candidate is the endohedral fullerene species $N@C_{60}$; the $\frac{3}{2}-$spin state associated with N atom which has a long relaxation time due to nearly isolation from the environment by the fullerene 'cage' [21].

An alternative approach exploits mobile electrons. An electron can be trapped within defined semiconductor quantum wires by the potential wells, and it is possible to do two-qubit operations by making the wires close enough to allow exchange to occur [22].

1.3 *Proposal for optically controlled gates in silicon*

Among the above proposals using the solid state, silicon-based quantum computer architectures have attracted attention because of their promise for scalability and their potential for using the available resources associated with the existing infrastructure of the powerful Si technology [40]. In pure Si, electron spins are associated only with defects and so are naturally isolated, therefore localized spins in Si are a very promising means to represent quantum information. Furthermore, implementing quantum gates requires producing interactions between localized spins in order to evolve these spin states. Previous approaches to control spin-spin interactions [8, 20] required gate electrodes positioned either near to specific, highly polarizable defects, which are readily ionized except at low temperatures, or close to specially

fabricated quantum-dot structures. The presence of the gates, and other interactions with the polarizable defects, may introduce significant sources of decoherence.

Stoneham *et al.* [23] by contrast propose a novel scheme for controlling interaction which avoids the electrodes; interactions are instead controlled by electronic excitation [24]. Quantum bits are encoded into electron spins of deep donors, for example Si:B which has an electron binding energy of 71 meV compared to 46meV for Si:P. Let (A,B) be two such deep donor atoms; their spacing should be sufficiently large that the ground-state interaction between donor spins is small (ideally negligible). A typical spacing between two deep donors to achieve this would be perhaps 7-10 nm for Si:Bi. Controlled optical excitation [25, 26] promotes a 'control' electron from a nearby impurity T, possibly Er or a shallow donor such as P, into an excited state that is to some extent delocalized across A, B and T and may even have 'molecular' character. In this excited state, there is an effective interaction induced between the qubit spins. Qubit-qubit interactions are therefore switched on by optical excitation and off by (stimulated) de-excitation of control electron.

This approach has two key requirements. First, the spin encoding the quantum information must have an acceptable lifetime. Second, there must be an electronic excited state in which the coupling between spins is changed significantly to produce entangling gates, and this excited state must be sufficiently long-lived that decay (though spontaneous emission or non-radiative processes) is very unlikely to occur during gate operations.

If these requirements can be met there are two main benefits in this scheme. First, ground-state quantum information storage is largely separated from excited-state information control. Second, if we choose a control system whose excitation energy is large, no small energy scale is involved in the gate operation. In other words, it might operate at liquid nitrogen temperatures or even near room temperature. Third, the fabrication requirements are much less stringent than for a scheme such as those described in [8, 10], since no electrode fabrication is required.

This scheme of gates may be made to satisfy the DiVincenzo's checklist due to the following reasons:

- *Defined Hilbert space to represent the quantum information.*

  $\frac{1}{2}$–spin provides a well-defined Hilbert space. Compared to shallow donors, it is even harder for deep donor electrons to be excited to the conduction band and get out of the Hilbert space.

- *Initialization of qubits.*

  The spin-injection and polarization selective optical pumping are accessible

initialization methods [27, 28].

- *Manipulation of quantum information.*

  For universal quantum computation, it is sufficient to realize arbitrary single-qubit gate and any non-trivial two-qubit gates such as control-NOT gate [1]. The single-qubit gate can be realized by confocal optical and magnetic resonance. If the control electron is excited to a suitable state, in some accessible region of physical parameters of magnetic field and control excited states the two-qubit manipulation can be done as described in [23].

- *Avoiding decoherence.*

  Our scheme avoids the electrodes, so the main decoherence source comes from the spin-lattice relaxation. However, older data [29, 30] shows that deeper donors than Si:Bi are desirable for the high-temperature manipulation.

- *Readout scheme.*

  Supposing we use qubits 0 to n in the computation, and we also introduce one additional qubit labeled -1. Let c_{ij} be the control atom connecting qubits q_i and q_j. After computation, all control atoms are in state $|0\rangle$. Suppose we can arrange that q_{-1} which takes no part in the computation is also in the state $|0\rangle$. Now tune the c_{-10} laser to be resonant between the $|000\rangle_g$ ground state of the full system $q_{-1} - c_{-10} - q_0$ and the excited state $|000\rangle_e$ and off resonance with transitions between other spin ground and excited states, and operate it continuously. Rabi oscillations will occur between these two states if and only if q_0 is in the state $|0\rangle$, and scattered photons produced by spontaneous emission when the system is in its excited state will be observed. If photons are observed, q_0 is in $|0\rangle$; if not, q_0 is in $|1\rangle$. If q_0 is in $|0\rangle$, the we can use c_{01} to read q_1, however, if not, we can first flip c_{01} to $|1\rangle$ and read q_1 by using the above scheme.

- *Advantage of Disorder*

  This scheme takes advantage of the ease of arranging disordered deep donors. Disorder makes the excitation energies different from one pair of donors to another since spacing and orientation relative to the host cystallographic axis will differ. We then are able to use spectroscopic resolution and spatial resolution to control a particular pair.

1.4 Overview of Part I

In the second chapter we will begin by introducing effective-mass theory, which gives a simple description of electrons bound to donors but only works for shallow donors. To get around this limitation we introduce a novel combination of the quantum defect method and a simple central-cell correction, thereby obtaining a better wave function for deep donors. Based on the Gaussian fitting of these wave functions, we can calculate the exchange interaction between two donors having arbitrary binding energies. This enables us to relate quantitatively the likely gate timescales to the concentration and distribution of the defects.

Having calculated the two-donor exchange in silicon, in the third and fourth chapters we turn to a more complicated case, the so-called control-qubit system where a third (control) atom is present in addition to the two qubits. In order to describe the excited states of this complex, and their magnetic properties, we perform a variational calculation in which the control electron is given the freedom to delocalize over these three atoms. Although this freedom is limited by the small basis set we use, the calculation illustrates the physics controlling the exchange interaction between donors as a function of the relative energies of the states involved.

Following these calculations of donor exchange, in the fifth chapter I describe an investigation of the random distribution of donors, because the atomic positions cannot be controlled precisely and the realistic environment of the control-qubit system will inevitably contain a random element. In particular, I calculate the distributions of the first- and second-nearest neighbour distances and the corresponding exchange and dipolar interactions. In order to understand the effect the environment has on the control-qubit system, in the sixth chapter we calculate the time evolution of a small group of spins which includes the control-qubit system and a spectator spin.

Spin readout is a particularly important and challenging area for spin-based quantum computation, owing to the extreme difficulty of single-spin detection. The readout scheme proposed in [23] is optical: it relies on finding a spin-dependent optical transition which can be resonantly excited, the number of fluorescence photons observed being used as an indication of the spin state. The final chapter of Part I describes an analysis of this readout process, by solving for the density matrix of the spin states in the presence of the laser flux.

2. EFFECTIVE MASS THEORY, MODEL CENTRAL CELL CORRECTION, AND THE CALCULATION OF DONOR EXCHANGE

2.1 Introduction

In this chapter first we introduce effective mass theory [31, 32] which is a very good approximation of shallow donors, but effective mass theory has the principal limitation for treating the deep donors in semiconductors.

In order to improve the treatment of deep donors we consider the quantum defect method [34]. In the sense that the anisotropy of the effective mass equation is neglected this method gives us a better wave function of donor electrons [34]. Using the quantum defect method one can include the information about the defect chemical nature into effective mass equation.

The solutions (radial functions) of the isotropic effective mass equation in the quantum defect method are regular far from the donor center, but divergent near the donor centre when $\nu \neq$ integer where ν is associated with the single-defect energy level,i.e., $E_\nu = -\frac{1}{2\nu^2}$, so we have to perform a central cell correction to make the radial functions regular at the center of defects. What we do is to model the potential near the center of the donor atom, i.e., choose a δ-potential or a square-well potential which is near the core of donor atom. By performing model central cell correction, we can find the eigenfunction of the isotropic effective mass equation in the whole space. As long as we know the eigenfunctions of the isotropic effective mass equation, we can use them to calculate the Heitler-London exchange couplings between shallow/deep donor electrons.

2.2 Introduction to Effective mass theory

Effective mass theory [31, 32] is a tool to solve the problem of impurity states in semiconductors. In effective mass theory a mass tensor, the elements of which are determined by the unperturbed band structure, replaces the effect of the periodic field. The effective-mass equation for impurity states is particularly well adapted to discussing impurity states in semiconductors, e.g., silicon. Luttinger *et al.* [31] and

Kittel *et al.* [32] derived the effective mass equation in the 1950s. Here we follow Luttinger's derivation [31]. Let's first introduce the basic problem effective mass theory aimed to solve. If we adopt the notation in Luttinger's paper [31], in the unperturbed periodic field one has

$$H_0\psi_{n\vec{k}} = \epsilon_n(\vec{k})\psi_{n\vec{k}} \tag{2.1}$$

$$\psi_{n\vec{k}} = e^{i\vec{k}\cdot\vec{r}}u_{n\vec{k}}, \tag{2.2}$$

$$u_{n\vec{k}}(\vec{r}+\vec{R}) = u_{n\vec{k}}(\vec{r}) \tag{2.3}$$

where n is the band index, and all $\vec{R}$ are in the Bravais lattice. Let U be the additional potential due to the impurity. The aim of effective mass theory is to solve the Schrödinger equation

$$(H_0 + U)\psi = \epsilon\psi. \tag{2.4}$$

After solving equation (2.4) one can find the impurity state ψ and the eigenvalue ϵ. In effective mass theory, the basic assumption is that U is slowly-varying, i.e., the change in U across any unit cell should be small although U may be large.

First, one can consider the relatively simple case where the conduction band has a non-degenerate minimum is at $\vec{k} = 0$. Because u_{n0} provide a complete set for functions having the periodicity of the lattice,

$$P_{n\vec{k}} = e^{i\vec{k}\cdot\vec{r}}u_{n0} \tag{2.5}$$

form a complete orthogonal set. So we have

$$\langle P_{n\vec{k}}|P_{n'\vec{k}'}\rangle = \delta(\vec{k}-\vec{k}')\delta_{nn'} \tag{2.6}$$

$$\psi = \sum_{n'}\int d\vec{k}' A_{n'}(\vec{k}')P_{n'\vec{k}'}. \tag{2.7}$$

If one expands and substitutes into equation (2.4), and assumes that U is so slowly-varying that its Fourier components outside the first Brillion zone can be neglected, equation (2.4) is changed to the form of:

$$(\epsilon_n + \frac{k^2}{2m})A_n(\vec{k}) + \sum_{n\neq n'}\frac{k_\alpha p^\alpha_{nn'}}{m}A_{n'}(\vec{k}) + \int d\vec{k}' U(\vec{k}-\vec{k}')A_n(\vec{k}') = \epsilon A_n(\vec{k}). \tag{2.8}$$

In equation (2.8), a summation over $\alpha = x, y, z$ is implied.

$$p^\alpha_{nn'} = \frac{(2\pi)^3}{\Omega}\int_{cell} u^*_{n0}(\frac{1}{i}\nabla_\alpha)u_{n'0}d\vec{r} \tag{2.9}$$

$$U(\vec{k}) = \frac{1}{(2\pi)^3}\int d\vec{r}e^{-i\vec{k}\cdot\vec{r}}U(\vec{r}). \tag{2.10}$$

The $p^{\alpha}_{nn'}$'s are just the momentum matrix elements at the bottom of the band, Ω is the volume of the unit cell and $U(\vec{k})$ is the Fourier transform of U.

Equation (2.8) contains the inter-band couplings, and those couplings cause trouble. In order to remove the inter-band couplings Luttinger and Kohn introduced a canonical transformation T:

$$A_n(\vec{k}) = \sum_{n'} \int d\vec{k'} \langle n\vec{k}|T|n'\vec{k'}\rangle B_{n'}(\vec{k'}). \tag{2.11}$$

After higher-order terms and the inter-band terms which are small are neglected, equation (2.8) changes to the form of

$$\epsilon_n(\vec{k})B_n(\vec{k}) + \int U(\vec{k}-\vec{k'})B_n(\vec{k'})d\vec{k'} = \epsilon B_n(\vec{k}), \tag{2.12}$$

where it is understood that $\epsilon_n(\vec{k})$ is to be expanded to second order in $\vec{k}$. Here we can see that there are no inter-band terms. Equation (2.12) is the well-known effective mass equation in 'momentum space'. Going back from 'momentum space' to 'coordinate space', equation (2.12) becomes

$$[\epsilon_n(-i\nabla) + U(\vec{r})]F_n(\vec{r}) = \epsilon F_n(\vec{r}), \tag{2.13}$$

$$F_n(\vec{r}) = \int e^{i\vec{k}\cdot\vec{r}} B_n(\vec{k})d\vec{k}, \tag{2.14}$$

the integration being over the first Brillouin zone.

At the end, the effective mass equation reads

$$[\epsilon_n(-i\nabla) + U(\vec{r})]F_n(\vec{r}) = \epsilon F_n(\vec{r}), \tag{2.15}$$

$$\psi = \sum_n F_n(\vec{r})\psi_{n0}(\vec{r}). \tag{2.16}$$

Especially for states located near to a particular band, only one term of the sum in (2.16) is needed,

$$\psi = F(\vec{r})\psi_c(\vec{r}). \tag{2.17}$$

For a band where the minimum is not at the center, the result will again be that

$$\psi = \sum_n F_n(\vec{r})\psi_{n\vec{k}_0}(\vec{r}), \tag{2.18}$$

where now F_n is a solution of the modified effective mass equation

$$[\epsilon_n(\vec{k}_0 + \frac{1}{i}\nabla) + U]F_n = \epsilon F_n. \tag{2.19}$$

As always, it is intended that ϵ_n be expanded around $\vec{k}_0$ to second order terms in $(1/i)\nabla$.

2.2.1 Donors in silicon

The silicon band structure was extensively studied experimentally and theoretically. There are six equivalent minima in the conduction band structure of Si: $(\pm k_0, 0, 0)$, $(0, \pm k_0, 0)$, $(0, 0, \pm k_0)$, where $k_0 = 0.85 \times \frac{2\pi}{a}$, and a is the lattice constant of silicon. The conduction-band energy near the minimum point $\vec{k}^{(i=5)} = (0, 0, k_0)$ is

$$E = E_0 + \frac{\hbar^2}{2m_1}(k_z - k_0)^2 + \frac{\hbar^2}{2m_2}(k_x^2 + k_y^2), \tag{2.20}$$

where index $i = 1, 2, ..., 6$ in $\vec{k}^{(i)}$ refers to $\pm x, \pm y, \pm z$, there is similar conduction band energy near the other band minima. Choosing the donor ion as the coordinate origin, for large r,

$$U(\vec{r}) = -e^2/\kappa r, \tag{2.21}$$

where κ is the dielectric constant of Si, having the value 11.4. Here we use the true atomic unit in which $\hbar = 1$. Because of the large reduction of Coulomb field of the donor ion, one expects bound states around the donor having dimensions large compared with lattice spacing. In this limit we should say that [33] the solutions of equation (2.4) are

$$\psi^{(i)}(\vec{r}) = F^{(i)}(\vec{r})\psi(\vec{k}^{(i)}, \vec{r}), i = 1, 2, ..., 6, \tag{2.22}$$

where $\psi(\vec{k}^{(i)}, \vec{r})$ is the Bloch wave function at the minimum $\vec{k}^{(i)}$. The $F^{(i)}(\vec{r})$ satisfy the effective mass equations,

$$[-\frac{1}{2m_1}\frac{\partial^2}{\partial^2 z_i} - \frac{1}{2m_2}(\frac{\partial^2}{\partial^2 x_i} + \frac{\partial^2}{\partial^2 y_i}) - e^2/\kappa r - \epsilon]F^{(i)}(\vec{r}) = 0 \tag{2.23}$$

where $z^{(i)}$ describes motion parallel to $\vec{k}^{(i)}$, and $m_1 = 0.98m_e, m_2 = 0.19m_e$ [33], where m_e is the free electron mass. ϵ is the energy of state (2.22) relative to the conduction band minimum.

In the simplest theory, the effective mass tensor is replaced by a single averaged effective mass m^*,i.e.,

$$[-\frac{\hbar^2}{2m^*}\nabla^2 - \frac{e^2}{\kappa r} - \epsilon]F(\vec{r}) = 0. \tag{2.24}$$

Here we ignore the anisotropy of the effective mass equation. In fact, this is the starting point of the quantum defect method as we discuss later.

Equation (2.23) is difficult to solve exactly. Luttinger and Kohn [32, 33] introduced a variational ansatz which gives a good approximation to the ground state. In the Kohn-Luttinger variational form, F has the form of

$$F^v_{\pm z_i} = \frac{1}{\sqrt{\pi a^2 b}} e^{-[(\frac{(x_i^2+y_i^2)}{a^2} + \frac{z_i^2}{b^2})^{\frac{1}{2}}]}, etc. \tag{2.25}$$

Here a and b are the variational parameters determined by the variational calculation. For silicon $a = 25.09\mathring{A}, b = 14.43\mathring{A}$ [40]. The Kohn-Luttinger variational form is remarkably good in the limit $m_2 \ll m_1$. But in silicon where $m_2/m_1 \simeq 0.19$ there is a significant energy difference between the energy calculated by Kohn-Luttinger variational form which is -0.029eV and the experimental value -0.044eV. This energy difference is due to two reasons: first, the effective mass formalism fails near the donor atom; secondly, the Kohn-Luttinger variational form may not be good enough.

In the effective mass theory, the Schrodinger equations have six equivalent degenerate solutions of the form (2.22). These wave functions form a basis for a representation, say $(1s)$ of the symmetry group of the system, tetrahedral group, T_d. The six wave functions under the operation of T_d behave like $x, -x, y, -y, z, -z$. This representation is reducible, so we can discompose it into the direct sum of irreducible representations of T_d while recombinating the six basis functions. After calculating the character table [33], we can see that

$$(1s) = A_{1g} \oplus E_{1g} \oplus T_{1u}. \tag{2.26}$$

Meanwhile,

$$\alpha_0 = \frac{1}{\sqrt{6}}(1,1,1,1,1,1) \tag{2.27}$$

belongs to the representation A_{1g},

$$\alpha_1 = \frac{1}{\sqrt{12}}(1,1,1,1,-2,-2) \tag{2.28}$$

$$\alpha_2 = \frac{1}{2}(1,1,-1,-1,0,0) \tag{2.29}$$

belongs to the representation E_{1g}, and

$$\alpha_3 = \frac{1}{\sqrt{2}}(1,-1,0,0,0,0) \tag{2.30}$$

$$\alpha_4 = \frac{1}{\sqrt{2}}(0,0,1,-1,0,0) \tag{2.31}$$

$$\alpha_5 = \frac{1}{\sqrt{2}}(0,0,0,0,1,-1) \tag{2.32}$$

belongs to the representation T_{1u}. The six functions (2.22) obtained in the effective mass theory are degenerate. In reality this degeneracy will be partially lifted by the inter-valley effect and one singly-, one doubly, one triply degenerate level will be produced.

2.2.2 Limitation of effective mass theory

Effective mass theory is a very good approximation to shallow donor wave functions, but there are several limitations in effective mass theory as follows:

- The assumption that the perturbing potential U is slowly-varying. This is not true for most deep donors. In addition, the potential near the donor atom centre is complicated and difficult to determine, so the effective mass formalism fails in the vicinity of the defect atom. [33]

- The effective mass equation does not contain any information about the chemical nature of defects. So the energies of impurity states calculated by effective mass theory are the same for all the defects. This is not true; experimentally determined binding energies for single donors in Si range from about 0.04eV to 0.07eV [25].

- Effective mass theory treatment of shallow donors is successful because the energy region within the effective mass theory is comparable with the energy level of shallow donors, and the donor electron spends much time far from the donor central region because a shallow donor electron is relatively more delocalized and the central-region potential has less effect on it. But the energy level of deep donors is lower which is not comparable with the energy region effective mass theory can reach. And contrary to the shallow donors, electrons bound to deep donors spend much time near the donor central region and are sensitive to the central-region potential.

2.3 Quantum defect method, Whittaker function

The Luttinger-Kohn variational forms of donor wave function in effective-mass theory are believed to be very good approximations to states of shallow donors. However, there are several limitations we have cited as in the last section. In addition, the effective mass theory is insensitive to the particular Group III acceptor or Group V donor. [34] It cannot account for the differences in the optical properties between B, Al, Ga, and In in silicon, or for the existence of deep donors. Bebb [34] employed the quantum defect method to obtain better approximate wave functions for impurity centers in semiconductors than had previously been available. Even in the simplest approximation assuming isotropic energy surface, the quantum defect methods provides quantitative results giving good approximations to both the observed spectral dependence and magnitude of the photo-ionization cross section. An essential feature of the quantum defect method is that good approximate wave

functions valid in the region outside the impurity ion core can be determined using only a knowledge of the energy eigenvalues.

Let's first recall the simplest effective mass equation (2.24). Rather than attempting to solve equation (2.24) as an eigenvalue equation to determine the allowed spectrum of ϵ, this equation is considered valid for large r only and solved for the asymptotic form of the wave functions $F(\vec{r})$ corresponding to the empirical value of the energy, ϵ. So another better property of the quantum defect method is that we can find the donor wave functions associated with observed energy levels. But using the effective mass theory we only can describe shallow donors.

The application of the quantum defect method to impurity states in semiconductors is entirely analogous to the development of the quantum defect method in free atoms with a single outer electron. The atomic units appropriate to the solid-state problem are used.

- Effective Bohr radius, $a_0^* = \hbar^2\kappa/(m^*e^2) \approx 1.7$ nm.
- Effective Hartree, $\mathrm{Ha}^* = e^2/(\kappa a_0^*) \approx 0.33$ eV.

In these units, the radial part of equation (2.24) is

$$(\frac{1}{2}\frac{d^2}{dr^2} - \frac{l(l+1)}{2r^2} - u(r) + \epsilon)P(r) = 0. \tag{2.33}$$

Here $P(r) = rR(r)$, and $R(r)$ is the radial part of the wave function. In the region outside the impurity ion core where the potential approaches $u(r) \sim -1/r$, equation (2.33) is conveniently written as

$$(\frac{1}{2}\frac{d^2}{dr^2} - \frac{l(l+1)}{2r^2} - u(r) - \frac{1}{2\nu^2})P(r) = 0, \tag{2.34}$$

where $-\frac{1}{2\nu^2}$ is just ϵ, the observed energy level. Since the energy is not in general an eigenvalue of the differential equation, the solution that is regular at infinity may diverge at the origin. However, this does not affect the validity of the solution far away from the origin. In the next section we will introduce how we do the model central cell correction to find the solution valid in the whole range of r.

For the negative energy, discrete states($-1/\nu^2 < 0$), the most useful form of the solution is a multiple of the well-known Whittaker function $W_{\nu,l+\frac{1}{2}}(2r/\nu)$. The Whittaker function is just a particular linear combination of two standard linearly independent confluent hypergeometric functions. The correct linear combination is determined by the quantum defect parameter, ν, defined at the eigenvalues ϵ_n (experimentally determined) by $\mu(\epsilon_n) = n - \nu$, where n is the usual principal quantum number and

$$\epsilon_n = -\frac{1}{2\nu^2} = -\frac{1}{2(n-\mu(\epsilon_n))^2}. \tag{2.35}$$

The quantum defect function, including the correct normalization, is then

$$P_{\nu,l}(r) = N_{\nu,l} W_{\nu,l+\frac{1}{2}}(2r/\nu). \tag{2.36}$$

Here W is a Whittaker function defined as

$$W_{\kappa,\mu}(z) = e^{-z/2} z^{1/2+\mu} U(\frac{1}{2} - \kappa + \mu, 1 + 2\mu, z), \tag{2.37}$$

where U is the hypergeometric function. For S-symmetry states, the normalization constant $N_{\nu,0}$ is approximately $(2/\nu)^{\nu}/(\nu^{3/2}\Gamma(\nu))$. In Figure (2.1) we plot $P_{1.0,0}/r$ and the radial part of the $1s$ hydrogenic state and show that these two functions are identical. Similarly in Figure (2.2) we plot $P_{1.1,0}/r$ and the radial part of the $1s$ hydrogenic state. Note how the Whittaker-function solution is regular at infinity but diverges at the origin. This is because $\nu = 1.10$ does not correspond to an eigenvalue of (2.34).

Now we have found the solutions of the single-impurity Hamiltonian far from the origin for a given energy (or ν value); next, we will consider how the Hamiltonian in the central region needs to be modified in order to obtain a solution that is valid everywhere.

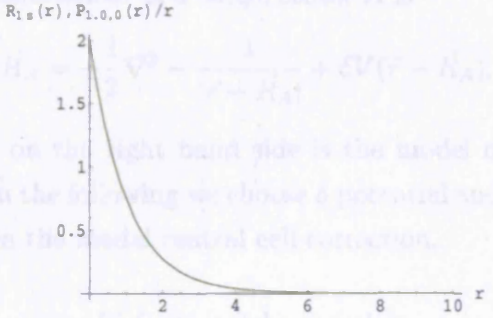

Fig. 2.1: The radial part of the wave function as a function of radius r in the case where $\nu = 1$. The radial part of A hydrongenic $1s$ state is plotted for comparison but the curves cannot be distinguished. Red line:$P_{1.0,0}(r)/r$; green line: the radial part of a Hydrogenic $1s$ state.

2.4 Model central cell correction

Due to the divergence of the radial function associated with equation 2.34 for non-integer values of ν, we have to perform a central cell correction. One way to do the central cell correction is trying to describe the potential near the donor centre as

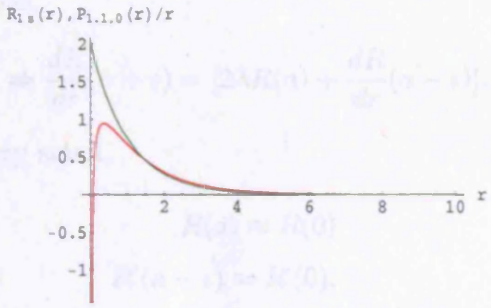

Fig. 2.2: The radial part of the wave function as a function of radius r in the case where $\nu = 1.1$. The radial part of A hydrongenic $1s$ state is plotted for comparison. Notice that the singularity in the red curve as $r \to 0$ occurs because $\nu = 1.10$ does not correspond to an eigenvalue of (2.34). Red line:$P_{1.1,0}(r)/r$; green line:the radial part of a Hydrogenic $1s$ state.

well as we can, while the other way is to alter the Hamiltonian in the region near the origin in order to make the solution regular there at the experimentally observed energy eigenvalue. We call the second way the model central cell correction. A simple form for the Hamiltonian of a single center A is

$$\hat{H_A} = -\frac{1}{2}\nabla^2 - \frac{1}{|\vec{r} - \vec{R}_A|} + \delta V(\vec{r} - \vec{R}_A), \tag{2.38}$$

where the third term on the right hand side is the model central cell correction, which is not unique. In the following we choose δ potential and square-well potential respectively to perform the model central cell correction.

(i) δ potential correction

Let us choose δV to be a potential 'shell' at radius $r = a$, where a is very small:

$$V(r) = -\frac{1}{r} + \lambda\delta(r - a). \tag{2.39}$$

A δ function of strength λ at a finite $r = a$ introduces discontinuity in the derivative of P such that (for a s-symmetry radial function):

$$-\frac{1}{2}[\frac{dP}{dr}]_{a-\epsilon}^{a+\epsilon} + \lambda P(a) = 0, \tag{2.40}$$

where $P(r) = rR(r)$ with $R(r)$ being the radial function.

$$\frac{dP}{dr} = R + r\frac{dR}{dr}. \tag{2.41}$$

Since $R(r)$ is continuous,

$$\Rightarrow \frac{dR}{dr}(a+\epsilon) = [2\lambda R(a) + \frac{dR}{dr}(a-\epsilon)]. \tag{2.42}$$

If a is chosen to be very small,

$$R(a) \approx R(0) \tag{2.43}$$

$$R'(a-\epsilon) \approx R'(0). \tag{2.44}$$

If we make a Taylor expansion of an s-symmetry radial function around r=0 in the form $R(r) = \alpha + \beta r + \gamma r^2 + ...$, the equation

$$[-\frac{1}{2}\frac{d^2}{dr^2} - \frac{1}{r}\frac{d}{dr} - \frac{1}{r}]R = ER, \tag{2.45}$$

implies that $\alpha = -\beta$, or that

$$R'(0) = -R(0) \tag{2.46}$$

(the cusp condition for a nucleus of charge $Z = 1$).

$$\begin{aligned} \Rightarrow R'(a+\epsilon) &= [2\lambda R(a) + R'(a-\epsilon)] \\ &= (2\lambda - 1)R(a), \end{aligned} \tag{2.47}$$

so we can find an expression for the required λ in terms of the external component of the wave function:

$$\frac{R'(a)}{R(a)} = 2\lambda - 1. \tag{2.48}$$

In the following discussion, we will only consider s-symmetry wave functions. Meanwhile, for $r \leq a$,

$$R(a) \approx R(0) + aR'(0) = R(0)(1-a), \tag{2.49}$$

$$R(r) \approx R(0) + rR'(0) = \frac{1}{1-a}[R(a) - rR(a)] = R(a)\frac{1-r}{1-a}. \tag{2.50}$$

So we have the total wave function:

$$R(r) = \left\{ \begin{array}{ccc} R(a)\frac{1-r}{1-a} & : & r \leq a \\ P_\nu(r)/r & : & r > a \end{array} \right\}. \tag{2.51}$$

In Figure (2.3) we can see the wave functions with central cell correction and without it. Note that the diverging tail of the Whittaker function is cut off for $r < a$.

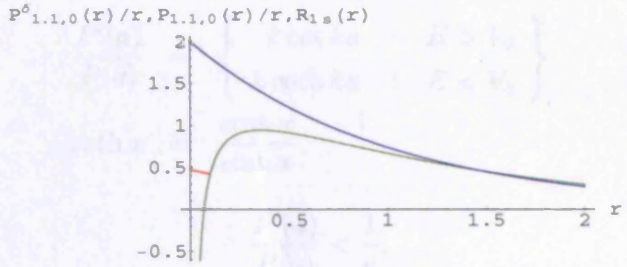

Fig. 2.3: The radial part of Whittaker function $P_{1,1,0}(r)/r$ with δ potential central cell correction (at $a = 0.1$) as a function of radius r. $P_{1,1,0}(r)/r$ and the radial part of a $1s$ Hydrogenic state are also plotted for comparison. Red line: $P^{\delta}_{1,1,0}(r)/r$; green line: $P_{1,1,0}(r)/r$; Blue line: the radial part of a $1s$ hydrogenic state. Notice that with the central cell correction, the diverging tail of the Whittaker function is cut off for $r < a$. The red curve is indistinguishable in the region of $r > a$.

(ii) Square-well potential correction

An alternative matching is to replace a Coulomb potential by a square well, of depth V_0, for $r < a$:

$$V(\vec{r}) = \left\{ \begin{array}{ccc} V_0 & : & r \leq a \\ -\frac{1}{r} & : & r > a \end{array} \right\} \tag{2.52}$$

P satisfies

$$-\frac{1}{2}\frac{d^2P}{dr^2} + V_0 P = EP \tag{2.53}$$

when $r < a$. If $E > V_0$,

$$\Longrightarrow P = A\sin kr + B\cos kr \tag{2.54}$$

$$\frac{1}{2}k^2 = E - V_0;$$

or if $E < V_0$,

$$P = C\sinh kr + D\cosh kr \tag{2.55}$$

$$\tag{2.56}$$

$$\frac{1}{2}k^2 = V_0 - E,$$

$$\sinh x = \frac{e^x - e^{-x}}{2} \tag{2.57}$$

$$\cosh x = \frac{e^x + e^{-x}}{2}. \tag{2.58}$$

The boundary condition $P \to 0$ as $r \to 0$ implies $B = D = 0$. We can find that

$$\frac{P'(a)}{P(a)} = \left\{ \begin{array}{rcl} k\cot ka & : & E > V_0 \\ k\coth ka & : & E < V_0 \end{array} \right\}, \tag{2.59}$$

$$\coth x = \frac{\cosh x}{\sinh x}. \tag{2.60}$$

When

$$\frac{P'(a)}{P(a)} < \frac{1}{a}, \tag{2.61}$$

we must choose $V_0 < E$, so we have a propagating-wave solution for $x < a$:

$$P(r) = \left\{ \begin{array}{rcl} P_\nu(a)\frac{\sin kr}{\sin ka} & : & r \leq a \\ P_\nu(r) & : & r > a \end{array} \right\} \tag{2.62}$$

and the appropriate matching condition at $r = a$ is given by the first line of equation (2.59).

Meanwhile, if

$$\frac{P'(a)}{P(a)} \geq \frac{1}{a}, \tag{2.63}$$

we may match using the second line of equation (2.59), and the wavefunction for $r < a$ is a combination of decaying and growing exponentials:

$$P(r) = \left\{ \begin{array}{rcl} P_\nu(a)\frac{\sinh kr}{\sinh ka} & : & r \leq a \\ P_\nu(r) & : & r > a \end{array} \right\}. \tag{2.64}$$

In Figure (2.4) we compare the wave functions $P_{1.1,0}$ with δ-function central cell correction and square well potential central cell correction, and the wave function $P_{1.1,0}$ without central cell correction is also plotted for comparison. Note that in both cases the diverging tails of the wave function are cut off for $r < a$.

We also calculated the normalization factor of s-symmetry states.

$$N(\nu) = (\int_0^\infty P(\nu, 0, r)^2 dr)^{-\frac{1}{2}}. \tag{2.65}$$

As shown in Figure (2.5) when $\nu \geq 1$ the normalization factor is nearly equal to 1. Here we neglect the contribution to the integration due to the wave function change in the central cell correction region because this region is very small so that the contribution to the whole integration is very little.

2.5 Two-donor Heitler-London exchange calculation

2.5.1 Review of exchange calculations in H_2

The exchange coupling between two electrons in H_2 has been calculated by several groups since the 1920s. In this subsection I will introduce some of the most important approaches to this problem.

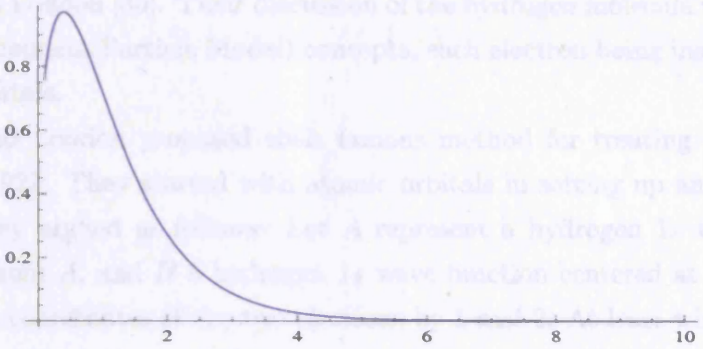

Fig. 2.4: δ potential and square-well potential central cell corrections are presented. Whittaker function $P_{1.1,0}/r$ is also plotted for comparison. Red line:$P^{\delta}_{1.1,0}(r)/r$ with δ potential central cell correction at $a = 0.1$; green line: $P^{sw}_{1.1,0}(r)/r$ with square-well potential central cell correction at $a = 0.1$; Blue line:$P_{1.1,0}(r)/r$. Notice that in both cases the diverging tails of the wave function are cut off for $r < a$, but those curves for $r < a$ are different because the potentials we added are different.

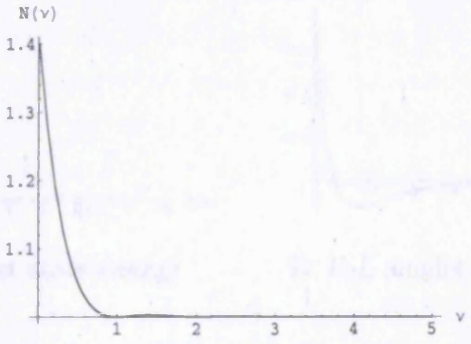

Fig. 2.5: $N(\nu)$ the normalization factors of $1s$ states of the Whittaker functions are plotted. Notice that when $\nu \geq 1$ the normalization factor is nearly equal to 1.

A.Heitler-London approximation

The first quantum-mechanical explanation of the chemical bond is usually attributed to Heitler and London [35]. Their discussion of the hydrogen molecule was not based on IPM(Independent Particle Model) concepts, each electron being instead assigned to atomic orbitals.

Heitler and London proposed their famous method for treating the hydrogen molecule in 1927. They started with atomic orbitals in setting up an approximate solution. They argued as follows: Let A represent a hydrogen $1s$ wave function centered at atom A, and B a hydrogen $1s$ wave function centered at atom B. Let us denote the coordinates of the two electrons by 1 and 2. At least when the atoms are widely separated, the ground state will be the situation where there is one electron on each atom. Thus, it could be represented by the wave function $A(1)B(2)$ or equally by the other function $A(2)B(1)$. These two products can not be the two-electron spatial wave function because it should be antisymmetric when you exchange the coordinates of these two electrons. Heitler and London found that suitable linear combinations are $A(1)B(2) \pm B(1)A(2)$, which are respectively, symmetric and antisymmetric in the coordinates of the electrons. In fact, the symmetric and anti-symmetric wave functions are respectively associated with singlet state and triplet state. They found that the symmetric function has an attractive potential energy curve, while the antisymmetric function indicates repulsion between the atoms, as in the repulsive curve (See Figure 2.6). They identified the symmetric function with a singlet state, the antisymmetric one with a triplet.

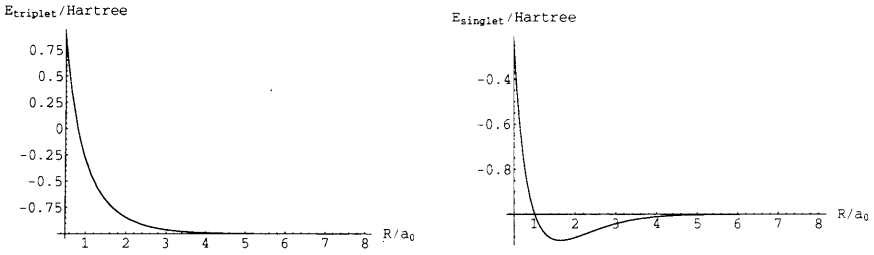

A: H-L triplet state energy B: H-L singlet state energy

Fig. 2.6: Heitler-London energy calculations of the triplet and singlet states in H_2 as functions of inter-nuclei distance R. Notice that curve A is like the repulsion curve and curve B is like the attractive potential energy curve.

We may then use these functions to find the expectation value of Hamiltonian for the singlet and triplet states. Since the Hamiltonian involves only the coordinates, and no spin operators, it is possible to compute its average value without consider-

ing the spins at all, using the properly normalized functions $A(1)B(2) \pm B(1)A(2)$ directly, as Heitler and London did. For convenience we shall assume that the atomic orbitals A and B are properly normalized, and that the overlap integral $\int A(1)B(1)dv_1 = S$. Then we find that the functions

$$\psi_\pm = \frac{1}{\sqrt{2(1 \pm S^2)}}[A(1)B(2) \pm B(1)A(2)] \tag{2.66}$$

are normalized.

The Hamiltonian operator is

$$-\frac{1}{2}\nabla_1^2 - \frac{1}{2}\nabla_2^2 - \frac{1}{r_{1A}} - \frac{1}{r_{2A}} - \frac{1}{r_{1B}} - \frac{1}{r_{2B}} + \frac{1}{r_{12}} + \frac{1}{R} \tag{2.67}$$

where r_{1A} is the distance from the first electron to the nucleus A, etc. r_{12} is the distance between the electrons, and R is the distance between the nuclei. Here we use Hartree as energy unit and Bohr radius as length unit. This leads to

$$E_\pm = -1 + \frac{H_0 \pm H_1}{1 \pm S^2} \tag{2.68}$$

where

$$H_0 = \int A^2(1)B^2(2)(-\frac{1}{r_{1B}} - \frac{1}{r_{2A}} + \frac{1}{r_{12}} + \frac{1}{R})dv_1 dv_2 \tag{2.69}$$

and

$$H_1 = \int A(1)B(1)A(2)B(2)(-\frac{1}{r_{1B}} - \frac{1}{r_{2A}} + \frac{1}{r_{12}} + \frac{1}{R})dv_1 dv_2. \tag{2.70}$$

The quantity called H_0 is ordinarily referred to as the Coulomb integral, and H_1 as the exchange integral. The quantities $E_\pm$ are respectively the average energies of symmetric and antisymmetric functions. These calculations are used to work out the exchange couplings between two electrons. The key simplification at this point is that A and B are eigenfunctions of the one-electron one-center Hamiltonian. The exchange coupling between two electrons in this two-centre case defines an effective Hamiltonian operator only on the spin degrees of freedom:

$$H_{EFF} = J\vec{S}_1 \cdot \vec{S}_2, \tag{2.71}$$

$$J = E_- - E_+ \tag{2.72}$$

and $\vec{S}_{1,2}$ are spin operators of these two electrons. So our sign convention is that the couplings between electrons are ferromagnetic if $J < 0$, and anti-ferromagnetic if $J > 0$. The leading term of Heitler-London exchange at large R is [36]

$$J_{H-L} = (56/45 - 4/15\gamma - 4/15 \ln R)R^3 e^{-2R} + O(R^2 e^{-2R}), \tag{2.73}$$

where γ is Euler's constant equal to 0.5772.

For the two electrons in H_2, the ground state should be nodeless [25], so the ground state is always the symmetric wave function which is associated with the singlet state. That means the singlet state is always lower than the triplet state and the exchange interaction should be be anti-ferromagnetic. But from expression (2.73) we can see that the Heitler-London method gives an unphysical negative exchange interaction when the distance between two atoms is very large (about $49.5a_0$) because of the dominant logarithm term. This logarithm term comes from the matrix elements of the Coulomb interaction $\frac{1}{r_{12}}$. So the limitation of Heitler-London approximation is that it takes inadequate account of mutual avoidance of exchanging electrons [36].

B.Herring-Flicker asymptotic form of exchange coupling

In 1964 Herring and Flicker [36] used a surface integral to calculate the exchange splitting between singlet and triplet states. They argued that the exchange splitting can be expressed as an integral involving the two-electron wave function over the hyperplane Σ where $z_1 = z_2, r_{1A}^2 + r_{2B}^2 = r_{2A}^2 + r_{1B}^2$.

$$\Phi_1 = \frac{1}{\sqrt{2}}(\phi_g + \phi_u) \tag{2.74}$$

$$J = \int_\Sigma \mathbf{dS}[(P\Phi_1)\nabla\Phi_1 - \Phi_1\nabla(P\Phi_1)] + O(e^{-4R}), \tag{2.75}$$

where ϕ_g and ϕ_u are the exact solutions of two-electron wave functions which are symmetric and anti-symmetric in the coordinates of two electrons. P is the operator permutating the electrons' coordinates. ∇ is the six-dimensional gradient.

By means of a perturbative procedure, which was first applied in H_2^+, they got an expression for the two-electron wave function and worked out the integral. The Herring-Flick asymptotic form for large R (in true atomic units as before) is

$$\begin{aligned} J_{H-F} &= E_{triplet} - E_{singlet} \\ &= 1.642R^{5/2}e^{-2R} + O(R^2e^{-2R}), \end{aligned} \tag{2.76}$$

where R is the distance between two hydrogen atoms. From expression (2.76) we can see that the exchange splitting is positive for all real R.

C. Kolos's calculation

In 1933, James *et al.* [37] improved the Heitler-London model by changing the trial wave functions. They argued that the wave function should be approximately the product of H-like function for distant electrons and H_2^+-like function for the close electrons. The above two conditions suggest the use of elliptic coordinates and the

insertion of an exponential factor which reduces to e^{-r} for either electron at large distances. The coordinates are

$$\lambda_1 = (r_{1A} + r_{1B})/R; \lambda_2 = (r_{2A} + r_{2B})/R \tag{2.77}$$

$$\mu_1 = (r_{1A} - r_{1B})/R; \mu_2 = (r_{2A} - r_{2B})/R \tag{2.78}$$

$$\rho = 2r_{12}/R, \tag{2.79}$$

where r_{1A}, r_{1B}, r_{12} and R are defined as before. The trial wave function takes the form:

$$\psi = \sum_{mnjkp} C_{mnjkp}\phi_{mnjkp} \tag{2.80}$$

$$\phi_{mnjkp} = (1/2\pi)e^{-\delta(\lambda_1+\lambda_2)}(\lambda_1^m\lambda_2^n\mu_1^j\mu_2^k\rho^p + \lambda_1^n\lambda_2^m\mu_1^k\mu_2^j\rho^p), \tag{2.81}$$

where C_{mnjkp} and δ are variational parameters. They calculated the binding energy of the hydrogen molecule by expanding the wave function in elliptic coordinates. This was believed to be the most accurate when the nuclear distance is smaller than 2 Bohr radius.

In 1965, Kolos *et al.* [38] generalized the expansion of the wave function in elliptic coordinates in order to extend the calculation of the ground state energy to large separations of the nuclei based on James's work. In order that the asymptotic form of the wave function at large distance reduces to Heitler-London wave functions, their trial wave function takes the form of:

$$\Psi = \sum_i c_i\Phi_i(1,2)x_1^l \pm c_i\Phi_i(2,1)x_2^l \tag{2.82}$$

$$\Phi_i = e^{(-\alpha\lambda_1-\overline{\alpha}\lambda_2)}\cosh(\beta\mu_1 + \overline{\beta}\mu_2)(\lambda_1^{m_i}\lambda_2^{n_i}\mu_1^{j_i}\mu_2^{k_i}\rho^{p_i}), \tag{2.83}$$

where $\alpha, \overline{\alpha}$, $\beta, \overline{\beta}$, and c_i are variational parameters. x_i is the Cartesian coordinate of the ith electron perpendicular to the molecular axis. $l = 0$ and $l = 1$ represent the wave functions for Σ and Π states, respectively. The $+$ or $-$ sign results in singlet state or triplet state. They got the numerical results for the exchange in the range of $0 \leq R \leq 7a_0$; these are plotted in Figure (2.7).

We have reviewed several exchange calculations of H_2 molecule including Heitler-London approximation, Herring-Flicker's asymptotic form of exchange splitting, and Kolos's calculation. We can compare them for values of R up to $7a_0$ in Figure 2.7 and for even larger values of R in Figure 2.8. Note that from $4a_0$ to $7a_0$ the Heitler-London is a good approximation to the exchange interaction if the other two calculations are more accurate. In Figure 2.8 we see that the intermediate-range behaviour of the two exchange calculations: J_{H-L} and J_{H-F} are very close.

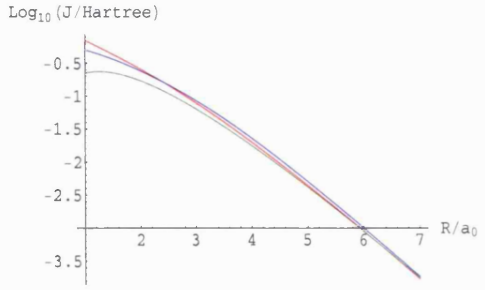

Fig. 2.7: The exchange splitting J calculated by three different methods as a function of inter-nuclei distance R. Red line: Heitler-London approximation, green line: Herring-Flicker asymptotic form, and blue line: Kolos's calculation. Notice that these three calculations are roughly consistent where R is from $4a_0$ to $7a_0$. From this point of view Heitler-London is a good approximation in that region.

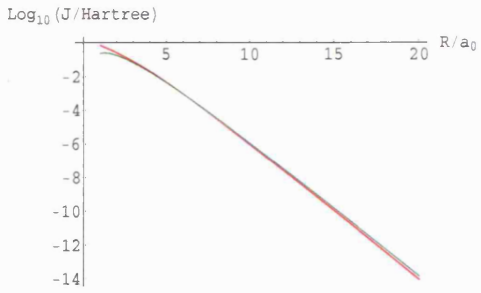

Fig. 2.8: The exchange splitting J as a function of inter-nuclei distance R. Red line: Heitler-London approximation; green line: Herring-Flicker asymptotic form. Notice that these two calculations are roughly consistent where R is from $4a_0$ to $20a_0$. But these two are quite far away from each other at small inter-nuclei distance. At very large inter-nuclei distance the Heitler-London approximation becomes negative, but Herring-Flicker calculation does not.

2.5.2 Review of the previous work on two-donor exchange calculations based on effective mass theory

A. Andres' calculation of exchange interaction

In 1981, Andres *et al.* [39] calculated the exchange interaction between two phosphorus donor electrons in silicon based on effective mass theory and Luttinger-Kohn variational form of the impurity states. After the spherical approximation of the envelope functions, the exchange interactions are the products of a rapidly varying interference factor and an isotropic factor which can be calculated from the hydrogen molecule.

$$J_A(R) = (\sum_{\nu=1}^{6}[\frac{1}{6}\cos(\vec{k}_\nu \cdot \vec{R})])^2 j_s(R), \tag{2.84}$$

where $j_s(R)$ is the hydrogenic exchange expression, and R is the inter-donor distance. $\vec{k}_\nu$ is the position of the νth conduction band minimum.

B. Koiller's calculation of two-donor exchange

In 2002, Koiller *et al.* [40] combined the effective mass theory and Heitler-London approximation to calculate the exchange interaction between donor electrons. They found that the exchange interaction between two donor electrons in silicon oscillates as the distance between donors changes.

The Heitler-London expression of the exchange splitting in Si was [40]

$$\begin{aligned} J(\vec{R}) &= \sum_{\nu,\mu}[\sum_{\vec{K},\vec{K}'}|c^\nu_{\vec{K}}|^2|c^\mu_{\vec{K}'}|^2 e^{i(\vec{K}-\vec{K}')\cdot\vec{R}}] \\ &\quad \times|\alpha_\nu|^2|\alpha_\mu|^2 J_{\nu\mu}(\vec{R})\cos(\vec{k}_\nu - \vec{k}_\mu)\cdot\vec{R}, \end{aligned} \tag{2.85}$$

where a pair of donors are at $\vec{R}_A = 0, \vec{R}_B = \vec{R}$ and $R >> a, b$(effective Bohr radii). The explicit expression of $J_{\nu\mu}$ is also given in the appendix of Koiller' paper [40]. The second sum (in the square bracket) in equation (2.85) refers to the reciprocal-lattice expansion of Bloch functions, $u_\nu(\vec{r}) = \sum_{\vec{K}} c^\nu_{\vec{K}} e^{i\vec{K}\cdot\vec{r}}$, and $\vec{k}_\nu, \vec{k}_\mu$ are band minima points. α_ν and α_μ are the components of the vectors shown in section 2.2.1.

We can see that both (2.84) and (2.85) took into account the rapid oscillating terms $e^{i\vec{k_\nu}\cdot\vec{R}}$. But the formula (2.85) is calculated by means of the Kohn-Luttinger variational form and the Heitler-London approximation.

The Heitler-London approximation used by Koiller *et al.* to calculate the exchange coupling between two electrons is analogous to that in the H_2 molecule. They changed the hydrogenic ground state energy to the single-donor ground state energy and the corresponding wave functions to the Luttinger-Kohn variational form. In

their Heitler-London formula the wave functions are assumed to be eigenfunctions of the single-donor Hamiltonian. Therefore the problem in their calculation is that the variational form of the Luttinger-Kohn wave function is not appropriate for the Heitler-London approximation given in their paper. However we can calculate two-center exchange coupling without assuming the electron wave function to be an eigenfunction of the single-donor Hamiltonian.

Both Andres and Koiller used the Luttinger-Kohn variational form, and included the oscillating factors in the calculation. The difference is that Andres changed the hydrogenic exchange expression $j_s(R)$ which is isotropic in his calculation, but Koiller calculated the anisotropic $J_{\nu\mu}$ approximately.

So now we have two ways to calculate exchange coupling:

1. To calculate the singlet-triplet splitting directly, without worrying about whether the wave functions are the eigenfunctions of one-electron single-atom Hamiltonian using Heitler-London approximation. Let's assume A and B are the same donor electron states in the different centres A and B. Then the calculation method here is

$$\langle\psi_\mp|\hat{H}|\psi_\mp\rangle = \frac{1}{1\mp S^2}[2\langle A(1)|(-\frac{1}{2}\nabla^2)|A(1)\rangle + 2\langle A(1)|(-\frac{1}{r_{1A}})|A(1)\rangle$$
$$+2\langle A(1)|(-\frac{1}{r_{1B}})|A(1)\rangle \mp 2S(\langle A(1)|(-\frac{1}{2}\nabla^2)|B(1)\rangle + 2\langle A(1)|(-\frac{1}{r_{1A}})|B(1)\rangle)$$
$$+\int d[1]d[2]\frac{A^2(1)B^2(2)}{r_{12}} \mp \int d[1]d[2]\frac{A(1)B(1)A(2)B(2)}{r_{12}}] + \frac{1}{R} \tag{2.86}$$
$$J = \langle\psi_-|\hat{H}|\psi_-\rangle - \langle\psi_+|H|\psi_+\rangle, \tag{2.87}$$

and the definition of $\hat{H}$, $\psi_\pm$ are in the section (2.5.1).

If we assume

$$(-\frac{1}{2}\nabla_1^2 - \frac{1}{r_{1A}})|A(1)\rangle = E_0|A(1)\rangle, \tag{2.88}$$

we will get the expression 2.89 below.

2. The route taken by Koiller *et al.* is based on a combination of the effective mass theory and Heitler-London approximation, but assuming that the individual donor states are eigenstates of single-donor Hamiltonian.

The basic formulae are

$$E_t^s = 2E_0 + \frac{H_0 \pm H_1}{1 \pm S^2} \tag{2.89}$$
$$H_0 = \int d[1]d[2]|A(1)|^2\hat{O}|B(2)|^2 \tag{2.90}$$
$$H_1 = \int d[1]d[2]A(1)^*B(2)^*\hat{O}B(1)A(2) \tag{2.91}$$

$$\hat{O} = -\frac{1}{r_{1B}} - \frac{1}{r_{2A}} + \frac{1}{r_{12}} + \frac{1}{R}. \tag{2.92}$$

Now we have improved wave functions, in the form of Whittaker functions with central cell correction, so in the next section we can use these wave functions to calculate the exchange splitting between two donor electrons and compare those two routes. We expect the calculation results from these two routes should be similar except for some numerical error.

2.5.3 Fitting Whittaker function with a 1s-type Guaussian

Whittaker functions with the model central cell correction are valid over all the range of r which can describe the donor wave functions. Based on these functions we can calculate the Heitler-London exchange coupling of two donor electrons (we take the case $Z = 1$).

First of all, in order to calculate the integral between different centres, we expand $P_{\nu,0}(r)/r$ using $1s$ Gaussian-type orbitals because the form of Whittaker function is quite complicated and it is quite difficult to calculate the exchange couplings directly:

$$\frac{P_{\nu,0}(r)}{r} \simeq R_\nu^G(r) = \sum_n A_n G_n(r, B_n) \tag{2.93}$$
$$G_n(r, B_n) = e^{-B_n r^2}.$$

In Figure (2.9) and Figure (2.10) we respectively fit $P_{1.0,0}(\vec{r})/r$ and $P_{1.1,0}(\vec{r})/r$ and compare them with the original wave functions. Here we use ten $1s$ Gaussian-type orbitals to fit Whittaker function.

2.5.4 Exchange calculation using Whittaker function

The following formulae were derived by Boys [42] for the integrals between $1s$ Gaussian-type orbitals associated with different centres. These formulae can be used to calculate the exchange between two Whittaker functions centered at different positions after the Whittaker-type orbital is expanded to the sum of $1s$ Gaussian-type orbitals. If we assume that

$$|aA\rangle = \exp(-ar_{1A}^2), \tag{2.94}$$

where A refers to centres, etc, then we have the following formulae:

- **Overlap matrix elements**

$$\mathrm{Ovlp}(A, B, a, b) = \langle aA|bB\rangle$$

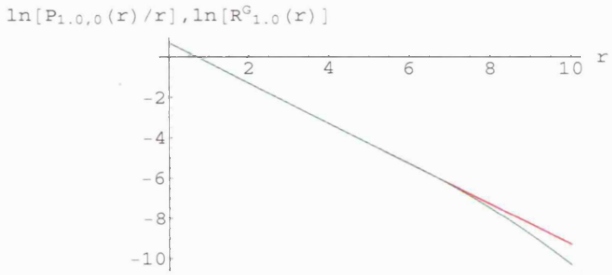

Fig. 2.9: Gaussian fitting of Whittaker function $P_{1.0,0}/r$. Here we used ten Gaussians to fit the Whittaker function. The Whittaker function $P_{1.0,0}/r$ is also plotted for comparison. Red line: $\ln P_{1.0,0}(r)/r$; Green line: $\ln R^G_{1.0}(r)$. We can see that there is splitting between the tails of two curves. There are two reasons for this. One is that Gaussian fitting is not good enough, while another is the long-range behaviors of Gaussians and Whittaker functions are different in principle.

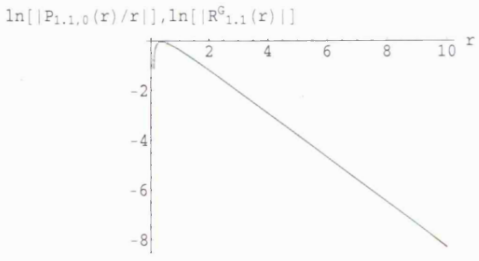

Fig. 2.10: Gaussian fitting of Whittaker function $P_{1.1,0,r}/r$. Red line: $\ln|P_{1.1,0}(r)/r|$; green line:$\ln|R^G_{1.1}(r)|$.

$$= \int \exp(-ar_{1A}^2 - br_{1B}^2)d\vec{r_1}$$
$$= (\frac{\pi}{a+b})^{3/2}\exp(-\frac{ab}{a+b}\overline{AB}^2); \quad (2.95)$$

- **Kinetic energy matrix elements**

$$K = -\frac{1}{2}\nabla^2 \quad (2.96)$$
$$KE(A,B,a,b) = \langle aA|K|bB\rangle$$
$$= \int \exp(-ar_{1A}^2)(-\frac{1}{2}\nabla_1^2)\exp(-br_{1B}^2)d\vec{r_1}$$
$$= \frac{ab}{a+b}(3 - \frac{2ab}{a+b}\overline{AB}^2)(\frac{\pi}{a+b})^{3/2}$$
$$\times \exp(-\frac{ab}{a+b}\overline{AB}^2); \quad (2.97)$$

- **Potential energy matrix elements**

$$V_C = -1/r_C \quad (2.98)$$
$$VE(A,B,C,a,b) = \langle aA|V_C|bB\rangle$$
$$= \int (-1/r_{1C})\exp(-ar_{1A}^2 - br_{1B}^2)d\vec{r_1}$$
$$= \frac{2\pi}{a+b}F_0[(a+b)\overline{CP}^2]\exp(-\frac{ab}{a+b}\overline{AB}^2); \quad (2.99)$$

- **Two-particle integrals**

$$XG(A,B,C,D,a,b,c,d) = [aAbB;cCdD]$$
$$= \int\int (1/r_{12})\exp(-ar_{1A}^2 - br_{1B}^2 - cr_{2C}^2 - dr_{2D}^2)d\vec{r_1}d\vec{r_2}$$
$$= \frac{2\pi^{5/2}}{(a+b)(c+d)\sqrt{a+b+c+d}}F_0[\frac{(a+b)(c+d)}{a+b+c+d}\overline{PQ}^2] \times$$
$$\exp(-\frac{ab}{a+b}\overline{AB}^2 - \frac{cd}{c+d}\overline{CD}^2). \quad (2.100)$$

The points P and Q lie on $\overline{AB}$ and $\overline{CD}$, respectively, and are given by, $P_x = \frac{aA_x+bB_x}{a+b}$, $Q_x = \frac{cC_x+dD_x}{c+d}$, etc.

$$F_m(t) = \int_0^1 u^{2m}\exp(-tu^2)du, \quad (2.101)$$
$$(t > 0; m = 0, 1, 2...),$$
$$= \frac{1}{2t^{m+1/2}}\gamma(m+1/2, t).$$
$$F_0(t) = \frac{1}{2}\sqrt{\pi/t} \times \mathrm{erf}(\sqrt{t}) \quad (2.102)$$
$$\mathrm{erf}(x) = \frac{2}{\sqrt{\pi}}\int_0^x e^{-t^2}dt. \quad (2.103)$$

Here $\mathrm{erf}(x)$ is the error function.

We can use these formulae to calculate the exchange interaction between two donor electrons whose wave functions are Whittaker functions. For example, the potential matrix elements:

$$\langle\psi_A|(-\frac{1}{|\vec{r}-\vec{R_C}|})|\psi_B\rangle = \sum_{m,n=1}^{g} A_m A_n VE(A,B,C,B_m,B_n). \tag{2.104}$$

So we can use the Gaussian fitting to calculate all the matrix elements in the Heitler-London approximation.

We then calculate the exchange numerically, in the following stages:

1. First we calculate exchange coupling with hydrogenic ($n = 1$)basis function $P_{1.0,0}(r)$ in two different ways: using the standard Heitler-London approach with Coulomb wave functions, and using our Gaussian fit to the Whittaker function. By this means we can check that the Mathematica code is correct for this case.

2. Change the basis function to $P_{1.1,0}(r)$ to calculate exchange coupling in the two ways: equation 2.86 and equation 2.89–2.92. Then we compare these two calculating procedures. One is to calculate the exchange interaction directly, and the other is Koiller's route.

3. Change the basis function to $P_{1.1,0}(r)$ (relatively shallow donors) and $P_{0.7,0}(r)$ (deep donors) with central cell corrections, and include a δ potential or square well potential with radius $a = 0.01$.

A. Exchange coupling with basis function $P_{1.0,0}(r)$

Supposing two electrons stay in the following two basic wave functions ψ_A, ψ_B with different centers:

$$\begin{aligned}\psi_A &= \frac{1}{\sqrt{4\pi}} P_{1.0,0}(|\vec{r}-\vec{R_A}|)/|\vec{r}-\vec{R_A}|;\\ \psi_B &= \frac{1}{\sqrt{4\pi}} P_{1.0,0}(|\vec{r}-\vec{R_B}|)/|\vec{r}-\vec{R_B}|;\\ &|\vec{R_A}-\vec{R_B}| = R.\end{aligned} \tag{2.105}$$

B. Exchange coupling with basic function $P_{1.1,0}(r)$

In this step we change the basic functions to $P_{1.1,0}(r)$.

$$\begin{aligned}\psi_A &= \frac{1}{\sqrt{4\pi}} P_{1.1,0}(|\vec{r}-\vec{R_A}|)/|\vec{r}-\vec{R_A}|;\\ \psi_B &= \frac{1}{\sqrt{4\pi}} P_{1.1,0}(|\vec{r}-\vec{R_B}|)/|\vec{r}-\vec{R_B}|;\\ &|\vec{R_A}-\vec{R_B}| = R.\end{aligned} \tag{2.106}$$

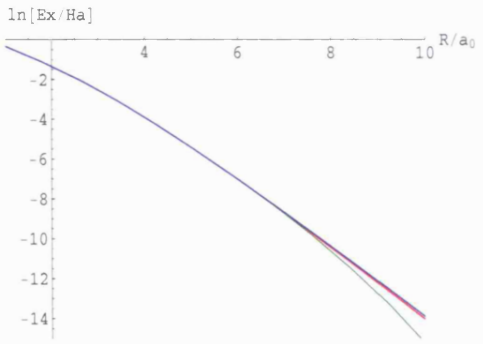

Fig. 2.11: The exchange coupling between two electrons whose wave functions are $1s$ states as a function of inter-nuclei distance R. Red line: directly calculated singlet-triplet splitting based on $R^G_{1.0}$; green line:Koiller's route to calculate exchange coupling based on $R^G_{1.0}$; blue line: based on Hydrogenic $1s$ state.

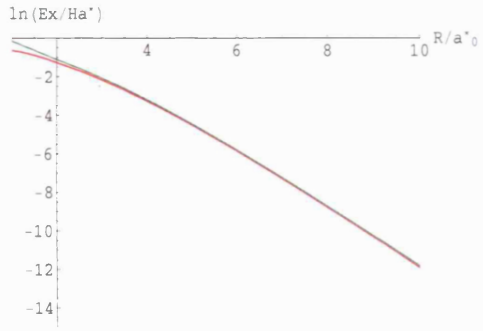

Fig. 2.12: The exchange coupling between two shallow donor electrons as a function of inter-donor distance R. Red line:Koiller's route to calculate exchange coupling based on $R^G_{1.1}$; green line: directly calculated singlet-triplet splitting based on $R^G_{1.1}$. Notice that these two calculations are roughly consistent with each other from 5 to 10 a^*_0.

Eventually, In Figure (2.12) we can see these two results of exchange coupling from different calculation methods are very close to each other in the region we are interested in although we have not considered the central cell correction. When $5 < R < 20$, the results from different ways to calculate exchange is roughly the same. We can see our improvement matches two Heitler-London approximations associated with equation 2.86 and equation 2.89 in this region.

C. Exchange coupling with basic function $P_{1.1.0}(r)$ with central cell correction

In this step we add the central cell correction. We only need to add some very small modification relative to the whole exchange coupling. We can see that the exchange calculation results are very close to each other.

- δ potential

  The small modification is from the matrix elements between wavefunctions associated with different centres. The one-center one-electron energy is unchanged because of the cancelation of kinetic energy and potential energy. The radial function satisfies

  $$-\frac{1}{2}\frac{\partial}{\partial r}(r^2\frac{\partial R}{\partial r}) + V(r)R = ER. \tag{2.107}$$

  If V includes a δ function of strength λ at $r = a$, then multiplying by r^2 and integrating from $a - \epsilon$ to $a + \epsilon$ gives (ignoring terms of order ϵ and higher)

  $$-\frac{1}{2}[r^2\frac{\partial R}{\partial r}]_{a-\epsilon}^{a+\epsilon} + a^2\lambda R(a) = 0. \tag{2.108}$$

  Hence, the derivative obeys

  $$\frac{\partial R}{\partial r}(a+\epsilon) - \frac{\partial R}{\partial r}(a-\epsilon) = 2\lambda R(a) \tag{2.109}$$

  But this means that the kinetic energy operator acting on R looks like

  $$\begin{aligned} -\frac{1}{2}\frac{1}{r^2}\frac{\partial}{\partial r}r^2\frac{\partial R}{\partial r} &= -\frac{1}{2}\times 2\lambda R(a)\delta(r-a) + \textbf{smooth terms} \\ &= -\lambda R(a)\delta(r-a) + \textbf{smooth terms}. \end{aligned} \tag{2.110}$$

  The δ function singularity exactly cancels the singularity in the potential energy. So this means that we don't have to include the terms ΔV whenever they occur along with a kinetic energy operator to 'compensate' them. So we are only concerned with different-centre potential energy integrals including $\langle A(1)|(\frac{1}{r_{1A}} + \delta V_A)|B(1)\rangle$ and $\langle A(1)|(\frac{1}{r_{1B}} + \delta V_B)|A(1)\rangle$.

  In Figure (2.17) we can see that the two methods of calculating exchange couplings are consistent in the range of $1 \leq R \leq 10a_0^*$.

- Square well potential

  In figure 2.14 we can see that the two results of calculating exchange couplings are consistent in the range of $1 \leq R \leq 10a_0^*$.

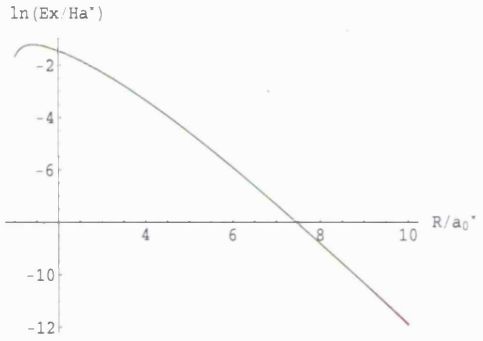

Fig. 2.13: The exchange coupling of two shallow donors with δ-potential central cell correction as a function of inter-donor distance R. Green line: directly calculated singlet-triplet splitting based on $R^G_{1.1}$ with δ potential central cell correction; Red line:Koiller's method to calculate exchange coupling based on $R^G_{1.1}$ with δ potential central cell correction. The red curve is indistinguishable.

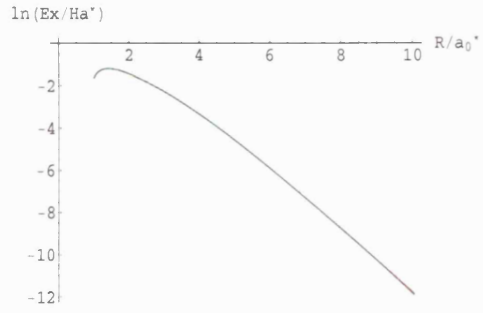

Fig. 2.14: The exchange coupling of two shallow donors with square well potential central cell correction as a function of inter-donor distance R. Red line: directly calculated singlet-triplet splitting based on $R^G_{1.1}$ with square well potential central cell correction; Green line: Koiller's method to calculate exchange coupling based on $R^G_{1.1}$ with square well potential central cell correction. The red curve is indistinguishable.

D.Exchange coupling for two deep donor electrons

Similarly, we can calculate the exchange coupling between two deep donors. According to the binding energy of Bi impurity in silicon, which is approximately -1.0 Hartree*, correspondingly we can calculate ν which is approximately 0.7.

Note that these two curves in Figure (2.15) are basically consistent in the range of $1 \leq R \leq 5a_0^*$, except for in some place the green curve changes sign. This is because $|S^2 E_0|$ is not exactly equal to, but slightly smaller than $|S\langle A(1)|(-\frac{1}{2}\nabla^2 - \frac{1}{r_{1A}})|B(1)\rangle|$ based on our Gaussian expansion. We should say that the Gaussian expansion is not good enough. There is the same problem in the figures we will show in the following.

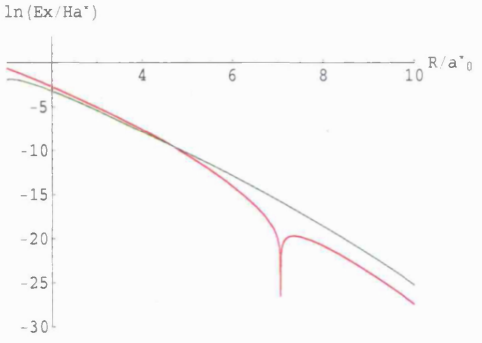

Fig. 2.15: The exchange coupling between two deep donor electrons as a function of inter-donor distance R. Green line: directly calculated singlet-triplet splitting based on $R_{0.7}^G$ without central cell correction; red line: Koiller's route to calculate exchange coupling based on $R_{0.7}^G$ without central cell correction.

2.6 Comparison with the scaled Hydrogenic exchange interaction

We can also compare the scaled exchange interaction from Heitler-London formula and Herring-Flicker asymptotic form with our calculations. Putting this another way, we just change the inter-atom distance R to R/ν. See Figures 2.18-2.21.

We can also calculate the ratio of $\frac{|J_{calculated} - J_{H-L}^{scaled}|}{|J_{calculated}|}$ (See Figure 2.22)and $\frac{|J_{calculated} - J_{H-F}^{scaled}|}{|J_{calculated}|}$ (See Figure 2.23). We can see that the scaled hydrogenic exchange does not agree with the calculated ones. Therefore, we can not use the scaled hydrogenic exchange to approximate donor exchange.

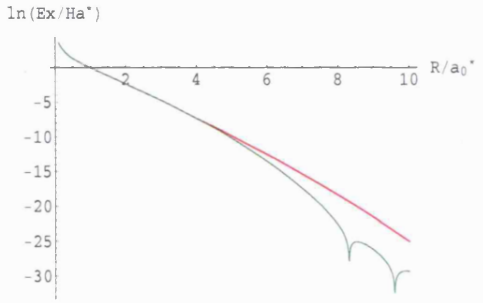

Fig. 2.16: The exchange coupling between two deep donor electrons with δ-potential central cell correction as a function of inter-donor distance R. Red line: directly calculated singlet-triplet splitting based on $R^G_{0.7}$ with δ potential central cell correction; Green line:Koiller's route to calculate exchange coupling based on $R^G_{0.7}$ with δ potential central cell correction.

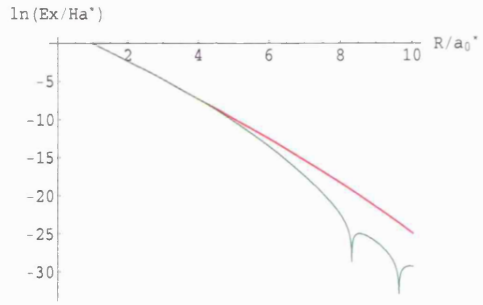

Fig. 2.17: The exchange coupling between two deep donor electrons with square-well potential central cell correction as a function of inter-donor distance R. Red line: directly calculated singlet-triplet splitting based on $R^G_{0.7}$ with square well potential central cell correction; Green line:Koiller's route to calculate exchange coupling based on $R^G_{0.7}$ with square well potential central cell correction.

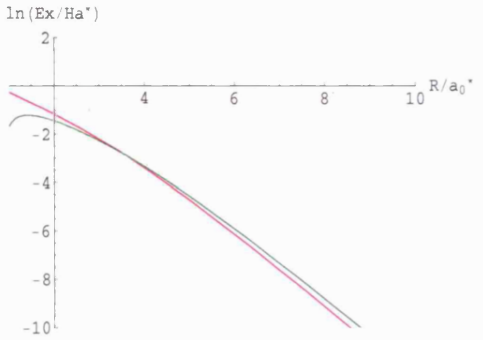

Fig. 2.18: The scaled exchange coupling between two shallow donor electrons as a function of inter-donor distance R. Green line: Heitler-London directly calculated singlet-triplet splitting based on $R^G_{1.1}$ with δ potential central cell correction; pink line: Scaled exchange splitting using Heitler-London formula $J_{H-L}(R/1.1)$.

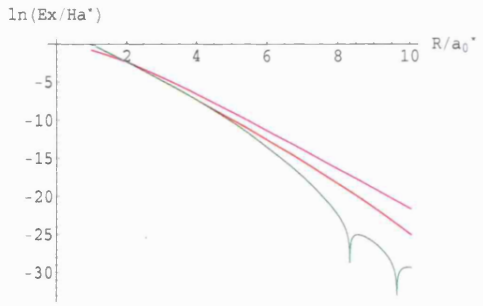

Fig. 2.19: The scaled exchange coupling between two deep donor electrons as a function of inter-donor distance R. Red line: Heitler-London directly calculated singlet-triplet splitting based on $R^G_{0.7}$ with square-well potential central cell correction; green line: Heitler-London singlet-triplet splitting based on Koiller's route; pink line: Scaled exchange splitting using Heitler-London formula $J_{H-L}(R/0.7)$.

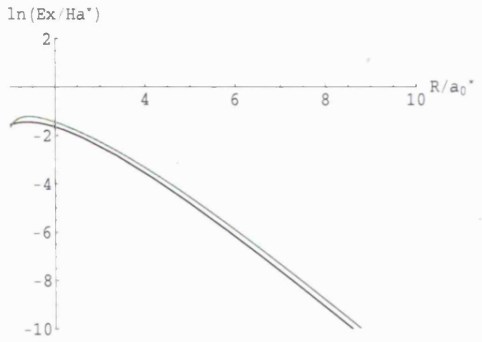

Fig. 2.20: The scaled exchange coupling between two shallow donor electrons as a function of inter-donor distance R. Green line: Heitler-London directly calculated singlet-triplet splitting based on $R^G_{1.1}$ with δ potential central cell correction; black line: Scaled exchange splitting using Herring-Flicker formula $J_{H-F}(R/1.1)$.

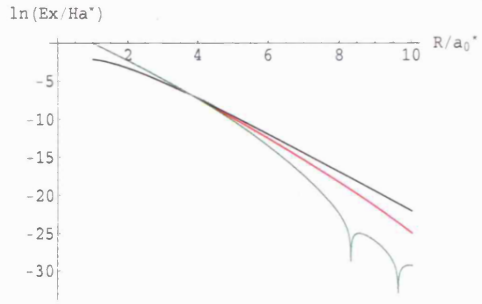

Fig. 2.21: The scaled exchange coupling between two deep donor electrons as a function of inter-donor distance R. Red line: Heitler-London directly calculated singlet-triplet splitting based on $R^G_{0.7}$ with square-well potential central cell correction; green line: Heitler-London singlet-triplet splitting based on Koiller's route; black line: Scaled exchange splitting using Herring-Flicker formula $J_{H-L}(R/0.7)$.

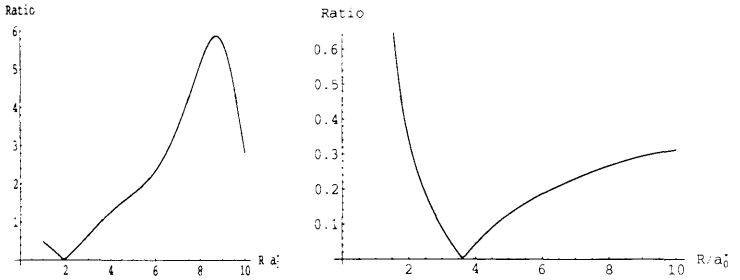

(a) (b)

Fig. 2.22: The ratio $\frac{|J_{calculated} - J_{H-L}^{scaled}|}{|J_{calculated}|}$ as a function of inter-donor distance is plotted for a deep donor: (a) $\nu = 0.7$, and a shallow donor (b) $\nu = 1.1$. Notice that the calculation of shallow donors is better than the deep one. Because the deep donor electron spends much time near the donor center, the scaling which represents the decay of the wave functions may not be appropriate for it.

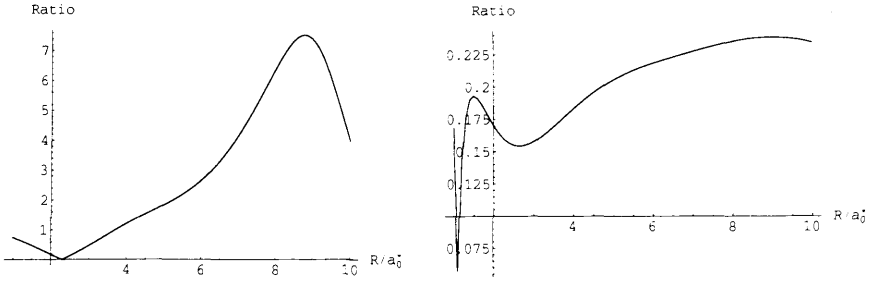

(a) (b)

Fig. 2.23: The ratio $\frac{|J_{calculated} - J_{H-F}^{scaled}|}{|J_{calculated}|}$ as a function of inter-donor distance is plotted for a deep donor: (a) $\nu = 0.7$, and a shallow donor (b) $\nu = 1.1$.

2.7 Multi-valley effect

The above two-donor exchange calculation can provide the integrals associated with envelope functions as included in $J(R)$ of equation 2.85 which is calculated using Heitler-London model for the exchange interaction for donors in silicon. After we ignore the rapid oscillating terms in the calculations of integrals involving Bloch functions we can find the other part is the multi-valley terms $e^{i(\vec{k}^{(i)}-\vec{k}^{(j)})\cdot\vec{R}}$, where $\vec{k}^{(i)}, \vec{k}^{(j)}$ and $\vec{R}$ are given in equation (2.85) if $\vec{R}$ is a fcc lattice vector. These terms can bring to the exchange interaction an additional periodic effect because they are periodical functions [40]. These terms also depend on the orientation of $\vec{R}$, i.e., the positions of two donors. So our expression for two-donor exchange interaction considering the multi-valley effect is:

$$\begin{aligned} J(R) &= \sum_{\nu,\mu}[\sum_{\vec{K},\vec{K}'} |c^{\nu}_{\vec{K}}|^2 |c^{\mu}_{\vec{K}'}|^2 e^{i(\vec{K}-\vec{K}')\cdot\vec{R}}] \\ &\quad \times |\alpha_\nu|^2 |\alpha_\mu|^2 J_w(R)\cos(\vec{k}_\nu - \vec{k}_\mu)\cdot\vec{R}, \end{aligned} \tag{2.111}$$

where $J_w(R)$ is our exchange interaction calculated by using Whittaker functions.

2.8 Conclusion

From the above exchange calculations we can summarize:

1. We have introduced a δ-potential and a square-well potential as model central cell corrections which can be coupled to the Whittaker-function solution in the far region to find the full one-electron eigenfunctions of an isotropic Hamiltonian for a single deep donor.

2. These central cell corrections resolve a discrepancy between two formulae for the exchange splitting, one used by Koiller *et al.* and another route based on the original Heitler-London formula, because they ensure that the potential and wavefunctions used in the calculations are compatible with one another.

3. Comparing the exchange calculations with and without central cell corrections, we see that the form of the Whittaker function is much more important than the presence of the central-cell correction.

4. Exchange couplings between typical shallow donors and deep donors are calculated. For a given distance, we find, as expected, that the exchange coupling between shallow donors is larger than between deep donors, at least in our calculation range.

5. We have compared the scaled hydrogenic exchange interaction from the Heitler-London formula and Herring-Flicker asymptotic form with our calculations. The scaled hydrogenic exchange interaction is not a good approximation.

6. We can now calculate Heitler-London exchange interactions between two donors having arbitrary binding energies. If we are given the energy levels of the single defects, we can find the defect wave functions by using quantum defect methods, and then evaluate the Heitler-London exchange interaction between defects.

3. COUPLING OF DONOR AND CONTROL QUBITS: VARIATIONAL SOLUTION OF A SIMPLE MODEL

3.1 Introduction

As described in chapter 1, we will perform a variational calculation about the control-qubit system in this chapter. In the control-qubit system qubit carriers are localized, the 'control' electron can be delocalized, and the separation between donors is relatively large. We can readily recall and use the Heitler-London approach in molecular physics to construct the total wave function of these three electrons. In the following sections, we will discuss how to construct the wave functions of the control-qubit system using the Heitler-London model and donor wave functions. After that we can calculate the energy spectra variationally and extract the exchange couplings among these three electrons.

We wish to address the following questions:

- How large is the control-qubit interaction, as a function of the control-qubit separation and the electronic states of the control and qubit?
- What is the relative importance of the qubit-qubit interaction as compared to the control-qubit interaction?
- Is the qubit-qubit interaction altered from its value in an isolated donor pair by the presence of the control atom? If so, how is it altered?
- Does the control electron always reside on the control atom when it is excited?

3.2 Three-donor Heitler-London exchange calculation

3.2.1 Single-donor wave functions: Whittaker basis function

Before we use the Heitler-London model to construct the total wave function of three electrons, we have to know the single-electron wave function. As introduced in the second chapter, a Whittaker function given in the quantum defect method is the solution of the isotropic single-donor Schrödinger equation far away from the

donor centre. So we can use the Whittaker functions introduced in section 2.3 to describe the donor electron wave function in the control-qubit system. Here we ignore the central cell correction when we calculate the exchange coupling because the donors are far apart from each other, therefore the small modification in the central region of wave function can be neglected. We notice that as the absolute value of ν becomes larger, the Whittaker function becomes more diffuse, so we can select some Whittaker functions with larger ν as control electron states and qubit excited states, and other Whittaker functions associated with small ν as qubit ground states.

3.2.2 Identification of donor excited states

A. Identification of donor excited states with δ potential central cell correction

In the control-qubit system the control electron is excited, so we need to know the excited states corresponding to a deep donor. We have to choose the same model central cell correction for excited states as used to describe ground states. First, we use the δ potential central cell correction. Because the model central cell corrections need to be the same, we need to fix the strength of the δ-potential λ and the correction point a as defined in section 2.4. For example, we select $P_{\nu_0,0}(r)$ as donor ground state to do variational calculations, we have to find excited states which are orthogonal to $P_{\nu_0,0}(r)$. First, we can calculate λ using $P_{\nu_0,0}(r)$ and a as derived in section 2.4:

$$\lambda(\nu_0, a) = (\frac{\partial[\ln(P_{\nu_0,l=0}(r)/r)]}{\partial r}|_{r=a} + 1)/2, \tag{3.1}$$

and then other eigenfunctions have to satisfy

$$\frac{\partial \ln(P_{\nu,0}(r)/r)}{\partial r}|_{r=a} = 2\lambda(\nu_0, a) - 1. \tag{3.2}$$

By solving this equation we can find the values of ν corresponding to excited states. In Figure (3.1) the crossing points of the red and green lines show the ν values of eigenfunctions which are orthogonal to $P_{1.1,0}(r)$ with δ potential central cell correction.

B. Identification of donor excited states with square well potential central cell correction

Similarly, when we look for the excited states orthogonal to the ground states on which we do the square well potential central cell correction, we have to fix V_0 as

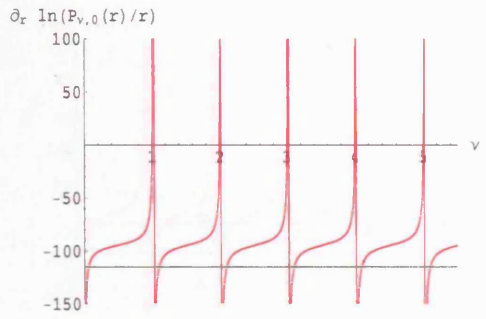

Fig. 3.1: Excited states orthogonal to $P_{1.1,0}(r)$ are found using δ-potential central cell correction. The logarithmic derivative of $P_{\nu,0}(r)/r$ as a function of ν is plotted, and $\lambda(\nu = 1.1, a = 0.01)$ is also plotted to find the excited states as we said in the above text. ν values associated with those crossing points of red and green curves correspond to the eigenfunctions including excited states. Red curve: The logarithmic derivative of $P_{\nu,0}(r)/r$; green straight line is $\lambda(\nu = 1.1, a = 0.01)$. Notice that the interval between ν values of adjacent eigenstates $\Delta\nu \simeq 1.0$.

defined in section 2.4. We have to solve this equation

$$k(\nu_0, a) = \sqrt{-\frac{1}{2\nu_0^2} - V_0(\nu_0, a)} \tag{3.3}$$

$$\frac{\partial \ln(P_{\nu,0}(r))}{\partial r}|_{r=a} = k(\nu_0, a)\cot[k(\nu_0, a)a] \tag{3.4}$$

In Figure (3.2) the crossing points correspond to different eigenvalues. By comparing Figure (3.1) and figure (3.2), we can see that the ν values of excited states found by these two methods are nearly the same.

3.2.3 System Hamiltonian

Before we set up the system Hamiltonian, we have to make some approximations. We only consider these three donors with no account of interactions with the external environment (except insofar as they are included in the effective mass Hamiltonian). In other words, we assume that the interactions between the control-qubit system and the environment are negligible compared with the interactions between donor electrons in the control-qubit system. Therefore, the Hamiltonian of this three-electron system is

$$\hat{H} = \sum_i \hat{h}_i + \frac{1}{2}\sum_{i\neq j}\frac{1}{|\vec{r}_i - \vec{r}_j|}, \tag{3.5}$$

where

$$\hat{h}_i = -\frac{{\nabla_i}^2}{2} - \frac{Z_C}{|\vec{r}_i - \vec{R}_C|} - \frac{Z_A}{|\vec{r}_i - \vec{R}_A|} - \frac{Z_B}{|\vec{r}_i - \vec{R}_B|}. \tag{3.6}$$

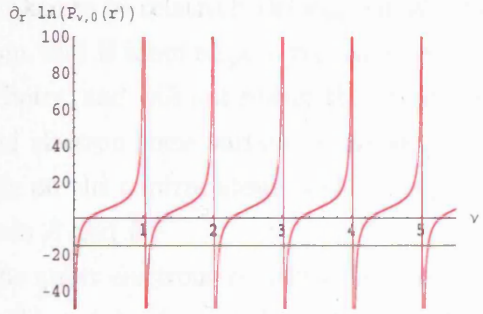

Fig. 3.2: Excited states orthogonal to $P_{1.1,0}(r)$ are found using square well potential central cell correction. The logarithmic derivative of $P_{\nu,0}(r)$ as a function of ν is plotted, and $(k(\nu_0, a)\cot[k(\nu_0, a)a])$ with $\nu_0 = 1.1, a = 0.01$ is also plotted to find the excited states as we said in the above text. The crossing points are associated with ν values of the eigenfunctions including excited states. Red curve: The logarithmic derivative of $P_{\nu,0}$; green straight line is $(k(\nu_0, a)\cot[k(\nu_0, a)a])$ with $\nu_0 = 1.1, a = 0.01$. Notice that the interval between ν values of adjacent eigenstates $\Delta\nu \simeq 1.0$.

Here $\vec{r}_i$ labels the coordinate of electron i, while $\vec{R}_C$, $\vec{R}_A$, and $\vec{R}_B$ respectively label the coordinates of control nucleus C, A nucleus, and B nucleus, with nuclear charges Z_C, Z_A, and Z_B. For now, we set $Z_C = Z_A = Z_B = 1$. We use scaled effective atomic units: effective Hartree for energy and effective Bohr radius a_0^* for length. Of course these should be scaled to the effective values for the host semiconductor in order to obtain real physical parameters. We assume that

- the effective mass of the donor electron is $0.33m_e$ (actually this is an average value $(m_1 m_2^2)^{1/3}$ of the anisotropic effective mass in Chapter 2), where m_e is free electron mass,
- the effective Bohr radius is about $1.7nm$,
- the effective Hartree is about 0.1 electron volt.

For the present we neglect valley degeneracy of donor states in Silicon and the conduction band anisotropy.

3.2.4 Construction of trial wave functions

We make a simple variational ansatz for the wave function of the control electron, writing the corresponding one-electron state as

$$\psi_C = \alpha\phi_C + \beta\phi_A + \gamma\phi_B, \tag{3.7}$$

where ϕ_C, ϕ_A, ϕ_B are taken to be relatively delocalized Whittaker functions centered at control atom, A atom, and B atom respectively as we say in section 1.3. Although this is a very simple choice, and will not reflect the full complexity of the problem, it does give the control electron some variational freedom between the extremes of being localized entirely on the control atom, and entirely on a 'molecular' excited state of the qubit atoms A and B.

We assume that the qubit electrons remain at all times in two localized states, λ_A (centered at atom A) and λ_B (centered at atom B). For the moment we label two qubit carriers by 2 and 3 (we shall account for the indistinguishability of the electrons later); if using x labels the spatial and spin coordinates of electrons, the possible wave functions of two qubits are then three singlets:

$$\Lambda^1_{singlet}(x_2,x_3) = \lambda_A(\vec{r}_2)\lambda_A(\vec{r}_3)\frac{1}{\sqrt{2}}(|\uparrow_2\downarrow_3\rangle - |\uparrow_3\downarrow_2\rangle) \tag{3.8}$$

$$\Lambda^2_{singlet}(x_2,x_3) = \lambda_B(\vec{r}_2)\lambda_B(\vec{r}_3)\frac{1}{\sqrt{2}}(|\uparrow_2\downarrow_3\rangle - |\uparrow_3\downarrow_2\rangle) \tag{3.9}$$

$$\Lambda^3_{singlet}(x_2,x_3) = (\lambda_A(\vec{r}_2)\lambda_B(\vec{r}_3) + \lambda_A(\vec{r}_3)\lambda_B(\vec{r}_2))\frac{1}{\sqrt{2}}(|\uparrow_2\downarrow_3\rangle - |\uparrow_3\downarrow_2\rangle), \tag{3.10}$$

and three triplets

$$\Lambda^1_{triplet}(x_2,x_3) = (\lambda_A(\vec{r}_2)\lambda_B(\vec{r}_3) - \lambda_A(\vec{r}_3)\lambda_B(\vec{r}_2))|\uparrow_2\uparrow_3\rangle \tag{3.11}$$

$$\Lambda^2_{triplet}(x_2,x_3) = (\lambda_A(\vec{r}_2)\lambda_B(\vec{r}_3) - \lambda_A(\vec{r}_3)\lambda_B(\vec{r}_2))\frac{1}{\sqrt{2}}(|\uparrow_2\downarrow_3\rangle + |\uparrow_3\downarrow_2\rangle) \tag{3.12}$$

$$\Lambda^3_{triplet}(x_2,x_3) = (\lambda_A(\vec{r}_2)\lambda_B(\vec{r}_3) - \lambda_A(\vec{r}_3)\lambda_B(\vec{r}_2))|\downarrow_2\downarrow_3\rangle \tag{3.13}$$

In practice, the configurations in which both qubit electrons reside on the same atom have much higher energy, so we shall neglect the first and second ('ionic') singlet states listed above. These wave functions above are not normalized.

Because the system Hamiltonian does not contain any spin operator (assuming we can neglect spin-orbit coupling and dipolar interaction), the total spin S is a good quantum number. Therefore, all the three electron spins including two qubit and one control form an octet, consisting of one quartet and two doublets. The quartet reads

$$|3/2,3/2\rangle_{1,2,3} = |\uparrow_1\uparrow_2\uparrow_3\rangle; \tag{3.14}$$

$$|3/2,1/2\rangle_{1,2,3} = \frac{1}{\sqrt{3}}(|\uparrow_1\uparrow_2\downarrow_3\rangle + |\uparrow_1\downarrow_2\uparrow_3\rangle + |\downarrow_1\uparrow_2\uparrow_3\rangle) \tag{3.15}$$

$$|3/2,-1/2\rangle_{1,2,3} = \frac{1}{\sqrt{3}}(|\downarrow_1\uparrow_2\downarrow_3\rangle + |\downarrow_1\downarrow_2\uparrow_3\rangle + |\uparrow_1\downarrow_2\downarrow_3\rangle) \tag{3.16}$$

$$|3/2,-3/2\rangle_{1,2,3} = |\downarrow_1\downarrow_2\downarrow_3\rangle. \tag{3.17}$$

One doublet is formed from the triplet states of two qubits:

$$|1/2,1/2\rangle^1_{1,2,3} = \frac{1}{\sqrt{6}}(|\uparrow_1\uparrow_2\downarrow_3\rangle + |\uparrow_1\downarrow_2\uparrow_3\rangle - 2|\downarrow_1\uparrow_2\uparrow_3\rangle) \tag{3.18}$$

$$|1/2,-1/2\rangle^1_{1,2,3} = \frac{1}{\sqrt{6}}(|\downarrow_1\uparrow_2\downarrow_3\rangle + |\downarrow_1\downarrow_2\uparrow_3\rangle - 2|\uparrow_1\downarrow_2\downarrow_3\rangle), \tag{3.19}$$

while the other doublet is formed from the singlet state of two qubits:

$$|1/2,1/2\rangle^0_{1,2,3} = \frac{1}{\sqrt{2}}(|\uparrow_1\uparrow_2\downarrow_3\rangle - |\uparrow_1\downarrow_2\uparrow_3\rangle) \tag{3.20}$$

$$|1/2,-1/2\rangle^0_{1,2,3} = \frac{1}{\sqrt{2}}(|\downarrow_1\uparrow_2\downarrow_3\rangle - |\downarrow_1\downarrow_2\uparrow_3\rangle). \tag{3.21}$$

We shall neglect correlations between the control electron and the qubit electrons, so the simplest three-electron trial wave functions are

$$\Psi^1_{total}(x_1,x_2,x_3) = \hat{A}[\psi_C(\vec{r_1})(\lambda_A(\vec{r_2})\lambda_B(\vec{r_3}) - \lambda_A(\vec{r_3})\lambda_B(\vec{r_2}))|3/2,M_s\rangle_{1,2,3}] \tag{3.22}$$

$$\Psi^2_{total}(x_1,x_2,x_3) = \hat{A}[\psi_C(\vec{r_1})(\lambda_A(\vec{r_2})\lambda_B(\vec{r_3}) - \lambda_A(\vec{r_3})\lambda_B(\vec{r_2}))|1/2,m_s\rangle^1_{1,2,3}] \tag{3.23}$$

$$\Psi^3_{total}(x_1,x_2,x_3) = \hat{A}[\psi_C(\vec{r_1})(\lambda_A(\vec{r_2})\lambda_B(\vec{r_3}) + \lambda_A(\vec{r_3})\lambda_B(\vec{r_2}))|1/2,m_s\rangle^0_{1,2,3}], \tag{3.24}$$

where $\hat{A}$ is the antisymmetrizing operator. These wave functions are un-normalized. M_s could be $\pm 1/2, \pm 3/2$, and m_s could be $\pm 1/2$.

3.2.5 Calculation of expectation value

We perform a variational calculation using undetermined multiplier methods to minimize the expectation values of the system hamiltonian,

$$E_i = \langle\Psi^i_{total}|\hat{H}|\Psi^i_{total}\rangle \tag{3.25}$$

$$S_i = \langle\psi^i_{total}|\psi^i_{total}\rangle \tag{3.26}$$

$$\frac{\partial E_i}{\partial \alpha_i} + \lambda\frac{\partial S_i}{\partial \alpha_i} = 0 \tag{3.27}$$

$$\frac{\partial E_i}{\partial \beta_i} + \lambda\frac{\partial S_i}{\partial \beta_i} = 0 \tag{3.28}$$

$$\frac{\partial E_i}{\partial \gamma_i} + \lambda\frac{\partial S_i}{\partial \gamma_i} = 0 \tag{3.29}$$

$$i = 1,2,3, \tag{3.30}$$

This yields values for three sets of variational parameters $(\alpha_i, \beta_i, \gamma_i)$. Once we know the energy spectrum of the spin octet, we can use this spectrum to extract the exchange constants in the effective hamiltonian [44] which describe the coupling strength of each pair of electron spins.

The effective Hamiltonian for three electrons must take the form

$$\hat{H}_{eff} = J_{CQA}\vec{\sigma}_A \cdot \vec{\sigma}_C + J_{CQB}\vec{\sigma}_B \cdot \vec{\sigma}_C + J_{QQ}\vec{\sigma}_A \cdot \vec{\sigma}_B, \tag{3.31}$$

because this is the most general form for three spin-$\frac{1}{2}$ objects that is invariant under spin-rotation and time-reversal. So we need to find out the relationship between

energy spectra and exchange couplings in which the effective spin Hamiltonian can reproduce the spectra. Let's define

$$\bar{\epsilon} = (4E_1 + 2E_2 + 2E_3)/8 \tag{3.32}$$

$$\epsilon = E_1 - \bar{\epsilon} \tag{3.33}$$

$$\delta = E_2 - E_3. \tag{3.34}$$

By solving the eigenvalue problem of the effective spin Hamiltonian we can find

$$J_{CQA} + J_{CQB} + J_{QQ} = \epsilon \tag{3.35}$$

$$J_{CQA} = \zeta + \eta + \frac{1}{3}\epsilon \tag{3.36}$$

$$J_{CQB} = \zeta - \eta + \frac{1}{3}\epsilon, \tag{3.37}$$

meanwhile η and ζ have to satisfy

$$3\eta^2 + 9\zeta^2 = \frac{\delta^2}{16}. \tag{3.38}$$

If we assume $J_{CQA} = J_{CQB} = J_{CQ}$, from the above relationships we can calculate the exchange constants in the effective Hamiltonian using the spectra.

$$\zeta = -\delta/12 \tag{3.39}$$

$$J_{CQ} = \zeta + \epsilon/3 \tag{3.40}$$

$$J_{QQ} = \epsilon/3 - 2\zeta. \tag{3.41}$$

3.2.6 Three-donor calculation results

To be specific, we shall assume that C is on the perpendicular bisector of the straight line connecting qubits AB (see Figure 3.3). Our method is general enough to treat other cases but this choice has the advantage that the system retains a mirror plane, so the spatial states of the system can be labeled by parity. In particular, doublet formed by the singlet of qubits and doublet formed by the triplet of qubits can not be mixed, since the former is even but the latter is odd under the mirror reflection.

In the same way as done in section(3.2.2), we can find the first excited states using a δ-potential central cell correction for the $\nu_g = 0.7, 0.8, 0.9, 1.0$ respectively.

ν_g	0.7	0.8	0.9	1.0
ν_x	1.70790	1.80317	1.90069	2.0

For reference, the value of ν corresponding to Bi:Si (a deep impurity) is approximately $\nu_{\mathrm{Bi}} \approx 0.7$, whereas for P (a shallow impurity) we have $\nu_{\mathrm{P}} \approx 1$.

We also select certain Whittaker functions with a wide range of ν_c as the wave functions centered at control atom which correspond to a range of defects from deep to shallow.

ν_c	0.7	1.0	1.3	1.6	1.9	2.2	2.5	2.8	3.1	3.4

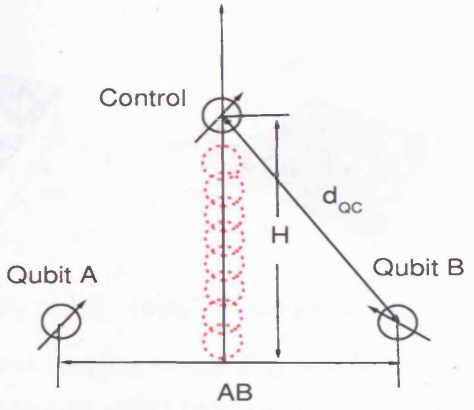

Fig. 3.3: The configuration of atoms we consider is shown. We assume that we fix A and B atoms and move away the 'control' atom. The 'control' atom is on the perpendicular bisector of AB. H is the height of the control atom. And $AB = D$ is the the distance between atom A and B.

A. Effect of dopant positioning

First, we show the behavior of J_{CQ}: Figure 3.4 shows how this coupling varies as the qubit-qubit distance D varies from $5\,a_0^*$ to $20\,a_0^*$, and the height H of the triangle formed by the qubits and control varies over the same range. We have chosen three different combinations of energies for the qubit and control states: in Figure 3.4(a) both the control and qubits correspond to a deep impurity ($\nu_g = \nu_c = 0.7$). In Figure 3.4(b) the qubit level has been made slightly shallower ($\nu_g = 0.8$), and the control level significantly shallower ($\nu_c = 1.6$), while in Figure 3.4(c) both states are significantly more delocalized($\nu_g = 0.9, \nu_c = 3.4$). As we expected, the magnitude of J_{CQ} becomes smaller and smaller when the height of the control atom H or the qubit-qubit distance D increases. And as the qubit states and control states become delocalized, the maximum of the control-qubit couplings becomes larger.

We also plot J_{QQ}, α^2 in Figure 3.5 and Figure 3.6. As expected J_{QQ} returns to the value in the absence of the control atom when the control moves away. This will be discussed later. α^2 is the probability to find the control electron on the control atom (see Ansatz 3.7). From Figure 3.6 we can see that as the control electron becomes delocalized, the charge will transfer from control atom to qubit atoms in the intermediate distance of H. This will also modify J_{QQ} significantly.

In addition, we plot the ratio of J_{QQ} to J_{CQ} in Figure 3.7. We can see that

- J_{QQ} reduces to the two-centre Heitler-London exchange value when the control

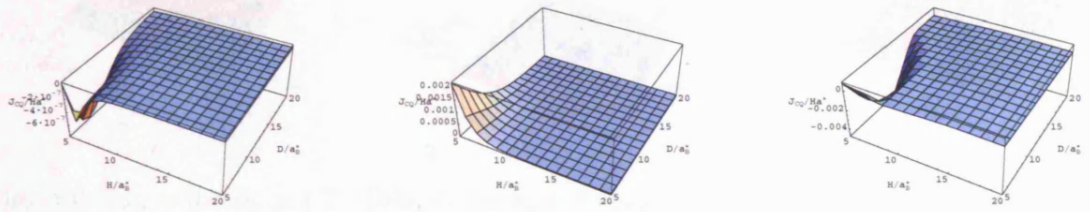

(a)$\nu_c = 0.7, \nu_g = 0.7, \nu_x \simeq 1.7$ (b)$\nu_c = 1.6, \nu_g = 0.8, \nu_x \simeq 1.8$ (c)$\nu_c = 3.4, \nu_g = 0.9, \nu_x \simeq 1.9$

Fig. 3.4: The control-qubit coupling energy J_{CQ} as a function of D and H for three different sets of quantum defect parameters. The donor distance D is from 5.0 to $20.0a_0^*$; the triangle height H also varies from 5.0 to $20.0a_0^*$. The values of the quantum defect parameters ν_c, ν_g, ν_x are shown below each plot.

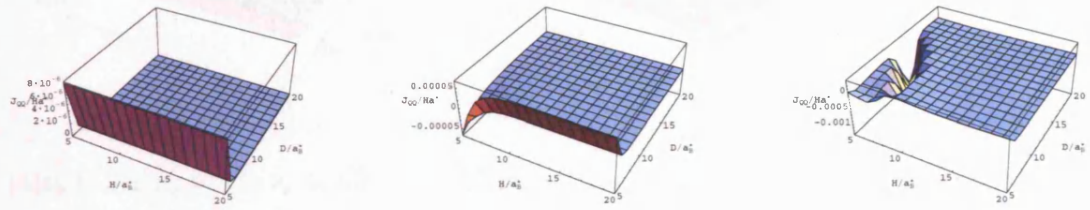

(a)$\nu_c = 0.7, \nu_g = 0.7, \nu_x \simeq 1.7$ (b)$\nu_c = 1.6, \nu_g = 0.8, \nu_x \simeq 1.8$ (c)$\nu_c = 3.4, \nu_g = 0.9, \nu_x \simeq 1.9$

Fig. 3.5: The qubit-qubit coupling energy J_{QQ} for the same parameters used in Figure 3.4 as a function of D and H is plotted.

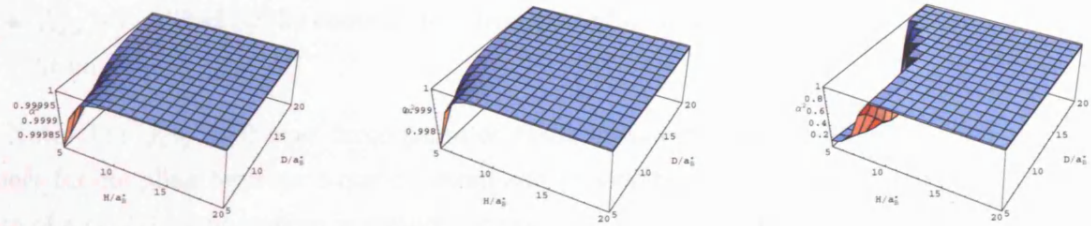

(a)$\nu_c = 0.7, \nu_g = 0.7, \nu_x \simeq 1.7$ (b)$\nu_c = 1.6, \nu_g = 0.8, \nu_x \simeq 1.8$ (c)$\nu_c = 3.4, \nu_g = 0.9, \nu_x \simeq 1.9$

Fig. 3.6: The probability α_1^2 of finding the control electron on the control site as a function of D and H is plotted using the same parameters in Figure 3.4.

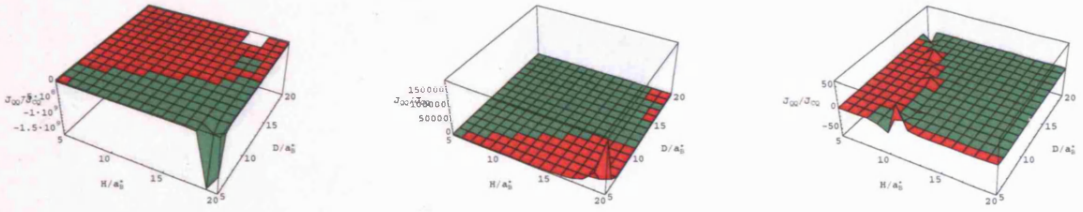

(a)$\nu_c = 0.7, \nu_g = 0.7, \nu_x \simeq 1.7$ (b)$\nu_c = 1.6, \nu_g = 0.8, \nu_x \simeq 1.8$ (c)$\nu_c = 3.4, \nu_g = 0.9, \nu_x \simeq 1.9$

Fig. 3.7: The ratio J_{QQ}/J_{CQ} as a function of D and H for the same parameters used in Figure 3.4 is shown in a colour-coded picture which distinguishes the regions of positive and negative values using red and green colors respectively. Notice that J_{QQ} is not always neglectable.

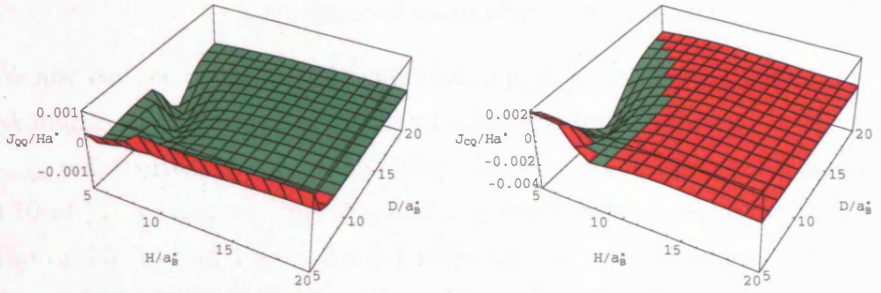

(a)$\nu_c = 3.1, \nu_g = 1.0, \nu_x \sim 2.0$ (b) $\nu_c = 3.1, \nu_g = 1.0, \nu_x \sim 2.0$

Fig. 3.8: Colour-coded plots of (a) J_{QQ} and (b) J_{CQ} as a function of D and H show FM (green) and AFM (red) regions.

atom is far from the qubits;

- J_{QQ} is not always negligible as the control electron becomes more and more delocalized
- J_{QQ} is modified by the control atom from its value in the absence of the control atom.

Note that $J_{CQ} > 0$ over large parts of the parameter space; this is what we expect for coupling between a control atom and an isolated donor, since the ground state of a two-electron system is always a singlet [43]. However, there are also significant regions in which $J_{CQ} < 0$ (ferromagnetic interactions) as shown in Figure 3.8. Similarly we found in some region $J_{QQ} < 0$ (ferromagnetic) as shown in Figure 3.8. This is our first clue that multi-site interactions are important in determining the exchange constants; this will be discussed further in the next chapter.

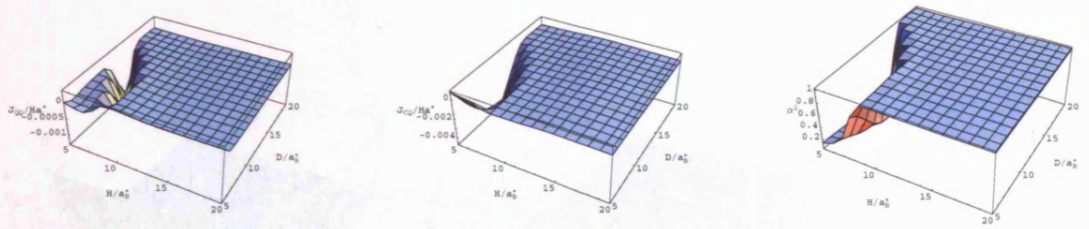

(a)$\nu_c = 3.4, \nu_g = 0.9, \nu_x \simeq 1.9$ (b)$\nu_c = 3.4, \nu_g = 0.9, \nu_x \simeq 1.9$ (c)$\nu_c = 3.4, \nu_g = 0.9, \nu_x \simeq 1.9$

Fig. 3.9: (a) J_{QQ}, (b) J_{CQ} and (c) α_1^2 as functions of D and H are plotted. Notice that the significant delocalization of control electron and the modification of J_{QQ} as shown in Figure 3.5(c). Notice that compared with Figure 3.10 J_{QQ} and J_{CQ} are modified significantly.

B. Effect of qubit-control hybridization

We also can see the significant hybridization of the control electron in Figure 3.9. For comparison we also plot the same quantities where we fix $\alpha_{1,2,3} = 1, \beta_{1,2,3} = 0$, and $\gamma_{1,2,3} = 0$ (corresponding to confining the electron to the control atom). In Figure 3.10(c),(d) we can see that J_{QQ} and J_{CQ} are modified significantly comparing with Figure 3.5 (c) and Figure 3.4 (c) when the control electron is hybridized. But in Figure 3.10(a),(b) we can see relatively small change comparing with Figure 3.5 (a) and Figure 3.4 (a).

In 3.10(a),(b) we plot J_{QQ} and J_{CQ} using the parameters in Figure 3.4(a), which corresponds to relatively localized control and qubit states. So optimization of α, β and γ in the variational calculation makes little difference until we reach combinations of control and qubit energies where it can produce significant hybridization and generate negative (FM) couplings.

In Figure 3.11, we plot J_{QQ}, J_{CQ}, α^2 as a function of ν_g and ν_c. As ν_c becomes larger, the control state is more delocalized, and we can see from (c) the charge transfers from control to qubits atoms. And the hybridization of control electron modifies the exchange couplings J_{QQ} compared with J_{QQ} without control atom.

3.3 Conclusion and discussion

By now we have presented a method to calculate the exchange interaction between three electrons in control-qubit system based on Whittaker functions. We can draw several conclusions from our calculation results:

- As expected, when the control electron is delocalized and in the middle of two qubits, the magnitude of J_{QQ} increases significantly.

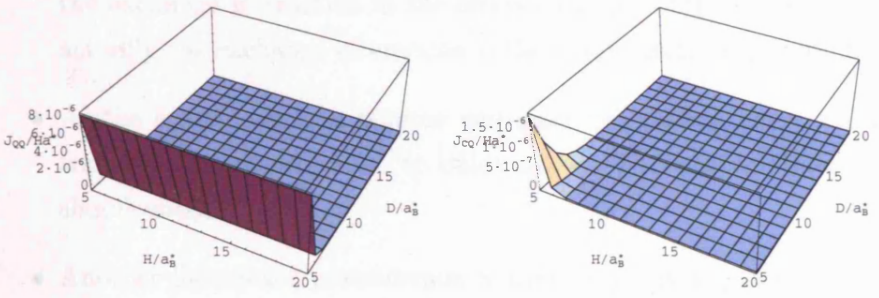

(a)$\nu_c = 0.7, \nu_g = 0.7, \nu_x \simeq 1.7$ (b)$\nu_c = 0.7, \nu_g = 0.7, \nu_x \simeq 1.7$

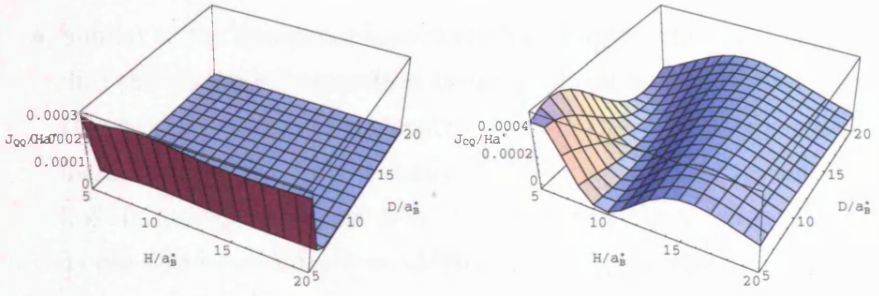

(c)$\nu_c = 3.4, \nu_g = 0.9, \nu_x \simeq 1.9$ (d)$\nu_c = 3.4, \nu_g = 0.9, \nu_x \simeq 1.9$

Fig. 3.10: (a) J_{QQ} and (b) J_{CQ} with the control electron constrained to reside on the control atom as a function of D and H are plotted using the parameter in Figure 3.4(a). (c) J_{QQ} and (d) J_{CQ} with the control electron constrained to reside on the control atom as a function of D and H are plotted using the parameter in Figure 3.4(c).

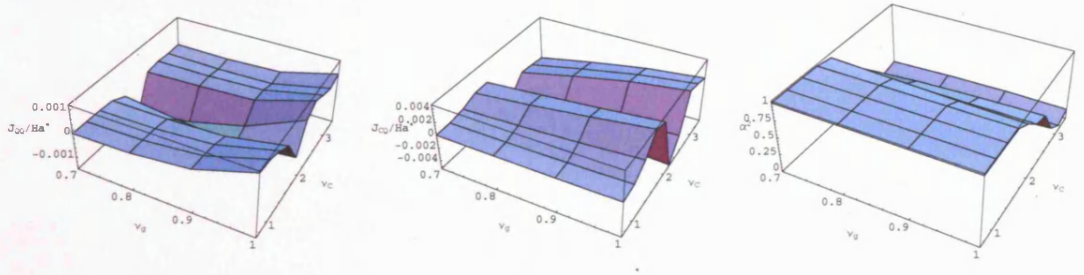

(a) (b) (c)

Fig. 3.11: Plot of (a)J_{QQ} , (b) J_{CQ} and (c) α_1^2 as a function of $\nu_g(0.7-1.0)$ and $\nu_c(0.7-3.4)$ at fixed positions ($D = 5.0a_0^*, H = 5.0a_0^*$). Notice that when the control electron is more and more delocalized, it will be hybridized more and more.

- As the control atom moves further and further away, J_{QQ} returns gradually to the exchange interaction in the absence of the control atom. This is because actually the exchange interaction is the static electronic interaction.

- As the control electron is more and more delocalized, there will be a charge transfer from control atom to qubit atoms. This also modifies J_{QQ} and J_{CQ} significantly.

- Another interesting phenomenon is that J_{QQ} and J_{CQ} can be ferromagnetic. Multi-site interactions are important in determining the exchange constants. This will be discussed in the next chapter.

- Similar to the two-donor case in the last chapter, the multi-valley terms will go into the exchange interaction between silicon donors of control-qubit system. Due to the presence of the control atom in this system, the multi-valley terms include both $e^{i(\vec{k}^{(i)}-\vec{k}^{(j)})\cdot\vec{R}_{QQ}}$ and $e^{i(\vec{k}^{(i)}-\vec{k}^{(j)})\cdot\vec{R}_{QC}}$, where $\vec{R}_{QQ}$ and $\vec{R}_{QC}$ are vectors linking two qubit atoms and one qubit and the control atom, respectively. These terms will introduce additional oscillating effects.

4. EXCHANGE CALCULATIONS BASED ON PERTURBATION THEORY

4.1 Introduction

In the beginning of this chapter up to §4.3 we describe a perturbation calculation of hydrogenic two-centre exchange. We first derive a novel perturbation theory which includes the overlaps between hydrogenic orbitals and the configuration where two electrons are centred at the same atom; this configuration was not included in the Heitler-London model. Our derivation is more general than the standard time-independent perturbation theory because we have to take into account orbital overlaps in the explicit exchange calculation. By using this perturbation theory derivative up to second order we can find the energy shifts of the singlet and triplet states which correspond to those in the Heitler-London model. We find the second order terms of the energy shifts give us an extra term for the exchange interaction. We also compare this second-order exchange splitting with the Heitler-London expression numerically. We find this second-order term appears anti-ferromagnetic in our sign convention, and it can not always be ignored.

After describing our two-centre perturbation calculation, we will introduce a 3-centre Green's function perturbation exchange calculation from §4.4. In the last chapter, we performed a variational calculation of the exchange couplings between each pair of electrons in the control-qubit system based on the Heisenberg spin Hamiltonian and Heitler-London approximation. We found that the exchange coupling between qubits (J_{QQ}) becomes larger when the control atom is in some particular position than without the control atom. We also found that when the control atom is very far away from the qubits, J_{QQ} returns to its value in the two-centre two-electron case. In addition, we found regions of the parameters where the exchange couplings are negative (ferromagnetic, in our sign convention). This is very interesting because exchange coupling in the ground state of a two-electron system (e.g. H_2 molecule) is definitely positive unless there is an orbital degeneracy [43] as we discussed in chapter 2. Although there is no theorem to say that all the exchange couplings in a three-electron system must be positive, we would like to understand the physical mechanism for these ferromagnetic couplings and at the same time

provide a check on whether our calculation is sensible. Therefore, in this chapter we use Green's function perturbation theory to calculate three-body and four-body super-exchange from a simple model.

4.2 Perturbation theory in the presence of a change in overlap

When we bring two H atoms together, we not only change the Hamiltonian but also the overlap between the one-electron states. We can represent this by writing

$$\hat{H} = \hat{H}_0 + \lambda \hat{V}; \quad \hat{S} = \hat{1} + \lambda \hat{s}. \tag{4.1}$$

Here $\hat{H}_0$ is the Hamiltonian for the two H atoms at infinite separation, where (since the states are orthogonal) the overlap operator is the identity. Both here and in what follows we will use the 'hats' as shorthand to denote the unperturbed Hamiltonian, the perturbation, and overlap operators.

We now look for solutions of the generalised eigenvalue equation

$$\hat{H}|\psi_n\rangle = E_n \hat{S}|\psi_n\rangle, \tag{4.2}$$

where we expand

$$E_n = E_n^{(0)} + \lambda E_n^{(1)} + \lambda^2 E_n^{(2)} + \mathrm{O}(\lambda^3); \tag{4.3}$$

$$|\psi_n\rangle = |\psi_n^{(0)}\rangle + \lambda|\psi_n^{(1)}\rangle + \lambda^2|\psi_n^{(2)}\rangle + \mathrm{O}(\lambda^3). \tag{4.4}$$

Collecting terms of order λ and using the shorthand $|n\rangle \equiv |\psi_n^{(0)}\rangle$ for the unperturbed states, we find

$$E_n^{(1)} = \langle n|\hat{V} - E_n^{(0)}\hat{s}|n\rangle; \tag{4.5}$$

$$\langle m|\psi_n^{(1)}\rangle = \frac{\langle m|\hat{V} - E_n^{(0)}\hat{s}|n\rangle}{E_n^{(0)} - E_m^{(0)}}. \tag{4.6}$$

The terms of order λ^2 yield

$$E_n^{(2)} = \sum_{m \neq n} \frac{|\langle m|\hat{V} - E_n^{(0)}\hat{s}|n\rangle|^2}{E_n^{(0)} - E_m^{(0)}} - E_n^{(1)}\langle n|\hat{s}|n\rangle. \tag{4.7}$$

Note that in the case of a perturbation affecting only the Hamiltonian, not the overlap (i.e., $\hat{s} = 0$), the results (4.5) and (4.7) reduce to the usual ones.

4.3 Application to exchange in H_2

Suppose a and b are 1s atomic orbitals centred on the respective atoms, which are separated by distance R. We can construct an appropriately symmetrized two-particle basis consisting of three singlet states (anti-symmetric under exchange of

spins, so symmetric under spatial exchange) which are orthonormal in the limit of infinite separation:

$$\left\{ \begin{array}{l} \psi_{sa}(1,2) = a(1)a(2) \\ \psi_{sb}(1,2) = b(1)b(2) \\ \psi_{sc}(1,2) = \frac{1}{\sqrt{2}}[a(1)b(2) + a(2)b(1)] \end{array} \right\} \times \chi_s \tag{4.9}$$

$$\chi_s = \frac{1}{\sqrt{2}}(\uparrow_1\downarrow_2 - \downarrow_2\uparrow_1), \tag{4.10}$$

and one triplet state (which has, of course, $m = -1, 0, +1$ components):

$$\psi_t(1,2) = \frac{1}{\sqrt{2}}[a(1)b(2) - a(2)b(1)] \times \chi_t \tag{4.12}$$

$$\chi_t = \left\{ \begin{array}{l} \downarrow_1\downarrow_2 \\ \frac{1}{\sqrt{2}}(\uparrow_1\downarrow_2 + \downarrow_1\uparrow_2) \\ \uparrow_1\uparrow_2 \end{array} \right\}. \tag{4.13}$$

If we neglect spin-orbit coupling, the perturbation when we bring the atoms together is purely spatial and so the singlet and triplet sectors remain uncoupled.

4.3.1 The overlap operator

Let us define the one-electron overlap between the two states as

$$\tilde{S} \equiv \int a(1)b(1)\,\mathrm{d}[1], \tag{4.14}$$

(note that a and b are real functions). Then the matrix representation of the overlap operator, in the basis $\{\psi_{sa}, \psi_{sb}, \psi_{sc}\}$, is

$$\hat{S} = \begin{pmatrix} 1 & \tilde{S}^2 & \sqrt{2}\tilde{S} \\ \tilde{S}^2 & 1 & \sqrt{2}\tilde{S} \\ \sqrt{2}\tilde{S} & \sqrt{2}\tilde{S} & 1+\tilde{S}^2 \end{pmatrix}, \tag{4.15}$$

so

$$\lambda\hat{s} = \begin{pmatrix} 0 & \tilde{S}^2 & \sqrt{2}\tilde{S}^2 \\ \tilde{S}^2 & 0 & \sqrt{2}\tilde{S}^2 \\ \sqrt{2}\tilde{S} & \sqrt{2}\tilde{S} & \tilde{S}^2 \end{pmatrix}. \tag{4.16}$$

Meanwhile, for the triplet state,

$$\langle\psi_t|\hat{S}|\psi_t\rangle = 1 - \tilde{S}^2 \quad \Rightarrow \quad \langle\psi_t|\hat{s}|\psi_t\rangle = -\tilde{S}^2. \tag{4.17}$$

4.3.2 The Hamiltonian

We will use a notation consistent with that of Slater, except that we use true atomic units so the energy unit is the Hartree, not the Rydberg (i.e. the energy of an isolated one-electron state is $E_0 = 1/2$). Then:

$$\int a(1)b(1)\,\mathrm{d}[1] \equiv \widetilde{S} = \exp(-R)[1 + R + R^2/3]; \tag{4.18}$$

$$\int a(1)[-\frac{1}{2}\nabla_1^2]a(1)\,\mathrm{d}[1] = \frac{1}{2}; \tag{4.19}$$

$$\int a(1)[-\frac{1}{r_{1a}}]a(1)\,\mathrm{d}[1] = -1; \tag{4.20}$$

$$\int a(1)[-\frac{1}{r_{1b}}]a(1)\,\mathrm{d}[1] = J = \frac{-1}{R} + \exp(-2R)\left(1 + \frac{1}{R}\right); \tag{4.21}$$

$$\int a(1)[-\frac{1}{r_{1b}}]b(1)\,\mathrm{d}[1] = K = -\exp(-R)(1 + R); \tag{4.22}$$

$$\int a(1)[-\frac{1}{2}\nabla_1^2]b(1)\,\mathrm{d}[1] = \int a(1)[E_0 + \frac{1}{r_{1b}}]b(1)\,\mathrm{d}[1] = \frac{-\widetilde{S}}{2} - K; \tag{4.23}$$

$$\int a^2(1)b^2(2)\frac{1}{r_{12}}\,\mathrm{d}[1]\mathrm{d}[2] \equiv J'; \tag{4.24}$$

$$\int a(1)b(1)a(2)b(2)\frac{1}{r_{12}}\,\mathrm{d}[1]\mathrm{d}[2] \equiv K'; \tag{4.25}$$

$$\int a^2(1)a(2)b(2)\frac{1}{r_{12}}\,\mathrm{d}[1]\mathrm{d}[2] \equiv L; \tag{4.26}$$

$$\int a^2(1)a^2(2)\frac{1}{r_{12}}\,\mathrm{d}[1]\mathrm{d}[2] = U = \lim_{R\to 0} J' = \frac{5}{8}. \tag{4.27}$$

Then the singlet part of the Hamiltonian, once again in the basis $\{\psi_{sa}, \psi_{sb}, \psi_{sc}\}$, is

$$\hat{H}_s = \begin{pmatrix} -1 + 2J + U + (1/R) & -\widetilde{S}^2 + 2K\widetilde{S} + J' + (\widetilde{S}^2/R) & \sqrt{2}(-\widetilde{S} + K + J\widetilde{S} + L + (\widetilde{S}/R)) \\ -\widetilde{S}^2 + 2K\widetilde{S} + J' + (\widetilde{S}^2/R) & -1 + 2J + U + (1/R) & \sqrt{2}(-\widetilde{S} + K + J\widetilde{S} + L + (\widetilde{S}/R)) \\ \sqrt{2}(-\widetilde{S} + K + J\widetilde{S} + L + (\widetilde{S}/R)) & \sqrt{2}(-\widetilde{S} + K + J\widetilde{S} + L + (\widetilde{S}/R)) & -1 + 2J + J' - \widetilde{S}^2 + 2K\widetilde{S} + K' + (1 + \widetilde{S}^2)/R \end{pmatrix}. \tag{4.28}$$

The triplet part is

$$\langle\psi_t|\hat{H}|\psi_t\rangle = -1 + 2J + J' + (1/R) + \widetilde{S}^2 - 2K\widetilde{S} - K' + \widetilde{S}^2/R. \tag{4.29}$$

4.3.3 Perturbation theory—definition 1

The first way of defining perturbation theory would be to take $\hat{H}_0$ as the Hamiltonian of two uncoupled H atoms (i.e. at $R \to \infty$):

$$\hat{H}_{0s} = \begin{pmatrix} -1 + U & 0 & 0 \\ 0 & -1 + U & 0 \\ 0 & 0 & -1 \end{pmatrix}; \tag{4.30}$$

$$\hat{V}_s = \begin{pmatrix} 2J + (1/R) & -\widetilde{S}^2 + 2K\widetilde{S} + J' + (\widetilde{S}^2/R) & \sqrt{2}(-\widetilde{S} + K + J\widetilde{S} + L + (\widetilde{S}/R)) \\ -\widetilde{S}^2 + 2K\widetilde{S} + J' + (\widetilde{S}^2/R) & 2J + (1/R) & \sqrt{2}(-\widetilde{S} + K + J\widetilde{S} + L + (\widetilde{S}/R)) \\ \sqrt{2}(-\widetilde{S} + K + J\widetilde{S} + L + (\widetilde{S}/R)) & \sqrt{2}(-\widetilde{S} + K + J\widetilde{S} + L + (\widetilde{S}/R)) & 2J + J' - \widetilde{S}^2 + 2K\widetilde{S} + K' + (1 + \widetilde{S}^2)/R \end{pmatrix} \tag{4.31}$$

The matrix elements for the triplet state, meanwhile, are

$$\langle\psi_t|\hat{H}_0|\psi_t\rangle = -1; \tag{4.32}$$

$$\langle\psi_t|\hat{V}|\psi_t\rangle = 2J + J' + \widetilde{S}^2 - 2K\widetilde{S} - K' + \frac{(1 - \widetilde{S}^2)}{R}. \tag{4.33}$$

With this definition, the first-order shifts to E_c (the lowest singlet state) and E_t are

$$E_c^{(1)} = 2J + J' + 2K\tilde{S} + K' + \frac{(1+\tilde{S}^2)}{R}; \quad (4.34)$$

$$E_t^{(1)} = 2J + J' - 2K\tilde{S} - K' + \frac{(1-\tilde{S}^2)}{R}. \quad (4.35)$$

The second-order shifts are

$$E_c^{(2)} = \frac{-4(K + J\tilde{S} + L + \tilde{S}/R)^2}{U} - \tilde{S}^2[2J + J' + 2K\tilde{S} + K' + \frac{(1+\tilde{S}^2)}{R}] \quad (4.36)$$

$$E_t^{(2)} = +\tilde{S}^2[2J + J' - 2K\tilde{S} - K' + \frac{(1-\tilde{S}^2)}{R}]. \quad (4.37)$$

Hence, the exchange is

$$J = E_t - E_c = -4K\tilde{S} - 2K' + \tilde{S}^2(4J + 2J') + \frac{4[K + L + \tilde{S}(J + 1/R)]^2}{U} + O(\lambda^3). \quad (4.38)$$

4.3.4 Perturbation theory—definition 2

The second way of defining the perturbation theory is to include in $\hat{H}_0$ all the energy shifts arising from the field of one atom acting at the site of the other, and to reserve for $\hat{V}$ only those terms which actually transfer electrons between the two sites. This yields:

$$\hat{H}_{0s} = \begin{pmatrix} -1 + 2J + U + 1/R & 0 & 0 \\ 0 & -1 + 2J + U + 1/R & 0 \\ 0 & 0 & -1 + 2J + J' + 1/R \end{pmatrix}; \quad (4.39)$$

$$\hat{V}_s = \begin{pmatrix} 0 & -\tilde{S}^2 + 2K\tilde{S} + J' + (\tilde{S}^2/R) & \sqrt{2}(-\tilde{S} + K + J\tilde{S} + L + (\tilde{S}/R)) \\ -\tilde{S}^2 + 2K\tilde{S} + J' + (\tilde{S}^2/R) & 0 & \sqrt{2}(-\tilde{S} + K + J\tilde{S} + L + (\tilde{S}/R)) \\ \sqrt{2}(-\tilde{S} + K + J\tilde{S} + L + (\tilde{S}/R)) & \sqrt{2}(-\tilde{S} + K + J\tilde{S} + L + (\tilde{S}/R)) & -\tilde{S}^2 + 2K\tilde{S} + K' + \tilde{S}^2/R \end{pmatrix} \quad (4.40)$$

Now the matrix element for the triplet state is

$$\langle\psi_t|\hat{H}_0|\psi_t\rangle = -1 + 2J + J' + \frac{1}{R}; \quad (4.41)$$

$$\langle\psi_t|\hat{V}|\psi_t\rangle = \tilde{S}^2 - 2K\tilde{S} - K' - \frac{\tilde{S}^2}{R}. \quad (4.42)$$

The first-order shifts are now

$$E_c^{(1)} = 2K\tilde{S} + K' - \tilde{S}^2(2J + J'); \quad (4.43)$$

$$E_t^{(1)} = -2K\tilde{S} - K' + \tilde{S}^2(2J + J'), \quad (4.44)$$

and the second-order shifts are

$$E_c^{(2)} = \frac{-4(K + J\tilde{S} + L + \tilde{S}/R)^2}{(U - J')} - \tilde{S}^2[(2J + J')\tilde{S}^2 + 2K\tilde{S} + K']; \quad (4.45)$$

$$E_t^{(2)} = +\tilde{S}^2[-2K\tilde{S} - K' + \tilde{S}^2(2J + J')]. \quad (4.46)$$

Thus the exchange is

$$J = E_t - E_c = -4K\tilde{S} - 2K' + \tilde{S}^2(4J + 2J') + \frac{4[K + L - \tilde{S}(J + J')]^2}{U - J'} + O(\lambda^3). \quad (4.47)$$

4.3.5 Comparing the two perturbation theories, and the Heitler-London result

The Heitler-London formula for the exchange, obtained from the *ansatz* that the triplet-state wavefunction is precisely ψ_t and the singlet-state wavefunction is precisely ψ_c, is

$$J = \frac{2}{1-\tilde{S}^4}[2J\tilde{S}^2 + J'\tilde{S}^2 - 2K\tilde{S} - K']. \tag{4.48}$$

To second order in λ, it can be approximated as

$$J \approx [4J\tilde{S}^2 + 2J'\tilde{S}^2 - 4K\tilde{S} - 2K']. \tag{4.49}$$

It can immediately be seen the two perturbation theory results, equations (4.38 and 4.47), agree with one another and with the approximated Heitler-London result (4.49) to the level of the first term. The remaining terms in (4.38) and (4.47) represent the effect of changes in the wavefunctions, arising from correlations introduced by the electron-electron interactions. These corrections make the exchange more antiferromagnetic (i.e. are positive contributions, in our sign convention).

How important are these corrections? For the moment we have only calculated L numerically, by fitting the hydrogenic 1s function to a contraction of Gaussians. We can then plot the correction as a function of separation R.

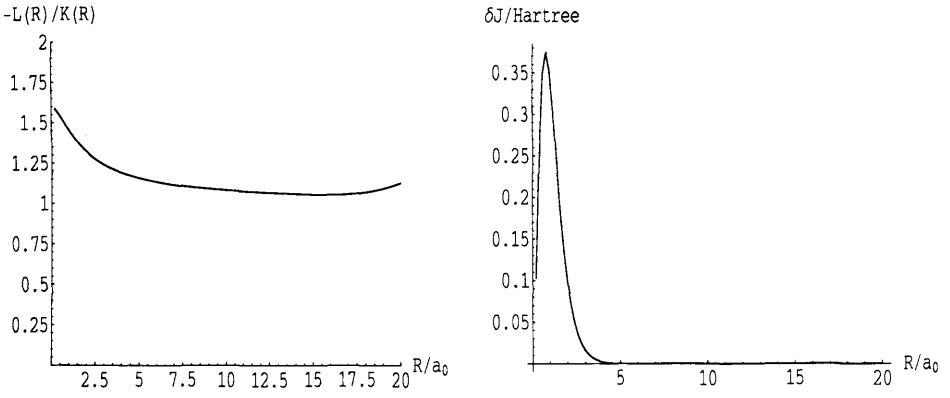

(a) (b)

Fig. 4.1: (a) The ratio of $L(R)$ to $-K(R)$ as a function of atom distance R, we can see that $L(R)$ goes to $-K(R)$ asymptotically, but the ratio at $20a_0$ is slightly different from 1 because we use the Gaussian expansion. (b) The correction term in equation 4.47 as a function of atom distance R.

From Figure 4.1, we can see that $L(R)$ goes to $-K(R)$ asymptotically. From Figure 4.2, we can see that in the region we are interested in,i.e.,$4-10$ bohr radius the second order correction term can be ignored.

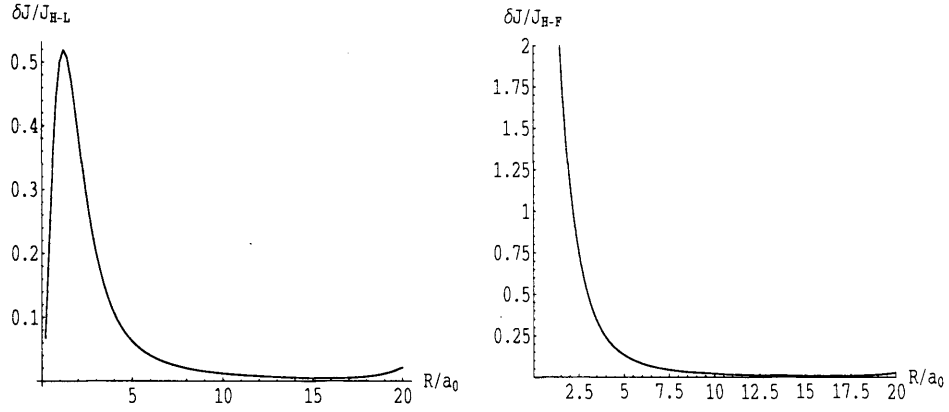

(a) (b)

Fig. 4.2: (a)Comparison between the correction term in equation 4.47 and Heitler-London exchange. The ratio of $\delta J(R)$ to $J_{H-L}(R)$ as a function of atom distance R, (b) Comparison between the correction term in equation 4.47 and Herring-Flicker asymptotic form of exchange J_{H-F}; their ratio as a function of atom distance R.

The asymptotic form of the correction can be seen as follows. $J + J'$ is the potential energy of interaction between one 1s electron and the total charge of the (neutral) other atom. We would therefore expect it to die off quickly with R, and indeed we find

$$\tilde{S}(J + J') = \frac{-R^4}{18} \exp(-3R) + \mathrm{O}(R^3 \exp(-3R)). \tag{4.50}$$

The corresponding term appearing in the first form of perturbation theory looks like

$$\tilde{S}(J + 1/R) = \frac{R^2}{3} \exp(-3R) + \mathrm{O}(R \exp(-3R)) \tag{4.51}$$

Similarly, L is the interaction of the 'exchange charge' $a(1)b(1)$ with the charge density of a neutral atom.

4.3.6 *'Exact' results*

Two exact results (in different senses) are available for this problem.

The Herring-Flicker result

This is the exact leading-order behaviour of the exchange at very large separations, calculated from the exact asymptotic solution of the two-particle Schrödinger equation in real-space (with no basis-set approximations) [36]. The result is

$$J = 4\pi^{1/2} R^{5/2} \exp(-2R) \int_0^1 \exp(-q) q^{3/2} (2 - q)^{1/2} \, \mathrm{d}q + \mathrm{O}(R^2 \exp(-2R)) \tag{4.52}$$

$$= 1.642 R^{5/2} \exp(-2R) + \mathrm{O}(R^2 \exp(-2R)). \tag{4.53}$$

The result of exact matrix diagonalization

Alternatively, one can solve exactly for the singlet and triplet energies within the basis generated by equations (4.8) and (4.11). This includes correlation effects exactly at all separations, but *only* within this restricted basis set. The singlet and triplet energies are easily found:

$$E_c^{(1)} = \frac{1}{1+\tilde{S}^2}(-(1+2\tilde{S}^2)(-1+2J+J^{'}+\frac{1}{R})+ (-\tilde{S}^2+2K\tilde{S}+K^{'}+\frac{\tilde{S}^2}{R})) \quad (4.54)$$

$$E_c^{(2)} = \frac{1}{1+\tilde{S}^2}\times\frac{4}{J^{'}-U}[K+L-(J+J^{'})\tilde{S}]^2 \quad (4.55)$$

$$E_t^{(1)} = \frac{1}{(1-\tilde{s}^2)}[(-1+2\tilde{s}^2)(-1+2J+J^{'})-(-\tilde{s}^2+2K\tilde{s}+K^{'}+\frac{\tilde{s}^2}{R})] \quad (4.56)$$

$$E_t^{(2)} = 0; \quad (4.57)$$

and the splitting can be found according to the above singlet and triplet energies:

$$E_t^{(1)}-E_c^{(1)} = \frac{2}{1-\tilde{S}^4}[2J\tilde{S}^2+J^{'}\tilde{S}^2-2K\tilde{S}-K^{'}] \quad (4.58)$$

$$E_t^{(2)}-E_c^{(2)} = \frac{1}{1+\tilde{S}^2}\times\frac{4}{-J^{'}+U}[K+L-(J+J^{'})\tilde{S}]^2. \quad (4.59)$$

Note that splitting from the first order perturbation is exactly the same as H-L exchange calculation. Therefore, the exchange splitting of two hydrogenic atoms based on second order perturbation theory takes the form of:

$$J = E_t - E_c \quad (4.60)$$

$$= \frac{2}{1-\tilde{S}^4}[2J\tilde{S}^2+J^{'}\tilde{S}^2-2K\tilde{S}-K^{'}]+ \frac{1}{1+\tilde{S}^2}\times\frac{4}{-J^{'}+U}[K+L-(J+J^{'})\tilde{S}]^2. \quad (4.61)$$

From this exact result, we can see that the second term in the right hand side is the second-order term when we consider more configurations than the Heitler-London model.

4.4 Green's function perturbation theory

We now move on from the simple case of the H_2 molecule to a perturbation treatment of the more complicated systems, containing qubits and control atoms, that were discussed in the previous Chapter. Once again we assume our system Hamiltonian can be separated into an unperturbed part of H_0, and a perturbation V

$$H = H_0 + V. \quad (4.62)$$

We assume the eigenvalues and eigenfunctions of H_0 are easily obtained. The Green's functions $G_0(z)$ and $G(z)$ corresponding to H_0 and H, respectively, are

$$G_0(z) = (z - H_0)^{-1}, \tag{4.63}$$

and

$$G(z) = (z - H)^{-1}. \tag{4.64}$$

G and G_0 are connected by the Dyson equation

$$\begin{aligned} G(z) &= [1 - G_0(z)V]^{-1} G_0(z) && (4.65)\\ &= G_0 + G_0 V G_0 + G_0 V G_0 V G_0 + \ldots, && (4.66) \end{aligned}$$

and the energy shift which can mix states into the eigen-state $|\psi_0\rangle$ of $\hat{H}_0$ due to the perturbation if we want to work with some subset of eigenfunctions of $\hat{H}_0$ is

$$\begin{aligned} \Delta\hat{H}_{eff} &= V + V\hat{P}\hat{G}_0(z)\hat{P}V && (4.67)\\ &\quad + V\hat{P}\hat{G}_0(z)\hat{P}V\hat{P}\hat{G}_0(z)\hat{P}V + \ldots, && (4.68) \end{aligned}$$

where $\hat{P}$ is the projection operator onto states kept, and the 2nd term on the right hand side is the 2nd order perturbation and the 3rd term is the 3rd order perturbation, and so on. In this formula, $\Delta\hat{H}_{eff}$ is energy dependent, so we should choose z to correspond to the energy of the states we work with.

4.5 Multi-center ring exchange

It is clear that the presence of the control atom is responsible for the ferromagnetism of J_{QQ} at intermediate separations of qubit atoms and control atom. The presence of the control atom means that multi-body exchange processes become possible in our control-qubit system model. There has been some work on the theory of multi-body exchange processes. The essential physics is roughly the same as that in our control-qubit system although the physical system previously researched on is very different from ours. Roger *et al.* [45] pointed out that, for the case of solid ^{3}He:

- Two-body exchange always leads to a Heisenberg Hamiltonian with antiferromagnetic exchange. See Figure 4.3(a).
- However, three-body ring exchange always leads to a Heisenberg Hamiltonian with ferromagnetic exchanges. See Figure 4.3(b).
- Four-body ring exchange leads to a Heisenberg Hamiltonian with anti-ferromagnetic exchanges. See Figure 4.3(c).

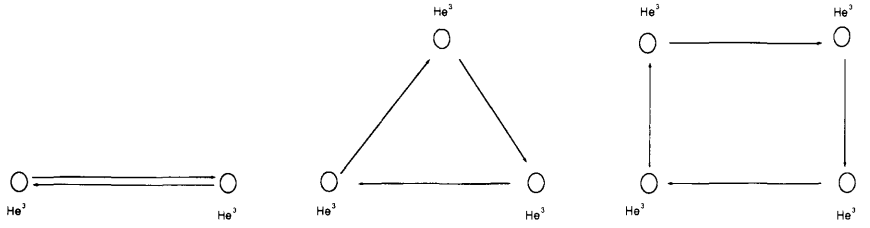

Fig. 4.3: Schematic view of possible exchange couplings between helium atoms in solid ^{3}He: (a) conventional two-body exchange (antiferromagnetic); (b) three-body ring exchange (ferromagnetic); (c) Four-body ring exchanges lead to a Heisenberg Hamiltonian with anti-ferromagnetic exchanges.

Although the solid ^{3}He system is a very different system from our control-qubit model, the central idea of multi-body ring exchange is similar in both cases. We need to include third-order and fourth-order processes in our model (see Figure 4.4) in order to capture these effects.

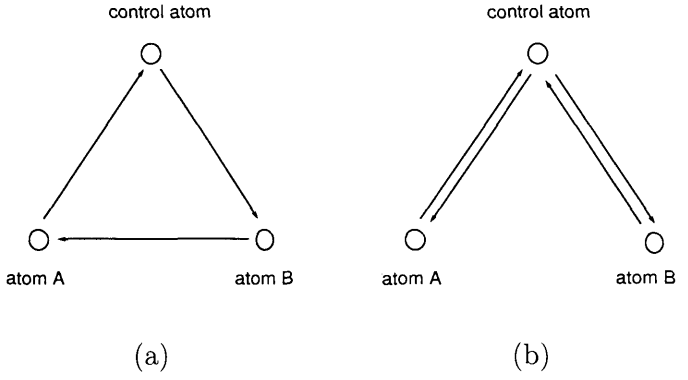

Fig. 4.4: (a) third-order exchange scheme; (b) fourth-order exchange scheme.

4.6 Perturbation theory calculations of 3-center problem

4.6.1 Matrix form of Heisenberg spin Hamiltonian

In order to calculate the exchange coupling, we need to know the matrix form of the Heisenberg spin Hamiltonian. In the following we will discuss how we reproduce the Heisenberg spin Hamiltonian and extract the exchange constants. The Heisenberg

spin Hamiltonian of the control-qubit system as cited in Chapter 3 is

$$\hat{H} = J_{QQ}\vec{S_1}\cdot\vec{S_2} + J_{CQ}(\vec{S_1}\cdot\vec{S_3} + \vec{S_2}\cdot\vec{S_3}), \tag{4.69}$$

where S_1, S_2 are the qubit spins, and S_3 is the control electron spin. The matrix form of this spin Hamiltonian that conserves the z-projection S_z of the total spin is an 8×8 matrix ($\hbar = 1$):

$$\hat{H} = \begin{array}{c} \\ |\uparrow\uparrow\uparrow\rangle \\ |\uparrow\uparrow\downarrow\rangle \\ |\uparrow\downarrow\uparrow\rangle \\ |\uparrow\downarrow\downarrow\rangle \\ |\downarrow\uparrow\uparrow\rangle \\ |\downarrow\uparrow\downarrow\rangle \\ |\downarrow\downarrow\uparrow\rangle \\ |\downarrow\downarrow\downarrow\rangle \end{array} \begin{array}{c} \begin{array}{cccccccc} |\uparrow\uparrow\uparrow\rangle & |\uparrow\uparrow\downarrow\rangle & |\uparrow\downarrow\uparrow\rangle & |\uparrow\downarrow\downarrow\rangle & |\downarrow\uparrow\uparrow\rangle & |\downarrow\uparrow\downarrow\rangle & |\downarrow\downarrow\uparrow\rangle & |\downarrow\downarrow\downarrow\rangle \end{array} \\ \begin{pmatrix} \frac{J_{CQ}}{2}+\frac{J_{QQ}}{4} & 0 & 0 & 0 & 0 & 0 & 0 & 0 \\ 0 & -\frac{J_{CQ}}{2}+\frac{J_{QQ}}{4} & \frac{J_{CQ}}{2} & 0 & \frac{J_{CQ}}{2} & 0 & 0 & 0 \\ 0 & \frac{J_{CQ}}{2} & -\frac{J_{QQ}}{4} & 0 & \frac{J_{QQ}}{2} & 0 & 0 & 0 \\ 0 & 0 & 0 & -\frac{J_{QQ}}{4} & 0 & \frac{J_{QQ}}{2} & \frac{J_{CQ}}{2} & 0 \\ 0 & \frac{J_{CQ}}{2} & \frac{J_{QQ}}{2} & 0 & -\frac{J_{QQ}}{4} & 0 & 0 & 0 \\ 0 & 0 & 0 & \frac{J_{QQ}}{2} & 0 & -\frac{J_{QQ}}{4} & J_{CQ} & 0 \\ 0 & 0 & 0 & \frac{J_{CQ}}{2} & 0 & \frac{J_{CQ}}{2} & -\frac{J_{CQ}}{2}+\frac{J_{QQ}}{4} & 0 \\ 0 & 0 & 0 & 0 & 0 & 0 & 0 & \frac{J_{CQ}}{2}+\frac{J_{QQ}}{4} \end{pmatrix} \end{array} \tag{4.70}$$

4.6.2 Simple model of the three-centreproblem

First we ignore the donor excited states to simplify calculation. We consider all processes (both single-electron terms and interactions) within one atom as contributing to the unperturbed Hamiltonian H_0, and the hopping operator V which transfers electrons between atoms as the perturbation. We divide our discussion into the following steps:

1. Select a particular eigenvalue of z-component of the total spin S_z, e.g., $S_z = \frac{1}{2}$;
2. Enumerate all the possible states for this S_z—for example, for two spin up and one spin down (i.e. $S_z = +1/2$) there are nine states as shown in Figure 4.5;
3. Construct the matrices of G_0 and V based on these states;
4. Use these matrices to calculate the 2nd, 3rd, and 4th order energy shifts;
5. Select the three lowest states which correspond to one electron on each atom and which are degenerate in the absence of the perturbation $\hat{V}$, and construct the spin Hamiltonian within this basis;
6. Identify the values J_{CQ} and J_{QQ} by comparison with the Heisenberg Hamiltonian matrix form (4.70).

First we define the second-quantized operators: $C^+_{A\sigma}$, $C_{A\sigma}$, $C^+_{B\sigma}$, $C_{B\sigma}$, $C^+_{C\sigma}$, $C_{C\sigma}$, where σ is $\uparrow$ or $\downarrow$. $C^+_{A\sigma}$ creates an electron with spin σ on atom A, $C_{A\sigma}$ annihilates an electron with spin σ on atom A, and so on. These operators satisfy

$$\{C_{i\sigma}, C^+_{j\sigma'}\} = \delta_{ij}\delta_{\sigma\sigma'}, \tag{4.71}$$

$$\{C_{i\sigma}, C_{j\sigma'}\} = 0, \tag{4.72}$$

$$\{C^+_{i\sigma}, C^+_{j\sigma'}\} = 0, \tag{4.73}$$

$$i, j = A, B, C, \tag{4.74}$$

$$\sigma, \sigma' = \uparrow, \downarrow . \tag{4.75}$$

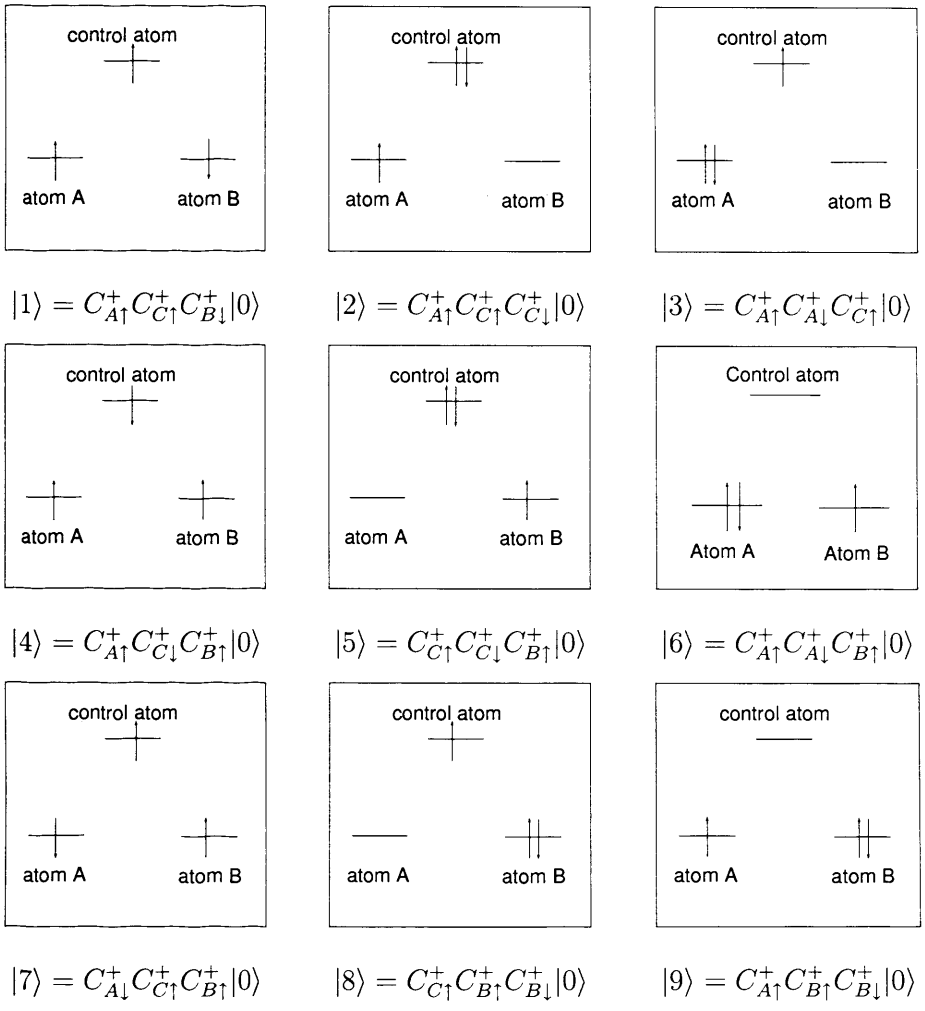

Fig. 4.5: This figure shows nine possible states with two spins up and one spin down (i.e. $S_z = 1/2$). Here $|0\rangle$ is vacuum state.

4.6.3 *Green's function perturbation theory calculation*

A. The unperturbed Hamiltonian H_0.

H_0 is the single-electron energy plus two-electron interaction within each atom. Let us consider its matrix elements among the states defined in Figure 4.5. Here we

assume that all those nine states are orthogonal to one another. If we define

$$\langle 1|\hat{H}_0|1\rangle = 0 \tag{4.76}$$
$$\langle 4|\hat{H}_0|4\rangle = 0 \tag{4.77}$$
$$\langle 7|\hat{H}_0|7\rangle = 0, \tag{4.78}$$

then

$$\langle 2|\hat{H}_0|2\rangle = \langle 5|\hat{H}_0|5\rangle = U_C - V_{QQ} \tag{4.79}$$
$$\langle 3|\hat{H}_0|3\rangle = \langle 8|\hat{H}_0|8\rangle = U_Q - V_{QQ} \tag{4.80}$$
$$\langle 6|\hat{H}_0|6\rangle = \langle 9|\hat{H}_0|9\rangle = U_Q + V_{QQ} - 2V_{CQ}, \tag{4.81}$$

and

$$U_C = \int \phi_C^2(\vec{r_1})\phi_C^2(\vec{r_2})/r_{12}d\vec{r_1}d\vec{r_2} \tag{4.82}$$
$$U_Q = \int \lambda_A^2(\vec{r_1})\lambda_A^2(\vec{r_2})/r_{12}d\vec{r_1}d\vec{r_2} \tag{4.83}$$
$$V_{QQ} = \int \lambda_A^2(\vec{r_1})\lambda_B^2(\vec{r_2})/r_{12}d\vec{r_1}d\vec{r_2} \tag{4.84}$$
$$V_{CQ} = \int \lambda_A^2(\vec{r_1})\phi_C^2(\vec{r_2})/r_{12}d\vec{r_1}d\vec{r_2} \tag{4.85}$$
$$= \int \lambda_B^2(\vec{r_1})\phi_C^2(\vec{r_2})/r_{12}d\vec{r_1}d\vec{r_2}. \tag{4.86}$$

All off-diagonal elements of $\hat{H}_0$ are zero. So the 9×9 matrix representation of H_0 is

$$H_0 = \begin{pmatrix} 0 & 0 & 0 & 0 & 0 & 0 & 0 & 0 & 0 \\ 0 & U_C - V_{QQ} & 0 & 0 & 0 & 0 & 0 & 0 & 0 \\ 0 & 0 & U_Q - V_{QQ} & 0 & 0 & 0 & 0 & 0 & 0 \\ 0 & 0 & 0 & 0 & 0 & 0 & 0 & 0 & 0 \\ 0 & 0 & 0 & 0 & U_C - V_{QQ} & 0 & 0 & 0 & 0 \\ 0 & 0 & 0 & 0 & 0 & U_Q + V_{QQ} - 2V_{CQ} & 0 & 0 & 0 \\ 0 & 0 & 0 & 0 & 0 & 0 & 0 & 0 & 0 \\ 0 & 0 & 0 & 0 & 0 & 0 & 0 & U_Q - V_{QQ} & 0 \\ 0 & 0 & 0 & 0 & 0 & 0 & 0 & 0 & U_Q + V_{QQ} - 2V_{CQ} \end{pmatrix} \tag{4.87}$$

B. The hopping operator V.

If we can neglect the effect of a magnetic field B on the orbital motion of the electrons, the hopping amplitudes t_{CQ}, t_{QQ} that respectively transfer electrons between the control atom and the qubits, and from qubit to qubit, can be chosen to be real. The definitions of t_{CQ} and t_{QQ} are

$$t_{CQ} = \langle \lambda_A|\hat{H}_{core}|\phi_C\rangle = \langle \lambda_B|\hat{H}_{core}|\phi_C\rangle, \tag{4.88}$$
$$t_{QQ} = \langle \lambda_A|\hat{H}_{core}|\lambda_B\rangle, \tag{4.89}$$

where

$$\hat{H}_{core} = \sum_{i=1}^{3} \hat{h}_i, \tag{4.90}$$
$$\hat{h}_i = -\frac{{\nabla_i}^2}{2} - \frac{1}{|\vec{r_i} - \vec{R}_C|} - \frac{1}{|\vec{r_i} - \vec{R}_A|} - \frac{1}{|\vec{r_i} - \vec{R}_B|}. \tag{4.91}$$

$$V = \sum_{\sigma}[t_{CQ}(C^{+}_{A\sigma}C_{C\sigma} + C^{+}_{C\sigma}C_{A\sigma} + C^{+}_{B\sigma}C_{C\sigma} + C^{+}_{C\sigma}C_{B\sigma}) + t_{QQ}(C^{+}_{A\sigma}C_{B\sigma} + C^{+}_{B\sigma}C_{A\sigma})]. \quad (4.92)$$

So the 9×9 matrix of V is

$$V = \begin{pmatrix} 0 & t_{CQ} & -t_{QQ} & 0 & 0 & 0 & 0 & -t_{QQ} & t_{CQ} \\ t_{CQ} & 0 & -t_{CQ} & -t_{CQ} & t_{QQ} & 0 & 0 & 0 & 0 \\ -t_{QQ} & -t_{CQ} & 0 & 0 & 0 & t_{CQ} & t_{QQ} & 0 & 0 \\ 0 & -t_{CQ} & 0 & 0 & t_{CQ} & t_{CQ} & 0 & 0 & -t_{CQ} \\ 0 & t_{QQ} & 0 & t_{CQ} & 0 & 0 & -t_{CQ} & -t_{CQ} & 0 \\ 0 & 0 & t_{CQ} & t_{CQ} & 0 & 0 & -t_{CQ} & 0 & -t_{QQ} \\ 0 & 0 & t_{QQ} & 0 & -t_{CQ} & -t_{CQ} & 0 & t_{QQ} & 0 \\ -t_{QQ} & 0 & 0 & 0 & -t_{CQ} & 0 & t_{QQ} & 0 & t_{CQ} \\ t_{CQ} & 0 & 0 & -t_{CQ} & 0 & -t_{QQ} & 0 & t_{CQ} & 0 \end{pmatrix} \quad (4.93)$$

C. Perturbation theory and reproduction of the Heisenberg spin Hamiltonian

The matrix form of H_0 is given in equation (4.87), and we can construct the corresponding matrix representation of G_0 from

$$G_0 = (\Omega \mathbf{1} - H_0)^{-1}, \quad (4.94)$$

where $\mathbf{1}$ is 9×9 identity matrix. After we project out the ground-state eigenspace, the matrix form of $(1 - \hat{P})G_0(1 - \hat{P})$ becomes

$$(1 - \hat{P})G_0(1 - \hat{P}) = \begin{pmatrix} \mathcal{G}_0^{top} & \hat{0}_{5\times 4} \\ \hat{0}_{4\times 5} & \mathcal{G}_0^{bottom} \end{pmatrix}, \quad (4.95)$$

where

$$\mathcal{G}_0^{top} = \begin{pmatrix} 0 & 0 & 0 & 0 & 0 \\ 0 & (\Omega - (UC - V_{QQ}))^{-1} & 0 & 0 & 0 \\ 0 & 0 & (\Omega - (U_Q - V_{QQ}))^{-1} & 0 & 0 \\ 0 & 0 & 0 & 0 & 0 \\ 0 & 0 & 0 & 0 & (\Omega - (UC - V_{QQ}))^{-1} \end{pmatrix}, \quad (4.96)$$

and

$$\mathcal{G}_0^{bottom} = \begin{pmatrix} (\Omega - (U_Q + V_{QQ} - 2V_{CQ}))^{-1} & 0 & 0 & 0 \\ 0 & 0 & 0 & 0 \\ 0 & 0 & (\Omega - (U_Q - V_{QQ}))^{-1} & 0 \\ 0 & 0 & 0 & (\Omega - (U_Q + V_{QQ} - 2V_{CQ}))^{-1} \end{pmatrix} \quad (4.97)$$

Now we can find the second-order, third-order, and fourth-order perturbations:

$$\Delta H^{(2)}_{eff} = V(1 - \hat{P})G_0(1 - \hat{P})V \quad (4.98)$$

$$\Delta H^{(3)}_{eff} = V(1 - \hat{P})G_0(1 - \hat{P})V((1 - \hat{P})G_0(1 - \hat{P})V \quad (4.99)$$

$$\Delta H^{(4)}_{eff} = V((1 - \hat{P})G_0(1 - \hat{P})V(1 - \hat{P})G_0(1 - \hat{P})V(1 - \hat{P})G_0(1 - \hat{P})V \quad (4.100)$$

Therefore, we seek values of J_{QQ} and J_{CQ} such that the expressions (4.98-4.100) reproduce the spin Hamiltonian (4.70). The states defined as $|1\rangle$, $|4\rangle$ and $|7\rangle$ in

Figure 4.5 form an invariant subspace with $M_S = +1/2$ both in the Heisenberg spin Hamiltonian matrix (4.70) and in the matrices $\Delta H_{eff}^{(2),(3),(4)}$. We extract these 3×3 sub-matrices from the Heisenberg spin Hamiltonian and $\Delta H_{eff}^{(2),(3),(4)}$ matrices (4.98-4.100), and compare them. We remove constant energy shifts by making the trace of each matrix zero. The traceless matrix extracted from the Heisenberg spin Hamiltonian is

$$\begin{array}{c} \\ |1\rangle \\ |4\rangle \\ |7\rangle \end{array} \begin{array}{c} \begin{array}{ccc} |1\rangle & |4\rangle & |7\rangle \end{array} \\ \begin{pmatrix} \frac{J_{CQ}-J_{QQ}}{6} & \frac{J_{CQ}}{2} & \frac{J_{QQ}}{2} \\ \frac{J_{CQ}}{2} & \frac{J_{QQ}-J_{CQ}}{3} & \frac{J_{CQ}}{2} \\ \frac{J_{QQ}}{2} & \frac{J_{CQ}}{2} & \frac{J_{CQ}-J_{QQ}}{6} \end{pmatrix} \end{array}. \tag{4.101}$$

Comparing this matrix with the matrix spanned by $|1\rangle, |4\rangle$, and $|7\rangle$ calculated by perturbation theory, we find that they are equal provided that

$$\begin{aligned} J_{CQ}^{(2)} &= 2t_{CQ}^2(-\frac{1}{\Omega - U_C + V_{QQ}} + \\ &\quad \frac{1}{-\Omega + U_Q - 2V_{CQ} + V_{QQ}}) \end{aligned} \tag{4.102}$$

$$J_{QQ}^{(2)} = \frac{-2t_{QQ}^2}{\Omega - U_Q + V_{QQ}}. \tag{4.103}$$

Similarly, we can find the third-order and fourth-order contributions to J_{QQ}, J_{CQ}:

$$\begin{aligned} J_{QQ}^{(3)} &= 2(\frac{{t_{CQ}}^2 t_{QQ}}{(\Omega - U_Q + 2V_{CQ} - V_{QQ})(\Omega - U_Q + V_{QQ})} - \frac{{t_{CQ}}^2 t_{QQ}}{(\Omega - U_C + V_{QQ})(\Omega - U_Q + V_{QQ})} \\ &\quad - \frac{t_{CQ}\left(-\left(\frac{t_{CQ}t_{QQ}}{\Omega - U_Q + 2V_{CQ} - V_{QQ}}\right) - \frac{t_{CQ}t_{QQ}}{\Omega - U_Q + V_{QQ}}\right)}{\Omega - U_Q + 2V_{CQ} - V_{QQ}} - \frac{t_{CQ}\left(\frac{t_{CQ}t_{QQ}}{\Omega - U_C + V_{QQ}} + \frac{t_{CQ}t_{QQ}}{\Omega - U_Q + V_{QQ}}\right)}{\Omega - U_C + V_{QQ}}) \end{aligned} \tag{4.104}$$

$$\begin{aligned} J_{CQ}^{(3)} &= 2(\frac{{t_{CQ}}^2 t_{QQ}}{(\Omega - U_Q + 2V_{CQ} - V_{QQ})(\Omega - U_Q + V_{QQ})} - \frac{{t_{CQ}}^2 t_{QQ}}{(\Omega - U_C + V_{QQ})(\Omega - U_Q + V_{QQ})} \\ &\quad + \frac{t_{CQ}\left(-\left(\frac{t_{CQ}t_{QQ}}{\Omega - U_Q + 2V_{CQ} - V_{QQ}}\right) - \frac{t_{CQ}t_{QQ}}{\Omega - U_Q + V_{QQ}}\right)}{\Omega - U_Q + 2V_{CQ} - V_{QQ}} + \frac{t_{CQ}\left(\frac{t_{CQ}t_{QQ}}{\Omega - U_C + V_{QQ}} + \frac{t_{CQ}t_{QQ}}{\Omega - U_Q + V_{QQ}}\right)}{\Omega - U_C + V_{QQ}}) \end{aligned} \tag{4.105}$$

$$\begin{aligned} J_{QQ}^{(4)} &= -\left(\frac{t_{CQ}\left(\frac{t_{CQ}{t_{QQ}}^2}{(\Omega - U_Q + 2V_{CQ} - V_{QQ})(\Omega - U_Q + V_{QQ})} - \frac{{t_{CQ}}^3}{(\Omega - U_C + V_{QQ})(\Omega - U_Q + V_{QQ})}\right)}{\Omega - U_Q + 2V_{CQ} - V_{QQ}}\right) \\ &\quad - \frac{t_{CQ}\left(-\left(\frac{{t_{CQ}}^3}{(\Omega - U_Q + 2V_{CQ} - V_{QQ})(\Omega - U_Q + V_{QQ})}\right) + \frac{t_{CQ}{t_{QQ}}^2}{(\Omega - U_C + V_{QQ})(\Omega - U_Q + V_{QQ})}\right)}{\Omega - U_C + V_{QQ}} \\ &\quad + \frac{t_{QQ}\left(-\left(\frac{{t_{CQ}}^2 t_{QQ}}{(\Omega - U_C + V_{QQ})(\Omega - U_Q + V_{QQ})}\right) + \frac{t_{CQ}\left(-\left(\frac{t_{CQ}t_{QQ}}{\Omega - U_Q + 2V_{CQ} - V_{QQ}}\right) - \frac{t_{CQ}t_{QQ}}{\Omega - U_Q + V_{QQ}}\right)}{\Omega - U_Q + 2V_{CQ} - V_{QQ}}\right)}{\Omega - U_Q + V_{QQ}} \end{aligned} \tag{4.106}$$

$$+\frac{t_{QQ}\left(-\left(\frac{{t_{CQ}}^2 t_{QQ}}{(\Omega-U_Q+2V_{CQ}-V_{QQ})(\Omega-U_Q+V_{QQ})}\right)-\frac{t_{CQ}\left(\frac{t_{CQ}t_{QQ}}{\Omega-U_C+V_{QQ}}+\frac{t_{CQ}t_{QQ}}{\Omega-U_Q+V_{QQ}}\right)}{\Omega-U_C+V_{QQ}}\right)}{\Omega-U_Q+V_{QQ}}$$

$$J_{CQ}^{(4)} = \frac{t_{CQ}\left(\frac{t_{CQ}{t_{QQ}}^2}{(\Omega-U_Q+2V_{CQ}-V_{QQ})(\Omega-U_Q+V_{QQ})}-\frac{{t_{CQ}}^3}{(\Omega-U_C+V_{QQ})(\Omega-U_Q+V_{QQ})}\right)}{\Omega-U_Q+2V_{CQ}-V_{QQ}} \tag{4.107}$$

$$+\frac{t_{CQ}\left(-\left(\frac{{t_{CQ}}^3}{(\Omega-U_Q+2V_{CQ}-V_{QQ})(\Omega-U_Q+V_{QQ})}\right)+\frac{t_{CQ}{t_{QQ}}^2}{(\Omega-U_C+V_{QQ})(\Omega-U_Q+V_{QQ})}\right)}{\Omega-U_C+V_{QQ}}$$

$$-\frac{t_{CQ}\left(\frac{{t_{CQ}}^3}{(\Omega-U_Q+2V_{CQ}-V_{QQ})(\Omega-U_Q+V_{QQ})}-\frac{t_{QQ}\left(-\left(\frac{t_{CQ}t_{QQ}}{\Omega-U_Q+2V_{CQ}-V_{QQ}}\right)-\frac{t_{CQ}t_{QQ}}{\Omega-U_Q+V_{QQ}}\right)}{\Omega-U_Q+2V_{CQ}-V_{QQ}}\right)}{\Omega-U_Q+2V_{CQ}-V_{QQ}} -$$

$$\frac{t_{CQ}\left(\frac{{t_{CQ}}^3}{(\Omega-U_C+V_{QQ})(\Omega-U_Q+V_{QQ})}+\frac{t_{QQ}\left(\frac{t_{CQ}t_{QQ}}{\Omega-U_C+V_{QQ}}+\frac{t_{CQ}t_{QQ}}{\Omega-U_Q+V_{QQ}}\right)}{\Omega-U_C+V_{QQ}}\right)}{\Omega-U_C+V_{QQ}}$$

$$J_{QQ} \simeq J_{QQ}^{(2)} + J_{QQ}^{(3)} + J_{QQ}^{(4)} \tag{4.108}$$

$$J_{CQ} \simeq J_{CQ}^{(2)} + J_{CQ}^{(3)} + J_{CQ}^{(4)}. \tag{4.109}$$

Because $J_{QQ}^{(i)}, J_{CQ}^{(i)} (i = 2, 3, 4)$ are functions of $V_{QQ}, V_{CQ}, U_Q, U_C, t_{QQ}$, and t_{CQ}, we can use reasonable values for those variables to perform numerical calculations and then compare these results with our variational calculation (see Chapter 3). In general, there is quantitative relationship between those parameters in the expression of exchange interaction J_{QQ}, J_{CQ}. The magnitude of t_{QQ} should be very small, but the magnitude of t_{CQ} may be large and we can roughly assume it to decay exponentially with the height of the control atom. $V_{QQ} < V_{CQ} < U_Q < U_C$ because on-site Coulomb interaction should be larger than the Coulomb interaction between different centres. U_Q should be larger than U_C because the qubit spatial state is more localized than the control state. For the same reason V_{QQ} should be smaller than V_{CQ}. Similarly we can assume V_{CQ} decay exponentially. For definiteness we assume the following values for the parameters: $U_C = 1.0, U_Q = 1.5, V_{QQ} = 0.5, V_{CQ} = e^{-d/2}, t_{QQ} = -0.01, t_{CQ} = -e^{-d/2}$. Using these parameters, we calculate J_{CQ}, J_{QQ} shown in Figure 4.6 and Figure 4.7. Here H is the height of control atom.

4.7 Conclusion and discussion

In Figure (4.7) with these parameters a negative (ferromagnetic) part in the qubit-qubit exchange coupling J_{QQ} does indeed arise at intermediate qubit-control sep-

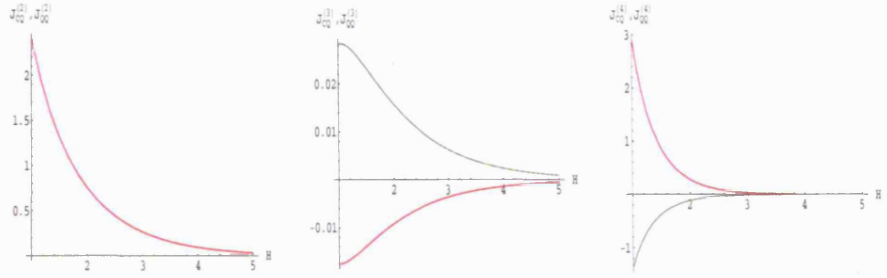

(a) (b) (c)

Fig. 4.6: (a)Second order exchange interactions as a function of d. Red line: $J_{CQ}^{(2)}$; green line: $J_{QQ}^{(2)}$, as calculated by perturbation theory through second order using the parameters given in the text. d is the height of the control atom.(b)Third order exchange interactions as a function of d. Red line: $J_{CQ}^{(3)}$; green line: $J_{QQ}^{(3)}$, as calculated by perturbation theory through third order. (c)Fourth order exchange interaction as a function of d. Red line: $J_{CQ}^{(4)}$; green line: $J_{QQ}^{(4)}$, as calculated by perturbation theory through fourth order.

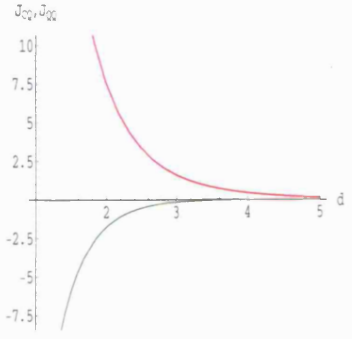

Fig. 4.7: Perturbation theory calculations of exchange interaction as functions of d. Red line: J_{CQ}; green line: J_{QQ}, as calculated by perturbation theory.

arations. We can also see that the main negative contribution comes from the fourth-order perturbation expansion, because the second-order terms are small (t_{QQ} is very small), and the third-order terms also involve t_{QQ}. So the fourth-order terms involving relatively large t_{CQ} become dominant. But using such simple perturbation theory, we have not been able to obtain quantitative agreement with the variational calculations. The reasons for this include

- First of all, this is a perturbation theory calculation. So part of the inaccuracy comes from the ignorance of the higher-order perturbation expansion.
- For simplification, we exclude the excited qubit states.
- In the perturbation theory calculation, we assume those possible states we need consider are orthogonal. This is not true in practice.
- We neglect the overlaps between wave functions, but these overlaps are very important in the explicit variational calculation.
- Many two-particle integrals are ignored in the perturbation theory calculation because we assume they are small. In fact there are many more two-particle integrals involved in the variational calculation than this perturbation calculation, e.g., $\int d[1]d[2]\phi_C(1)\phi_C(1)\lambda_A(2)\lambda_B(2)$.

So in summary, the perturbation theory calculation only can give us a qualitative check of our relatively explicit variational calculation.

5. RANDOM DISTRIBUTION OF DONORS IN SILICON

5.1 Introduction

If we can randomly put donors in silicon, the donor distribution will determine the average distance between nearest-neighbour donors and therefore the distribution of the interactions between them. In the control-qubit scheme the 1st nearest neighbours are used to do quantum computation, but the 2nd nearest neighbour is the strongest perturbation to the control-qubit system. So it is important to know how the 2nd nearest neighbours are distributed randomly. The simplest model in which to examine the distribution of 1st and 2nd nearest neighbours is a continuous one in which we forget about the existence of the crystal lattice and simply assume that the atoms are distributed randomly and independently in three-dimensional space. In this chapter we first consider the distribution of the first nearest neighbours. Then we perform a similar calculation for the distribution of the second nearest neighbours. At the end, we compare two kinds of interactions: exchange interaction and dipole-dipole interaction, and see which one dominates the interaction from the 2nd nearest neighbours.

5.2 The distribution of 1st nearest neighbours

This distribution of 1st nearest neighbors was first considered by Hertz [46, 47]. Let $w(r)dr$ denote the probability that the nearest neighbor to a particle occurs between r and $r+dr$. The function $w(r)$ must satisfy the relation

$$w(r) = [1 - \int_0^r w(x)dx]4\pi r^2 n, \tag{5.1}$$

where n denotes the average number of particles per unit volume. Then we have

$$\frac{d}{dr}[\frac{w(r)}{4\pi r^2 n}] = -4\pi r^2 n \frac{w(r)}{4\pi r^2 n} \tag{5.2}$$

$$w(r) = e^{-4\pi r^3 n/3} 4\pi r^2 n. \tag{5.3}$$

using the above formulae we can derive an exact formula for the 'average distance' D between a particle we are interested in and its first nearest neighbors.

$$D = \int_0^\infty r w(r)dr \tag{5.4}$$

$$= \Gamma(\frac{4}{3})(4\pi n/3)^{\frac{1}{2}}, \tag{5.5}$$

where $\Gamma(x)$ is the Euler gamma function:

$$\Gamma(x) = \int_0^\infty t^{x-1}e^{-t}dt. \tag{5.6}$$

Andres *et al.*, calculated the distribution of exchange couplings from the 1st nearest neighbor [39]. The distribution of exchange couplings J from the 1st nearest neighbor takes the form

$$p_1(J) = |\frac{w(r)}{dJ/dr}|_{J=J(r)}, \tag{5.7}$$

if we know the analytical expression of exchange couplings and J is a monotonic function of inter-nuclei distance. We can also calculate the average value of exchange coupling from the 1st nearest neighbor by

$$\overline{J_1} = \int_0^\infty Jp_1(J)dJ \tag{5.8}$$

5.3 The distribution of 2nd nearest neighbours

Similarly, we can calculate the distribution of 2nd nearest neighbours given that a 1st nearest neighbor occurs at the distance R. The probability that a 2nd nearest neighbor occurs between r and $r + dr$ given the distance of the 1st nearest neighbor being R is

$$w_2(r|R) = [1 - \int_R^r w_2(x|R)dx]4\pi r^2 n \ (r \geq R), \tag{5.9}$$

and $w_2(r|R)$ should vanish when $r < R$. And we also require that

$$w_2(r) = 4\pi R^2 n, \tag{5.10}$$

when $r \rightarrow R^+$ due to the normalization condition

$$\int_R^\infty w_2(r|R)dr = 1. \tag{5.11}$$

Hence, we can find this conditional probability reads

$$w_2(r|R) = 4\pi r^2 n e^{-\frac{4\pi n}{3}(r^3 - R^3)} \ (r > R). \tag{5.12}$$

Actually, we can generalize this calculation to the case: if we know the nth nearest neighbor is at the distance R, the probability that the $(n+1)$th nearest neighbor occurs between r and $r + dr$ takes the form (5.12). We also can calculate the

average distance of the conditional 2nd nearest neighbor (i.e., the mean distance to the second nearest neighbor given that the first nearest neighbor is at distance R).

$$D_2(R) = \int_R^\infty r w_2(r) \tag{5.13}$$

$$= (\frac{3}{4\pi n})^{1/3} e^X \int_X^\infty x^{1/3} e^{-x} dx, \tag{5.14}$$

where

$$X = \frac{4\pi}{3} n R^3. \tag{5.15}$$

From the definition of incomplete gamma functions:

$$\Gamma(a,x) = \Gamma(a) - \gamma(a,x) \tag{5.16}$$

$$\Gamma(a) = \int_0^\infty t^{a-1} e^{-t} dt \tag{5.17}$$

$$\gamma(a,x) = \int_0^x t^{a-1} e^{-t} dt \tag{5.18}$$

$$\Gamma(a,x) = \int_x^\infty t^{a-1} e^{-t} dt, \tag{5.19}$$

therefore

$$D_2(R) = (\frac{3}{4\pi n})^{1/3} e^X \Gamma(\frac{4}{3}, X). \tag{5.20}$$

Also, provided the exchange coupling J is a monotonic function of the inter-nuclei distance we can calculate the distribution of 2nd nearest neighbor exchange coupling conditional on a 1st nearest neighbor separation R from

$$p_2(J,R) = |\frac{w_2(r|R)}{dJ/dr}|_{J=J(r)}, \tag{5.21}$$

and the corresponding average value of exchange coupling is $\overline{J_2}(R) = \int_0^\infty J p_2(J,R) dJ$.

In the figure below we first compare $\overline{J_2}(R)$ and $J(R)$ using the Herring-Flicker asymptotic form of exchange interaction which in atomic units is

$$J(R) = E_{triplet} - E_{singlet} \tag{5.22}$$

$$= 1.642 R^{5/2} e^{-2R} + O(R^2 e^{-2R}), \tag{5.23}$$

where R is the distance between two atoms. We use the donor density that Andres *et al.* used in [39] $n_D = 0.0032/a^{*3}, a^{*3} \sim a^2 b$, and $a = 25 \times 10^{-10}$ m and $b = 14 \times 10^{-10}$ m are Kohn-Luttinger radii as cited in chapter 2. So $n_D \simeq 3.6 \times 10^{17}/cm^3$.

Note that the effect of the exchange coupling from the 2nd nearest neighbor increases as R becomes larger as shown in Figure 5.1, 5.2, and 5.3. Another manifestation of the same physics is that $D_2(R) \to R$ as $R \to \infty$: if by some chance we have to go a very long way from our chosen initial dopant before we find its first nearest neighbor, we are very likely to find the second neighbor almost immediately.

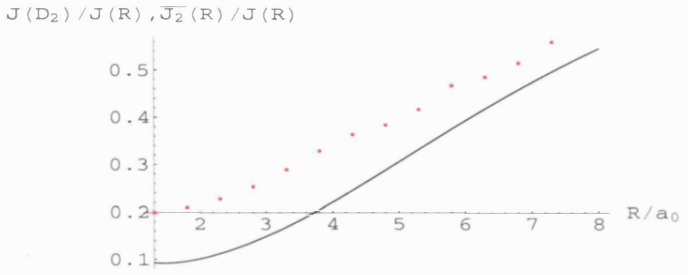

Fig. 5.1: The ratio of $\overline{J_2}(R)$ to $J(R)$(red points) and the ratio of $J(D_2(R))$ to $J(R)$ (black curve) as functions of the distance of the 1st nearest neighbors R. Donor density is $n_D = 0.0032/a^{*3} = 3.6 \times 10^{17}/cm^3$. Notice that the effect of exchange coupling from the 2nd nearest neighbor becomes larger when the distance of the 1st nearest neighbor is enlarged.

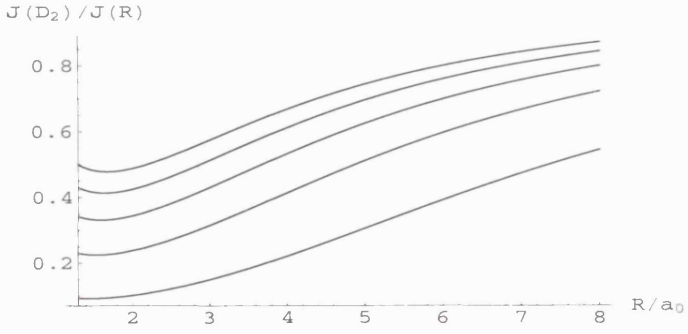

Fig. 5.2: The ratio of $J(D_2(R))$ to $J(R)$ as a function of the distance of 1st nearest neighbors R. The curves from down to up are associated with increasing donor densities which are $n_D = 0.0032/a^{*3} = 3.6 \times 10^{17}/cm^3, n_D = 0.0062/a^{*3} = 7.09 \times 10^{17}/cm^3, n_D = 0.0092/a^{*3} = 1.05 \times 10^{18}/cm^3, n_D = 0.0122/a^{*3} = 1.39 \times 10^{18}/cm^3, n_D = 0.0152/a^{*3} = 1.73 \times 10^{18}/cm^3$. Notice that the effect of exchange coupling from the 2nd nearest neighbor becomes larger as the distance of the 1st nearest neighbor is enlarged and the donor density increases.

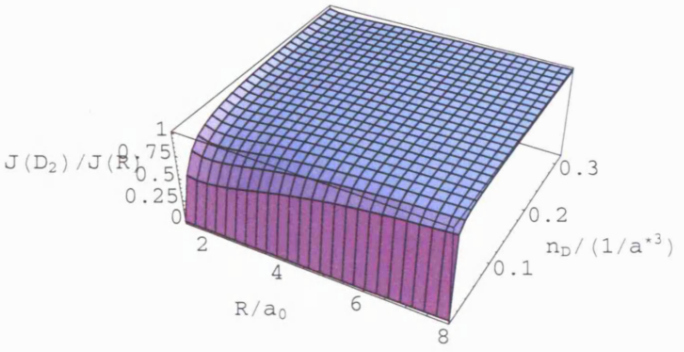

Fig. 5.3: The ratio of $J(D_2(R))$ to $J(R)$ as a function of the distance of 1st nearest neighbors R and the donor density n_D which ranges from $n_D = 0.00032/a^{*3} = 3.6 \times 10^{16}/cm^3$ to $n_D = 0.32/a^{*3} = 3.6 \times 10^{19}/cm^3$. Notice that the higher the donor density, the easier to find out the 2nd nearest neighbors in a fixed 1st nearest neighbor distance R.

5.4 Competition between dipole-dipole and exchange interactions

The dipole-dipole interaction is very important and responsible for the line shape broadening. So it is necessary to consider it and compare it with exchange interaction. The dipole-dipole interaction reads

$$H_{DD}(\vec{R}) = J_{DD}(\vec{R})(\vec{S_1} \cdot \vec{S_2}) - 3g^2\beta^2 R^{-5}(\vec{R} \cdot \vec{S_j})(\vec{R} \cdot \vec{S_k}), \tag{5.24}$$

where β denotes the Bohr magneton, nuclear or electric as the case may be, and g is the corresponding Lande factor which is 2 for electrons. If we ignore the terms depending on the relative orientations of two atoms,

$$H_{DD}(\vec{R}) = J_{DD}(\vec{R})(\vec{S_1} \cdot \vec{S_2}) \tag{5.25}$$

$$J_{DD}(\vec{R}) = g^2\beta^2 R^{-3} \tag{5.26}$$

$$= 0.000074 \times R^{-3}. \tag{5.27}$$

Here the energy unit is Hartree. We can compare the dipole-dipole interaction with the Herring-Flicker asymptotic form of exchange interaction in Figure 5.4. We can see that when the inter-nuclei distance is larger that $14a_0$, the dipole-dipole interaction becomes dominant. We can do the same calculation to compare the

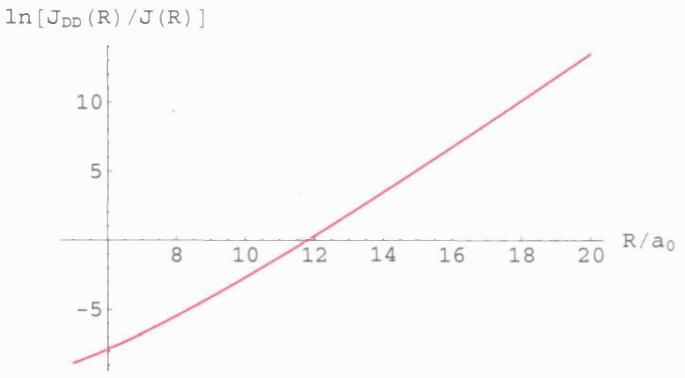

Fig. 5.4: The ratio of $J_{DD}(R)$ to the Herring-Flicker asymptotic form $J(R)$ as a function of the inter-nuclei distance R. Notice that when $R < 10a_0$ the exchange interaction is dominant, but when $R > 14a_0$, the dipole interaction becomes dominant.

dipole-dipole interaction from the 2nd nearest neighbor by $J_{DD}(D_2(R))$ with that from the 1st nearest neighbor $J_{DD}(R)$ in Figure 5.5. We can do another calculation to compare the dipole-dipole interaction from the 2nd nearest neighbor by $\overline{J_{DD2}}(R) = \int_0^\infty J p_2^{DD}(J) dJ$ with that from the 1st nearest neighbor $J_{DD}(R)$ in Figure 5.6. We can see the same behavior as the exchange interaction in the last section. We also can compare the dipole-dipole interaction from the 2nd nearest neighbor by $J_{DD}(D_2(R))$ with the exchange interaction from the 2nd nearest neighbor $J(D_2(R))$. We can see that the larger the distance at which the 1st nearest neighbor occurs is, the more dominant the dipole-dipole interaction from the 2nd nearest neighbor is. And as the donor density becomes more dilute, it is more difficult to find the 2nd nearest neighbor, so we have to go a long way to find it (See Figure 5.7). In another way, we can compare $\overline{J_{DD2}}(R)$ with $\overline{J_2}(R)$ (See Figure 5.8).

5.5 Conclusion

We have computed the exchange couplings expected from the second-nearest neighbour of a given spin, as a function of the distance to the first nearest neighbour. We find that the ratio of the second-neighbour to first-neighbour exchanges depends strongly on the distance to the first neighbour; if the first-neighbour distance is large compared with the mean inter-defect separation, it is is very likely that we will find a second neighbour at an only slightly greater distance, and hence the exchange interactions will be comparable. This points to the importance of selecting strongly coupled pairs, if the influence of other spins is not to be too strong. We

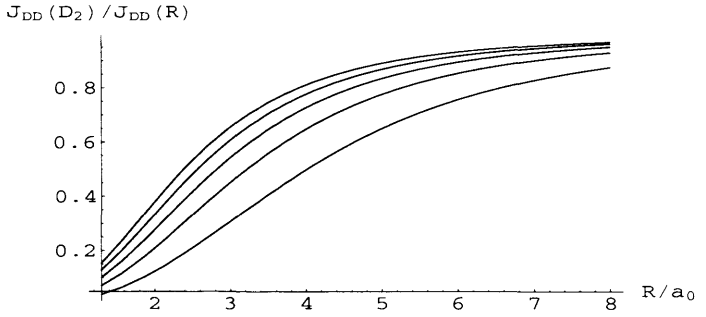

Fig. 5.5: The ratio of $J_{DD}(D_2(R))$ to $J_{DD}(R)$ as a function of the distance of 1st nearest neighbors R. The curves from down to up are associated with increasing donor densities which are $n_D = 0.0032/a^{*3} = 3.6 \times 10^{17}/cm^3, n_D = 0.0062/a^{*3} = 7.09 \times 10^{17}/cm^3, n_D = 0.0092/a^{*3} = 1.05 \times 10^{18}/cm^3, n_D = 0.0122/a^{*3} = 1.39 \times 10^{18}/cm^3, n_D = 0.0152/a^{*3} = 1.73 \times 10^{18}/cm^3$. Notice that the effect of dipole-dipole interaction from the 2nd nearest neighbor becomes larger as the distance of the 1st nearest neighbor is enlarged and the donor density increases.

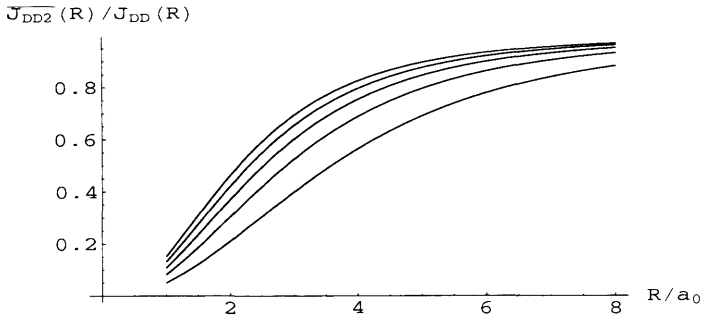

Fig. 5.6: The ratio of $\overline{J_{DD2}}(R)$ to $J_{DD}(R)$ as a function of the distance of 1st nearest neighbors R. The curves from down to up are associated with increasing donor densities which are $n_D = 0.0032/a^{*3} = 3.6 \times 10^{17}/cm^3, n_D = 0.0062/a^{*3} = 7.09 \times 10^{17}/cm^3, n_D = 0.0092/a^{*3} = 1.05 \times 10^{18}/cm^3, n_D = 0.0122/a^{*3} = 1.39 \times 10^{18}/cm^3, n_D = 0.0152/a^{*3} = 1.73 \times 10^{18}/cm^3$. Notice that the effect of dipole-dipole interaction from the 2nd nearest neighbor becomes bigger when the distance of the 1st nearest neighbor is enlarged and the donor density increases.

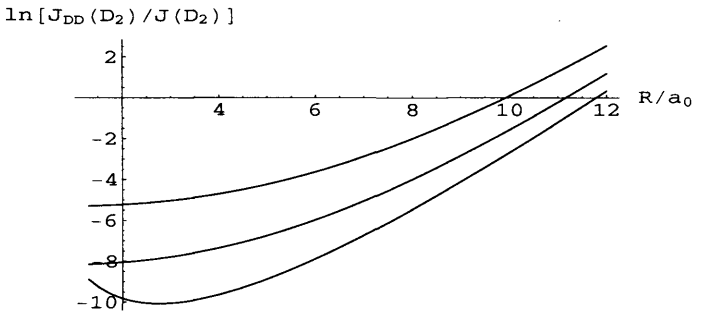

Fig. 5.7: The ratio of $J_{DD}(D_2(R))$ to $J(D_2(R))$ as a function of the distance of 1st nearest neighbors R. The curves from up to down are associated with increasing donor densities which are $n_D = 0.00032/a^{*3} = 3.6 \times 10^{16}/cm^3, n_D = 0.0092/a^{*3} = 1.09 \times 10^{18}/cm^3, n_D = 3.2/a^{*3} = 3.6 \times 10^{20}/cm^3$. Notice that (a) the effect of dipole-dipole interaction from the 2nd nearest neighbor is bigger and bigger when the distance of the 1st nearest neighbor is enlarged and (b) as the donor density becomes more dilute, the dipole-dipole interaction becomes dominant at the shorter distance of the 1st nearest neighbor.

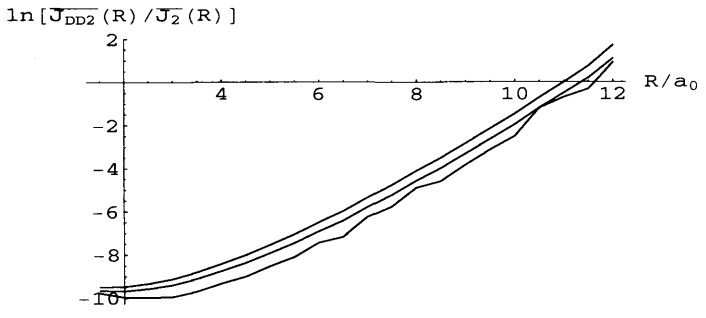

Fig. 5.8: The ratio of $\overline{J_{DD2}}(R)$ to $\overline{J_2}(R)$ as a function of the distance of 1st nearest neighbors R. The curves from up to down are associated with increasing donor densities which are $n_D = 0.00032/a^{*3} = 3.6 \times 10^{16}/cm^3, n_D = 0.00092/a^{*3} = 1.09 \times 10^{17}/cm^3, n_D = 0.016/a^{*3} = 1.8 \times 10^{18}/cm^3$. Notice the same behavior as in Figure 5.7.

have also compared the exchange interaction with the dipole-dipole interaction associated with the 1st nearest neighbor and the 2nd nearest neighbor respectively. Within our simple continuum model, and for the defect densities likely to be of interest for quantum information processing (where the nearest neighbour is likely to be found within a distance of order $10a_0$), the dipole-dipole interaction from the nearest neighbor can generally be neglected, but it should be considered for more distant spins and will be dominant at relatively long distances (above about $14a_0$).

6. SPIN DYNAMICS IN A SMALL GROUP OF SPINS

6.1 Introduction

If we use three first nearest neighbours as two qubits and one control (control-qubit system) [23] to do quantum computation and readout in a silicon material in which donors are randomly distributed, the second nearest neighbour will be the strongest perturbation and the exchange coupling from 2nd nearest neighbour may be comparable to that from 1st nearest neighbour as shown in the last chapter. Therefore, it is necessary to know the effect the second nearest neighbours have on the evolution of spin states in the control-qubit system. In this chapter we focus on the spin dynamics in a small spin group which includes several qubit spins and one control spin:

- A qubit to be measured

  What we really care about is the spin dynamics of the qubit to be measured.

- An auxiliary qubit

  The auxiliary qubit is the first nearest neighbour of the qubit to be measured. We can use this qubit to help us do quantum computation and readout.

- A control atom.

  The control atom is the first nearest neighbour of the qubit to be measured. The control atom is very important in our quantum computing scheme. In the quantum computation the control atom is excited by laser to produce entangling gates to evolve qubit spin states. In the readout process it is excited by laser to scatter photons. In the next chapter we will introduce the readout scheme.

- A spectator spin

  The spectator spin is the second nearest neighbour which is the strongest perturbation to the control-qubit system. From the last chapter, we can see that if 1st nearest neighbour is quite a long way from our initial chosen donor, then we are quite likely to find the 2nd nearest neighbour almost immediately.

Putting it into another way, the interaction from the spectator spin may be comparable to the interaction from 1st nearest neighbours. So the 2nd nearest neighbour is quite important for our control-qubit system if the sample is sufficiently dilute.

This small spin group is the simplest case we can consider because we have only one spectator spin. Although this is very simple model, we can see how the spectator spin influences the time evolution of the qubit spin even if we have only one spectator spin, and the usefulness of the magnetic field by analysis of the reduced density matrix.

6.2 Time-evolution of 3-spin states

6.2.1 Description of system

In this section we consider three spins: a control atom, a qubit to be measured, and a spectator spin. In our control-qubit system the control atom is assumed to be the first nearest neighbour of the qubit to be measured, so it is strongly coupled with the qubit to be measured. We neglect the exchange interactions between the control electron spin and the spectator spin which is the second nearest neighbour of the qubit to be measured, and the exchange interactions between any other spins and these three spins. For the moment we also ignore the auxiliary spin. We shall see similar physical phenomena when we consider the auxiliary spin as shown in section 6.4.

Therefore, if we consider the external magnetic fields the spin Hamiltonian of these three spins including a control spin $\vec{S}_0$, a qubit to be measured $\vec{S}_1$, and a spectator spin $\vec{S}_2$ reads

$$\hat{H} = J_1\vec{S}_0 \cdot \vec{S}_1 + J_2\vec{S}_1 \cdot \vec{S}_2 + B_z\mu_B \sum_{i=0}^{2} g_i S_{zi}, \tag{6.1}$$

where B_z is the z-component of magnetic field, μ_B is Bohr magneton, and g_i is g-factor of each spin. Additionally, we assume in our sample $J_1 >> J_2$. First we consider the situation where there is no external magnetic field, i.e., $B_z = 0$. Then we also assume that at $t = 0$ we know the spin state of the control electron, say $|\uparrow\rangle$(In fact, if we selected $|\downarrow\rangle$, we should get the same result), and the spin state of the qubit to be measured is $\alpha|\uparrow\rangle + \beta|\downarrow\rangle$. We do not know the spin state of the spectator spin at all, so its spin state density matrix is assumed to be a classical mixture, say, $\frac{1}{2}|\uparrow\rangle\langle\uparrow| + \frac{1}{2}|\downarrow\rangle\langle\downarrow|$. So we can calculate the density matrix for these three spins in two steps:

1. Start from the pure state in which the spectator spin is in $|\uparrow\rangle$ state,

$$|\psi_\uparrow(t=0)\rangle = \alpha|\uparrow\uparrow\uparrow\rangle + \beta|\uparrow\downarrow\uparrow\rangle \tag{6.2}$$

and evolve it in time to calculate $\rho_\uparrow(t) = |\psi_\uparrow(t)\rangle\langle\psi_\uparrow(t)|$. Noticing that $|\uparrow\uparrow\downarrow\rangle$, $|\uparrow\downarrow\uparrow\rangle$, and $|\downarrow\uparrow\uparrow\rangle$ are coupled, we find the matrix of Hamiltonian spanned by them:($\hbar = 1$)

$$H_\uparrow = \begin{array}{c} \\ |\uparrow\uparrow\uparrow\rangle \\ |\uparrow\uparrow\downarrow\rangle \\ |\uparrow\downarrow\uparrow\rangle \\ |\downarrow\uparrow\uparrow\rangle \end{array} \begin{array}{c} \begin{array}{cccc} |\uparrow\uparrow\uparrow\rangle & |\uparrow\uparrow\downarrow\rangle & |\uparrow\downarrow\uparrow\rangle & |\downarrow\uparrow\uparrow\rangle \end{array} \\ \begin{pmatrix} \frac{J_1+J_2}{4} & 0 & 0 & 0 \\ 0 & \frac{J_1-J_2}{4} & \frac{J_2}{2} & 0 \\ 0 & \frac{J_2}{2} & -\frac{J_1+J_2}{4} & \frac{J_1}{2} \\ 0 & 0 & \frac{J_1}{2} & -\frac{J_1-J_2}{4} \end{pmatrix} \end{array}. \tag{6.3}$$

The other four states $|\downarrow\downarrow\downarrow\rangle, |\downarrow\downarrow\uparrow\rangle, |\downarrow\uparrow\downarrow\rangle, |\uparrow\downarrow\downarrow\rangle$ are not coupled with the above four states because $[\hat{H}, \hat{S}_{0z} + \hat{S}_{1z} + \hat{S}_{2z}] = 0$.

2. For the pure state in which the spectator spin is in $|\downarrow\rangle$ state,

$$|\psi_\downarrow(t=0)\rangle = \alpha|\uparrow\uparrow\downarrow\rangle + \beta|\uparrow\downarrow\downarrow\rangle \tag{6.4}$$

and evolve it to calculate $\rho_\downarrow(t) = |\psi_\downarrow(t)\rangle\langle\psi_\downarrow(t)|$.

Similarly, $|\uparrow\downarrow\downarrow\rangle$, $|\downarrow\uparrow\downarrow\rangle$, and $|\downarrow\downarrow\uparrow\rangle$ are coupled. We can get the Hamiltonian matrix:

$$H_\downarrow = \begin{pmatrix} H_1 & 0 \\ 0 & H_2 \end{pmatrix} \tag{6.5}$$

$$H_1 = \begin{array}{c} \\ |\uparrow\uparrow\downarrow\rangle \\ |\uparrow\downarrow\uparrow\rangle \\ |\downarrow\uparrow\uparrow\rangle \end{array} \begin{array}{c} \begin{array}{ccc} |\uparrow\uparrow\downarrow\rangle & |\uparrow\downarrow\uparrow\rangle & |\downarrow\uparrow\uparrow\rangle \end{array} \\ \begin{pmatrix} \frac{J_1-J_2}{4} & \frac{J_2}{2} & 0 \\ \frac{J_2}{2} & -\frac{J_1+J_2}{4} & \frac{J_1}{2} \\ 0 & \frac{J_1}{2} & -\frac{J_1-J_2}{4} \end{pmatrix} \end{array} \tag{6.6}$$

$$H_2 = \begin{array}{c} \\ |\uparrow\downarrow\downarrow\rangle \\ |\downarrow\uparrow\downarrow\rangle \\ |\downarrow\downarrow\uparrow\rangle \end{array} \begin{array}{c} \begin{array}{ccc} |\uparrow\downarrow\downarrow\rangle & |\downarrow\uparrow\downarrow\rangle & |\downarrow\downarrow\uparrow\rangle \end{array} \\ \begin{pmatrix} \frac{J_2-J_1}{4} & \frac{J_1}{2} & 0 \\ \frac{J_1}{2} & -\frac{J_1+J_2}{4} & \frac{J_2}{2} \\ 0 & \frac{J_2}{2} & \frac{J_1-J_2}{4} \end{pmatrix} \end{array}. \tag{6.7}$$

To calculate $\psi_{\uparrow,\downarrow}(t)$, we can use

$$\begin{aligned} \psi(t) &= e^{-i\hat{H}t}\psi(0) \\ e^{-i\hat{H}t} &= \sum_n e^{-iE_n t}|n\rangle\langle n|, \end{aligned} \tag{6.8}$$

where $|n\rangle$ is the eigenstate of $\hat{H}$ associated with the eigenvalue E_n.

Because the spectator spin is assumed to be the classical mixture, we can calculate the total density of these spins by:

$$\rho(t) = \frac{1}{2}(\rho_\uparrow + \rho_\downarrow) \tag{6.9}$$

Finally, we can get the reduced density matrix for the qubit to be measured $\vec{S}_1$:

$$\tilde{\rho}(t) = \mathrm{Tr}_{\text{other spins}}[\rho(t)], \tag{6.10}$$

where $\tilde{\rho}$ is the reduced density matrix for the spin to be measured. We are concerned with two components in $\tilde{\rho}$: the population of up spin $\tilde{\rho}_{\uparrow\uparrow}$ and the population of down spin $\tilde{\rho}_{\downarrow\downarrow}$.

6.2.2 Numerical results

It is sufficient to know the ratio of J_1 to J_2 in order to make the key point clear, so we can select some parameters for J_1 and J_2 with $J_1 >> J_2$. We may select the parameters: $\alpha = \frac{\sqrt{2}}{\sqrt{3}}$, and $\beta = \frac{1}{\sqrt{3}}$, and $J_1 = 0.1$, or $0.5; J_2 = 0.01$. The spin up and down populations as functions of time are shown in Figure 6.1.

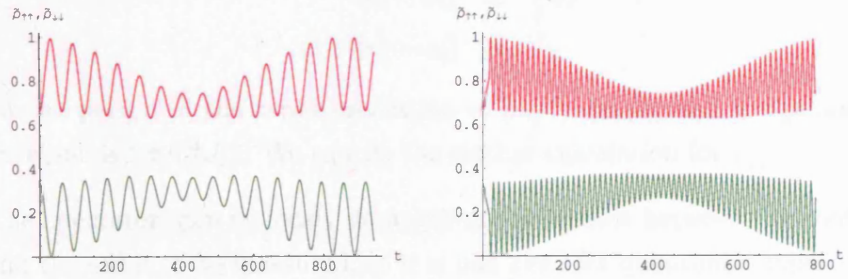

(a) (b)

Fig. 6.1: The spin-up and spin-down populations of the reduced density matrix for the qubit to be measured as functions of time. Red curve: $\tilde{\rho}_{\uparrow\uparrow}$; green curve: $\tilde{\rho}_{\downarrow\downarrow}$. (a)Select parameters: $\alpha = \frac{\sqrt{2}}{\sqrt{3}}$, and $\beta = \frac{1}{\sqrt{3}}$, and $J_1 = 0.1, J_2 = 0.01$. Notice that the period of the rapid oscillation $\sim 2\pi/J_1$, and the period of the envelope $\sim 2\pi/(\frac{3}{4}J_2)$. (b) The same parameters as (a) except $J_1 = 0.5$. Notice that the period of the rapid oscillation $\sim 2\pi/J_1$, and the period of the envelope $\sim 2\pi/(\frac{3}{4}J_2)$.

6.2.3 Discussion

From Figure 6.1, we can see that

- The period of the rapid oscillation of the spin population $\simeq 2\pi/J_1$, and the period of the envelope $\simeq 2\pi/(\frac{3}{4}J_2)$. Actually, the oscillation periods depend on the splittings between eigenvalues of the spin coupling Hamiltonian as shown in equation 6.8. We can find the eigenvalues of the spin Hamiltonian. For example, for $\hat{H}_{\uparrow}$, we have its eigenvalues

$$e_1 = \frac{1}{4}(J_1 + J_2), \tag{6.11}$$

$$e_2 = \frac{1}{4}(J_1 + J_2), \tag{6.12}$$

$$e_3 = \frac{1}{4}(-J_1 - J_2 - 2\sqrt{J_1^2 - J_1J_2 + J_2^2}), \tag{6.13}$$

$$e_4 = \frac{1}{4}(-J_1 - J_2 + 2\sqrt{J_1^2 - J_1J_2 + J_2^2}). \tag{6.14}$$

Because $J_1 >> J_2$, we can approximate that

$$\sqrt{J_1^2 - J_1J_2 + J_2^2} = (J_1 - J_2/2)[1 + \frac{3J_2^2}{16(J_1 - J_2/2)^2}] \tag{6.15}$$

$$\simeq (J_1 - J_2/2). \tag{6.16}$$

Therefore

$$|e_1 - e_3| \simeq J_1 \tag{6.17}$$

$$|e_1 - e_4| \simeq \frac{3}{4}J_2 \tag{6.18}$$

$$|e_3 - e_4| \simeq J_1. \tag{6.19}$$

So the period of the rapid oscillation in $\rho_{\uparrow\uparrow}$ is $2\pi/J_1$, and the period of the envelope is $2\pi/(\frac{3}{4}J_2)$. We can do the similar calculation for $\rho_{\downarrow\downarrow}$.

- The spectator spin seriously damages the coherence between the control spin and the qubit to be measured, so it is bad news for quantum computation and the readout even if they are predominantly exchange coupled, i.e., contain no 'non-secular' terms, i.e., dipole-dipole interaction.

- The timescale for which the quantum information can be held is $2\pi/J_1$.

6.3 Time-evolution of 3-spin states holding magnetic field

6.3.1 Description of system

Similar with the above section, we can do the time-evolution of 3-spin states when we add a magnetic field, i.e., $B_z \neq 0$ into the Hamiltonian 6.1. Correspondingly,

$$H_{\uparrow} = \begin{array}{c} \\ |\uparrow\uparrow\uparrow\rangle \\ |\uparrow\uparrow\downarrow\rangle \\ |\uparrow\downarrow\uparrow\rangle \\ |\downarrow\uparrow\uparrow\rangle \end{array} \begin{array}{c} \begin{array}{cccc} |\uparrow\uparrow\uparrow\rangle & |\uparrow\uparrow\downarrow\rangle & |\uparrow\downarrow\uparrow\rangle & |\downarrow\uparrow\uparrow\rangle \end{array} \\ \begin{pmatrix} \frac{J_1+J_2}{4} + \frac{B_0+B_1+B_2}{2} & 0 & 0 & 0 \\ 0 & \frac{J_1-J_2}{4} + \frac{B_0+B_1-B_2}{2} & \frac{J_2}{2} & 0 \\ 0 & \frac{J_2}{2} & -\frac{J_1+J_2}{4} + \frac{B_0-B_1+B_2}{2} & \frac{J_1}{2} \\ 0 & 0 & \frac{J_1}{2} & -\frac{J_1-J_2}{4} + \frac{-B_0+B_1+B_2}{2} \end{pmatrix} \end{array} \tag{6.20}$$

$$H_{\downarrow} = \begin{pmatrix} H_1 & 0 \\ 0 & H_2 \end{pmatrix} \tag{6.21}$$

$$H_1 = \begin{array}{c} \\ |\uparrow\uparrow\downarrow\rangle \\ |\uparrow\downarrow\uparrow\rangle \\ |\downarrow\uparrow\uparrow\rangle \end{array} \begin{array}{c} \begin{array}{ccc} |\uparrow\uparrow\downarrow\rangle & |\uparrow\downarrow\uparrow\rangle & |\downarrow\uparrow\uparrow\rangle \end{array} \\ \begin{pmatrix} \frac{J_1-J_2}{4}+\frac{B_0+B_1-B_2}{2} & \frac{J_2}{2} & 0 \\ \frac{J_2}{2} & -\frac{J_1+J_2}{4}+\frac{B_0-B_1+B_2}{2} & \frac{J_1}{2} \\ 0 & \frac{J_1}{2} & -\frac{J_1-J_2}{4}+\frac{-B_0+B_1+B_2}{2} \end{pmatrix} \end{array} \tag{6.22}$$

$$H_2 = \begin{array}{c} \\ |\uparrow\downarrow\downarrow\rangle \\ |\downarrow\uparrow\downarrow\rangle \\ |\downarrow\downarrow\uparrow\rangle \end{array} \begin{array}{c} \begin{array}{ccc} |\uparrow\downarrow\downarrow\rangle & |\downarrow\uparrow\downarrow\rangle & |\downarrow\downarrow\uparrow\rangle \end{array} \\ \begin{pmatrix} \frac{J_2-J_1}{4}+\frac{B_0-B_1-B_2}{2} & \frac{J_1}{2} & 0 \\ \frac{J_1}{2} & -\frac{J_1+J_2}{4}+\frac{-B_0+B_1-B_2}{2} & \frac{J_2}{2} \\ 0 & \frac{J_2}{2} & \frac{J_1-J_2}{4}+\frac{-B_0-B_1+B_2}{2} \end{pmatrix} \end{array}, \tag{6.23}$$

where $B_i = \mu_B B_z g_i$.

6.3.2 Numerical results

By the same calculation methods, we can get the following numerical results as shown in Figure 6.2. The calculated result suggests that the magnetic field tries to

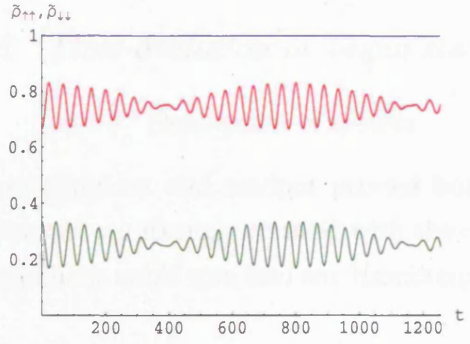

Fig. 6.2: The spin-up and spin-down populations of the reduce density matrix for the qubit to be measured as functions of time. $\alpha = \frac{\sqrt{2}}{\sqrt{3}}$, $\beta = \frac{1}{\sqrt{3}}$, and $J_1 = 0.1, J_2 = 0.01, B_0 = 0.1, B_1 = 0.2, B_2 = 0.2$. Red line is $\tilde{\rho}_{\uparrow\uparrow}$, and green line $\tilde{\rho}_{\downarrow\downarrow}$. Notice that the amplitude of the rapid oscillation is suppressed compared with Figure 6.1.

fix spin states. If the magnetic field is very large, the diagonal terms are dominant, it is difficult for the spin-flip operators to flip the spins. In other words, the evolution operator is approximately diagonal, so the spin states are unchanged from the original state except changing some states' phase factor.

We can consider this problem from another point of view. According to time-independent perturbation theory, the first-order approximate eigenstate reads

$$\psi_m = \psi_m^{(0)} + \sum_{n \neq m} [\frac{V_{nm}}{E_m^{(0)} - E_n^{(0)}} \psi_n^{(0)}]. \tag{6.24}$$

In our case, $|E_m^{(0)} - E_n^{(0)}| \propto B_i$ which is much bigger than the perturbation V_{nm}. So the mixture between the unperturbed states $\psi_n^{(0)}$ and $\psi_m^{(0)}$ becomes smaller when

B_i becomes bigger. Therefore the interference between states is smaller, and the oscillations between spin states is suppressed. For example, in $\hat{H}_\uparrow$,

$$\psi_1 = |\uparrow\uparrow\uparrow\rangle \tag{6.25}$$

$$\psi_2 = |\uparrow\uparrow\downarrow\rangle + \frac{J_2}{J_1}|\uparrow\downarrow\uparrow\rangle \tag{6.26}$$

$$\psi_3 = |\uparrow\downarrow\uparrow\rangle - \frac{J_2}{J_1}|\uparrow\uparrow\downarrow\rangle - \frac{J_1}{J_2+2B_1-2B_0}|\downarrow\uparrow\uparrow\rangle \tag{6.27}$$

$$\psi_4 = |\downarrow\uparrow\uparrow\rangle + \frac{J_1}{J_2+2B_1-2B_0}|\uparrow\downarrow\uparrow\rangle. \tag{6.28}$$

So we can see the magnetic field suppresses the oscillation amplitude due to the couplings between control and qubit to be measured because the g-factors are different for the control and qubits. Because the g-factors are the same for qubits the magnetic field can not suppress the oscillation amplitude due to the coupling between the spectator spin and qubits to be measured.

6.4 Time-evolution of 4-spin states

6.4.1 Description of system

During our quantum computation and readout process both the auxiliary qubits and the qubit to be measured are strongly coupled with the control electron. In this section we include the auxiliary qubit spin into our Hamiltonian(see Figure 6.3). We

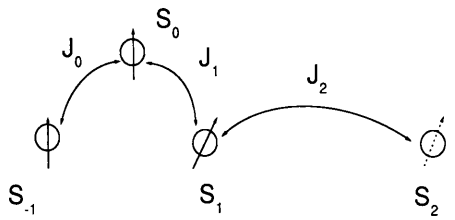

Fig. 6.3: $\vec{S}_{-1}$ is the auxiliary qubit, $\vec{S}_0$ is the control spin, $\vec{S}_1$ is the qubit to be measured, and $\vec{S}_2$ is the spectator spin. J_0, J_1, J_2 are the exchange couplings between them as shown in this figure.

can write down the Hamiltonian as

$$\hat{H} = J_0\vec{S_{-1}}\cdot\vec{S_0} + J_1\vec{S_0}\cdot\vec{S_1} + J_2\vec{S_1}\cdot\vec{S_2} + B_z\mu_B\sum_{i=-1}^{2} g_i S_{zi}, \tag{6.29}$$

where $\vec{S}_{-1}$ refers to the auxiliary qubit. We first consider the situation where there is no magnetic field, i.e., $B_z = 0$. This Hamiltonian includes four spins, so it should

be 16×16 matrix. The Hamiltonian reads:

$$H_{\uparrow} = \begin{array}{c} \\ |\uparrow\uparrow\uparrow\uparrow\rangle \\ |\uparrow\uparrow\uparrow\downarrow\rangle \\ |\uparrow\uparrow\downarrow\uparrow\rangle \\ |\uparrow\downarrow\uparrow\uparrow\rangle \\ |\downarrow\uparrow\uparrow\uparrow\rangle \end{array} \begin{array}{c} \begin{array}{ccccc} |\uparrow\uparrow\uparrow\uparrow\rangle & |\uparrow\uparrow\uparrow\downarrow\rangle & |\uparrow\uparrow\downarrow\uparrow\rangle & |\uparrow\downarrow\uparrow\uparrow\rangle & |\downarrow\uparrow\uparrow\uparrow\rangle \end{array} \\ \begin{pmatrix} \frac{J_0+J_1+J_2}{4} & 0 & 0 & 0 & 0 \\ 0 & \frac{J_0+J_1-J_2}{4} & \frac{J_2}{2} & 0 & 0 \\ 0 & \frac{J_2}{2} & \frac{J_0-J_1-J_2}{4} & \frac{J_1}{2} & 0 \\ 0 & 0 & \frac{J_1}{2} & \frac{-J_0-J_1+J_2}{4} & \frac{J_0}{2} \\ 0 & 0 & 0 & \frac{J_0}{2} & \frac{-J_0+J_1+J_2}{4} \end{pmatrix} \end{array}; \tag{6.30}$$

$$H_{\downarrow} = \begin{pmatrix} H_1 & 0 \\ 0 & H_2 \end{pmatrix} \tag{6.31}$$

$$H_1 = \begin{array}{c} \\ |\uparrow\uparrow\uparrow\downarrow\rangle \\ |\uparrow\uparrow\downarrow\uparrow\rangle \\ |\uparrow\downarrow\uparrow\uparrow\rangle \\ |\downarrow\uparrow\uparrow\uparrow\rangle \end{array} \begin{array}{c} \begin{array}{cccc} |\uparrow\uparrow\uparrow\downarrow\rangle & |\uparrow\uparrow\downarrow\uparrow\rangle & |\uparrow\downarrow\uparrow\uparrow\rangle & |\downarrow\uparrow\uparrow\uparrow\rangle \end{array} \\ \begin{pmatrix} \frac{J_0+J_1-J_2}{4} & \frac{J_2}{2} & 0 & 0 \\ \frac{J_2}{2} & \frac{J_0-J_1-J_2}{4} & \frac{J_1}{2} & 0 \\ 0 & \frac{J_1}{2} & \frac{-J_0-J_1+J_2}{4} & \frac{J_0}{2} \\ 0 & 0 & \frac{J_0}{2} & \frac{-J_0+J_1+J_2}{4} \end{pmatrix} \end{array} \tag{6.32}$$

$$H_2 = \begin{array}{c} \\ |\uparrow\uparrow\downarrow\downarrow\rangle \\ |\uparrow\downarrow\uparrow\downarrow\rangle \\ |\uparrow\downarrow\downarrow\uparrow\rangle \\ |\downarrow\uparrow\uparrow\downarrow\rangle \\ |\downarrow\uparrow\downarrow\uparrow\rangle \\ |\downarrow\downarrow\uparrow\uparrow\rangle \end{array} \begin{array}{c} \begin{array}{cccccc} |\uparrow\uparrow\downarrow\downarrow\rangle & |\uparrow\downarrow\uparrow\downarrow\rangle & |\uparrow\downarrow\downarrow\uparrow\rangle & |\downarrow\uparrow\uparrow\downarrow\rangle & |\downarrow\uparrow\downarrow\uparrow\rangle & |\downarrow\downarrow\uparrow\uparrow\rangle \end{array} \\ \begin{pmatrix} \frac{J_0-J_1+J_2}{4} & \frac{J_1}{2} & 0 & 0 & 0 & 0 \\ \frac{J_1}{2} & -\frac{J_0+J_1+J_2}{4} & \frac{J_2}{2} & \frac{J_0}{2} & 0 & 0 \\ 0 & \frac{J_2}{2} & \frac{-J_0+J_1-J_2}{4} & 0 & \frac{J_0}{2} & 0 \\ 0 & \frac{J_0}{2} & 0 & \frac{-J_0+J_1-J_2}{4} & \frac{J_2}{2} & 0 \\ 0 & 0 & \frac{J_0}{2} & \frac{J_2}{2} & \frac{-J_0-J_1-J_2}{4} & \frac{J_1}{2} \\ 0 & 0 & 0 & 0 & \frac{J_1}{2} & \frac{J_0-J_1+J_2}{4} \end{pmatrix} \end{array} \tag{6.33}$$

where the order is $|S_{-1}S_0S_1S_2\rangle$.

6.4.2 Numerical results

By the same calculation methods, we can obtain the following numerical results (Figure 6.4) which show the similar phenomena as those in the last section for the same reason that the g-factors of control and qubits are different and magnetic field is much stronger than exchange splittings.

6.5 4-spin problem holding magnetic field

Similarly, we can do the calculation about the 4-spin problem holding the magnetic field, i.e.,$B_z \neq 0$ in Hamiltonian 6.29. Correspondingly,

$$H_{\uparrow}^M = H_{\uparrow} + \begin{pmatrix} \frac{B_{-1}+B_0+B_1+B_2}{2} & 0 & 0 & 0 & 0 \\ 0 & \frac{B_{-1}+B_0+B_1-B_2}{2} & 0 & 0 & 0 \\ 0 & 0 & \frac{B_{-1}+B_0-B_1+B_2}{2} & 0 & 0 \\ 0 & 0 & 0 & \frac{B_{-1}-B_0+B_1+B_2}{2} & 0 \\ 0 & 0 & 0 & 0 & \frac{-B_{-1}+B_0+B_1+B_2}{2} \end{pmatrix} \tag{6.34}$$

$$H_{\downarrow}^M = \begin{pmatrix} H_1^M & 0 \\ 0 & H_2^M \end{pmatrix} \tag{6.35}$$

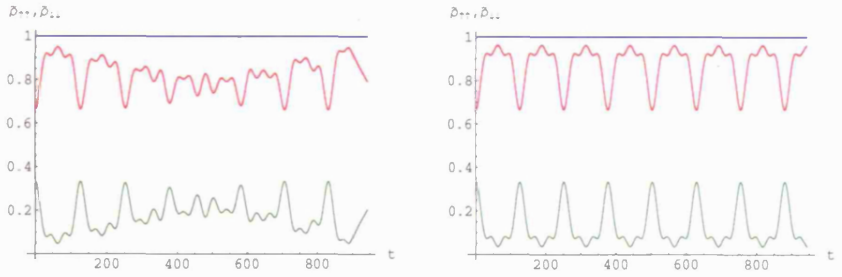

(a) (b)

Fig. 6.4: The spin-up and spin-down populations of the reduced density matrix for the qubit to be measured as functions of time. (a)$\alpha = \frac{\sqrt{2}}{\sqrt{3}}$, $\beta = \frac{1}{\sqrt{3}}$, and $J_0 = 0.1, J_1 = 0.1, J_2 = 0.01$. Red line is $\tilde{\rho}_{\uparrow\uparrow}$, and green line $\tilde{\rho}_{\downarrow\downarrow}$. (b)The same parameters as (a) except $J_2 \sim 0$. Red line is $\tilde{\rho}_{\uparrow\uparrow}$, and green line $\tilde{\rho}_{\downarrow\downarrow}$. Comparing (a) and (b) we can see that the spectator spin damage the coherence between the qubit to be measured and the control spin and the reference qubit.

$$H_1^M = H_1 + \begin{pmatrix} \frac{B_{-1}+B_0+B_1-B_2}{2} & 0 & 0 & 0 \\ 0 & \frac{B_{-1}+B_0-B_1+B_2}{2} & 0 & 0 \\ 0 & 0 & \frac{B_{-1}-B_0+B_1+B_2}{2} & 0 \\ 0 & 0 & 0 & \frac{-B_{-1}+B_0+B_1+B_2}{2} \end{pmatrix} \quad (6.36)$$

$$H_2^M = H_2 + B_2^M \quad (6.37)$$

$$B_2^M = \begin{pmatrix} B_2^{Mtop} & \hat{0} \\ \hat{0} & B_2^{Mbottom} \end{pmatrix} \quad (6.38)$$

$$B_2^{Mtop} = \begin{pmatrix} (B_{-1}+B_0-B_1-B_2)/2 & 0 & 0 \\ 0 & (B_{-1}-B_0+B_1-B_2)/2 & 0 \\ 0 & 0 & (B_{-1}-B_0-B_1+B_2)/2 \end{pmatrix} \quad (6.39)$$

$$B_2^{Mbottom} = \begin{pmatrix} (-B_{-1}+B_0+B_1-B_2)/2 & 0 & 0 \\ 0 & (-B_{-1}+B_0-B_1+B_2)/2 & 0 \\ 0 & 0 & (-B_{-1}-B_0+B_1+B_2)/2 \end{pmatrix} \quad (6.40)$$

where $\hat{0}$ is three by three zero matrix.

By the same methods as in the last section, we can draw the following Figure 6.5. The amplitude of the oscillation is suppressed compared with Figure 6.4.

6.6 Conclusion

We have analyzed the effect of coupling to neighbouring spectator spins on the dynamics of a spin cluster containing two qubit atoms and one control. Clusters of this type are important because of their role in the readout process (see Chapter 7) as well as in the course of the computation itself. We find that the coupling to the

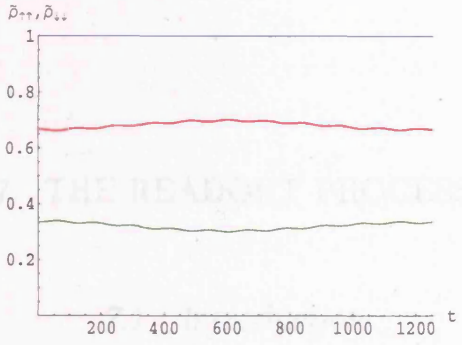

Fig. 6.5: The spin-up and spin-down populations of the reduced density matrix for the qubit to be measured as functions of time. $\alpha = \frac{\sqrt{2}}{\sqrt{3}}$, $\beta = \frac{1}{\sqrt{3}}$, and $J_0 = 0.1, J_1 = 0.1, J_2 = 0.01, B_{-1} = B_1 = B_2 = 5.0, B_0 = 2.0$. Similarly $B_i = B_z g_i \mu_B$. Red line is $\tilde{\rho}_{\uparrow\uparrow}$, and green line $\tilde{\rho}_{\downarrow\downarrow}$. Notice that the amplitude of the oscillation is suppressed compared with Figure 6.4.

spectator rapidly disturbs the state of the rest of the cluster. Specifically:

- From Figure 6.1 and Figure 6.4, we see that the spin populations of the qubit to be measured oscillate with a period that depends on the splitting of the eigenvalues of the spin Hamiltonian. The timescale to hold the quantum information is roughly $\pi/$(the biggest coupling).
- From Figure 6.2 and Figure 6.5 we can see that the application of a magnetic field helps to preserve the quantum information by suppressing spin flip-flop processes, provided that the difference in spin-flip energies is large compared with the exchange interactions. However, such large fields may also interfere with the operation of gates during the computational phase; in the ideal case we would like to choose a field that is small compared with the control-qubit exchange coupling, but large compared with the interactions with any spectator spins.
- So in principle, from this simple model, if we know the concentration of dopants, we can find the average exchange interaction from the 1st nearest neighbour assumed to be J_1, so the time within which measurement must be made is $\frac{\pi}{J}$. Supposing the dopant densities in our sample range from $10^{16}/\text{cm}^3$ to $10^{19}/\text{cm}^3$, according to the above estimate the measurement times range from 10^{-11} to 10^{-13}seconds which is too fast for the practical experiments.

7. THE READOUT PROCESS

7.1 Introduction

It is a very important challenge to be able to read out the quantum information after the completion of a quantum computation. There are many proposals for readout, including via single-spin detection and by optical readout of the state of the ions in the ion-trapped quantum computer. In this chapter we will use density matrix methods to describe our laser readout scheme in the control-qubit system.

First of all, I review the current state of the art in single-spin detection, and then describe the optical readout method used in the ion-trapped quantum computer since our readout scheme is similar to the essential idea used there. Secondly, I introduce our laser readout scheme. The main calculation then falls into two parts:

- (I) In the first part we use a semi-classical model to describe the laser-atom interaction using rotating-wave approximation. At this stage we assume the spontaneous decay rate is very small compared with transition strength.
- (II) In the second part we consider spontaneous decay, by including appropriate Lindblad operators in the master equation for the density matrix.

7.2 Review on previous approaches to readout

7.2.1 Single spin detection

Spins, including nuclear spins and electron spins, are good candidates for quantum bits. Traditional Electron Spin Resonance (ESR) requires a large number of spins ($10^{10} - 10^{15}$). Single-spin detection is only just being developed for the readout of quantum states.

Single spin detection can be realized in several ways:

- Detection using spin resonance.

  Detection of a single-spin resonance is realized using Magnetic Resonance Force Microscopy (MRFM) [48]; see Figure 7.1. The fundamental elements

in MRFM are a mass-loaded silicon cantilever and a samarium cobalt magnetic tip. The measured sample is vitreous silica in which a low density of spins is present. The experiment is performed at a very low temperature to minimize the noise of force and reduce the relaxation rate of spins. The SmCo tip is mounted above the sample to create a large magnetic field gradient into the sample. The field gradient induces the spin located at different depths to resonate at different frequencies, providing selective excitations of spins. The vibration of the magnetic cantilever causes the resonant slice to sweep back and forward, and when the slice finds a spin, the resonance repeatedly flips the spin, and gives the cantilever a slight boost. The change in the frequency of the cantilever is read by the laser interferometer.

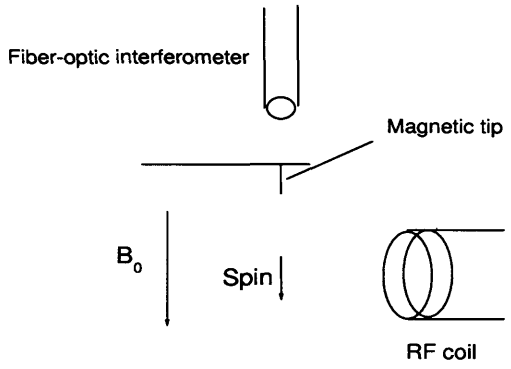

Fig. 7.1: Schematic illustration of MRFM set up for the single spin detection.

The other possible way to detect a single spin using magnetic resonance is using Scanning Tunneling Microscopy (STM) [49]. It is observed that, in an applied magnetic field, the current between the STM tip and a sample surface containing some unpaired spins is modulated at the Larmor frequency. By detecting the radio-frequency signal by a spectrum analyzer, it is possible to locate the spin on the surface. However, no convincing mechanism for this modulation has been identified.

Even if they could be made to work straightforwardly for single spins, these resonance-based methods would suffer from the disadvantage that they detect the occurrence of single-spin transitions, rather than measuring a single-spin state.

- Electrical detection technique

  Electrical detection is performed using quantum dots, field-effect transistor,

and current detection [50]. One method is to use the configuration comprising the quantum dots and quantum point contact. By measuring the current in the quantum point contact channel the change of the charge in the quantum dot is measured. A magnetic field is applied to split the spin up and down states by Zeeman energy. The dot potential is tuned to be in the middle of the spin up state energy level and the spin down state energy level such that if the electron spin is $\downarrow$, it will escape, whereas if the electron spin is $\uparrow$, it will stay. The charge in the quantum dot is constant if the electron contained in the quantum dot is $\uparrow$, whereas the charge changes if the electron spin is $\downarrow$. The electrical detection offers several advantages. Devices are self-contained

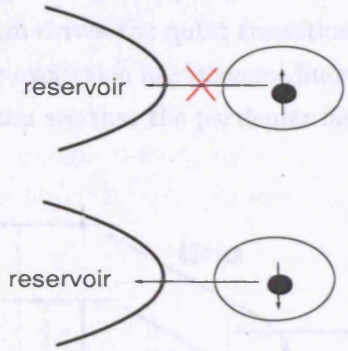

Fig. 7.2: Schematic illustration of single spin detection using quantum dots.

on a chip without needing a laser or optical tables. The electrical devices can be naturally interfaced with conventional electrical circuits. In addition, electrical detection can facilitate the direct study of spin decoherence.

- Optical detection.

  The benefit of optical detection is its capability of being used in a wide range of systems, provided that suitable transitions that are coupled to the spins can be identified. Of all solid state systems, optical detection has been most successfully applied to the nitrogen-vacancy defect centre (NV centre) in diamond [51, 52, 53]. In this NV centre there are strong optical dipole-allowed transitions between the triplet ground state and a first triplet excited state. The induced fluorescence emission is strongly dependent on the electron spin states. By detecting the occurrence of quantum jumps in the fluorescence state of a single centre, it was possible to show that the spin state of a single defect was indeed being determined.

Single-spin detection is an extremely important challenge and necessary for the future successful development of spin-based proposals for the quantum computer. But Single spin detection is also a very difficult problem since a single spin interacts with the environment very weakly and hence also only interacts weakly with measurement devices.

7.2.2 Ion-trapped quantum computer

Trapped and laser-cooled atoms are a promising potential approach for quantum information processing. Blatt *el al.*, [54] used a laser pulse to drive a single $^{40}Ca^{+}$ ion. As shown in Figure 7.3, the upper and lower electronic states $S_{\frac{1}{2}}$, $m = -1/2$, and $D_{\frac{5}{2}}$, $m = -1/2$ of the narrow quadrupole transition 729nm serve as the qubits. Coherent radiation at 729nm drives the qubit transition. Lasers at 397nm, 866nm, and 854nm are used for the excitation of resonance fluorescence for Doppler cooling and optical pumping. We can see that the particular laser frequency 729nm is very

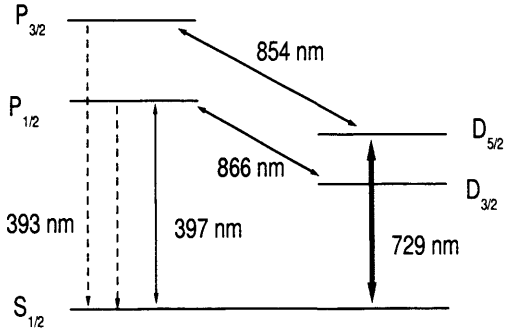

Fig. 7.3: $^{40}Ca^{+}$ ion-trapped quantum computing scheme.

important for the qubit coherence. Meanwhile, lasers 397nm and 866nm can be used to distinguish $S_{\frac{1}{2}}$ and $D_{\frac{5}{2}}$. If we apply these two beams, and there is fluorescence, we can say atoms are in the state $S_{\frac{1}{2}}$; otherwise, they must be in the state $D_{\frac{5}{2}}$.

7.3 Our Readout scheme

Detection of a single electron spin by any technique is an extremely challenging problem. The idea behind the readout scheme proposed by Stonerham *et al.* [23] is analogous to that in ion-trap quantum computing [54]: one searches for a local optical transition that will be on resonance for a particular laser (and so can be

strongly driven, producing many scattered photons) only when a chosen qubit is in a particular one of its two computational basis states. However, in the optically controlled gate scheme, it is the *control* atoms which are chosen to have strong optical transitions in a particular region; the optical transitions proposed for readout are therefore those of a complex consisting of the control and qubit atoms due to the exchange couplings between control and qubits.

Supposing we use qubits 0 to n in the computation, and we also introduce one additional qubit labeled -1. Let c_{ij} be the control atom connecting qubits q_i and q_j. After computation, all control atoms are also in state $|0\rangle$. Suppose we can arrange that q_{-1} which takes no part in the computation is also in the state $|0\rangle$. Now tune the c_{-10} laser to be resonant between the $|000\rangle_g$ ground state of the full system $q_{-1}-c_{-10}-q_0$ and the excited state $|000\rangle_e$ and off resonance with transitions between other spin ground and excited states, and operate it continuously. Rabi oscillations will occur between these two states if and only if q_0 is in the state $|0\rangle$, and scattered photons produced by spontaneous emission when the system is in its excited state will be observed. If photons are observed, q_0 is in $|0\rangle$; if not, q_0 is in $|1\rangle$. See Figure (7.4).

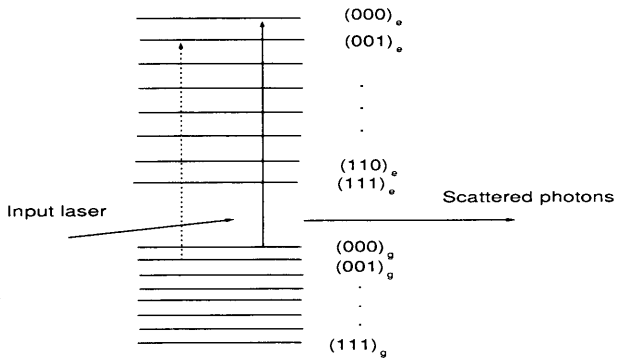

Fig. 7.4: A diagram describing the readout process. '0' refers to spin up state, and '1' refers to spin down state. 'g' means ground state, and 'e' means excited state.

7.4 Laser-atom interaction without considering spontaneous decay

7.4.1 System Hamiltonian and readout methods

Our readout process involves the interaction between a laser and the whole control qubit system. At the moment we neglect the spontaneous decay, i.e., we assume the

spontaneous decay rate is very small. First we define the quantized electric field as the electric field operator at position $\vec{r}$

$$\hat{E}(\vec{r},t) = \vec{E}_0[\hat{a}\exp(-i\Omega t + i\vec{k}\cdot\vec{r}) + \hat{a}^+\exp(i\Omega t - i\vec{k}\cdot\vec{r})], \tag{7.1}$$

where $\vec{k}$ is wavevector, Ω is the laser frequency, and $\hat{a}, \hat{a}^+$ are the photon annihilation and creation operators. We assume that the field is single-mode, the control atom is at the origin. In addition, the laser does not change the spin states, so we can apply the rotating wave approximation to each spin state. After making the rotating wave approximation, the Hamiltonian reads

$$\begin{aligned} H_{L-S} &= |g\rangle[J^g_{QQ}\vec{S}_{-1}\cdot\vec{S}_1 + J^g_{CQ}(\vec{S}_0\cdot\vec{S}_1 + \vec{S}_{-1}\cdot\vec{S}_0) + \sum_{i=-1}^{1}\mu_B B_z g_i S_{iz} + \hbar\omega]\langle g| \\ &\quad + |e\rangle[J^e_{QQ}\vec{S}_{-1}\cdot\vec{S}_1 + J^e_{CQ}(\vec{S}_0\cdot\vec{S}_1 + \vec{S}_{-1}\cdot\vec{S}_0) + \sum_{i=-1}^{1}\mu_B B_z g_i S_{iz}]\langle e| \\ &\quad + V(|g\rangle\langle e|\hat{a}^+ + |e\rangle\langle g|\hat{a}), \end{aligned} \tag{7.2}$$

where J^g_{QQ}, J^e_{QQ} are respectively the qubit-qubit couplings in the ground state and excited state, J^g_{CQ}, J^e_{CQ} are the control-qubit couplings in the ground state and excited state, $\vec{S}_{-1}, \vec{S}_1$ are the qubit spins, $\vec{S}_0$ is the control spin, μ_B is Bohr magneton, B_z is the z-component of magnetic field, and g_i is the g-factor for each spin. Ω is the laser frequency, Ω_0 is the resonant frequency for control atom when there are no exchange couplings, and $\omega = \Omega - \Omega_0$. The electric dipole interaction operator is

$$V = \vec{\mu}\cdot\vec{E}_0, \tag{7.3}$$

where $\vec{\mu}$ is the dipole matrix element $\langle g|e\vec{r}|e\rangle$, and $\vec{E}_0$ is the amplitude of the electric field. So the matrix of this Hamiltonian spanned by $|g\rangle|1_p\rangle$ and $|e\rangle|0_p\rangle$ is a 16×16 matrix, where $|1_p\rangle$ is the one-photon state.

Because the dipole interactions do not change the spin states, and the exchange interactions does not change $\sum_i S_{iz}$, we can separate the whole matrix into 4 blocks:

$$H_{L-S} = \begin{pmatrix} (H^1_{L-S}) & 0 & 0 & 0 \\ 0 & (H^2_{L-S}) & 0 & 0 \\ 0 & 0 & (H^3_{L-S}) & 0 \\ 0 & 0 & 0 & (H^4_{L-S}) \end{pmatrix} \tag{7.4}$$

$$H^1_{L-S} = \begin{array}{c} \\ |\uparrow\uparrow\uparrow\rangle^g|1_p\rangle \\ |\uparrow\uparrow\uparrow\rangle^e|0_p\rangle \end{array} \begin{array}{c} \begin{array}{cc} |\uparrow\uparrow\uparrow\rangle^g|1_p\rangle & |\uparrow\uparrow\uparrow\rangle^e|0_p\rangle \end{array} \\ \begin{pmatrix} \frac{J^g_{QQ}+2J^g_{CQ}}{4} + \hbar\omega + \tilde{B}_1 & V \\ V & \frac{J^e_{QQ}+2J^e_{CQ}}{4} + \tilde{B}_1 \end{pmatrix} \end{array} \tag{7.5}$$

$$\tilde{B}_1 = B_{-1} + B_0 + B_1, \tag{7.6}$$

where $B_i = \frac{\mu_B B_z g_i}{2}$.

$$H^2_{L-S} = \begin{array}{c} \\ |g\rangle|1_p\rangle \\ |e\rangle|0_p\rangle \end{array} \begin{array}{c} \begin{array}{cc} |g\rangle|1_p\rangle & |e\rangle|0_p\rangle \end{array} \\ \begin{pmatrix} H^{2g}_{L-S} + \tilde{B}_2 & VI \\ VI & H^{2e}_{L-S} + \tilde{B}_2 \end{pmatrix} \end{array} \tag{7.7}$$

$$H^{2g}_{L-S} = \begin{array}{c} \\ |\uparrow\uparrow\downarrow\rangle^g|1_p\rangle \\ |\uparrow\downarrow\uparrow\rangle^g|1_p\rangle \\ |\downarrow\uparrow\uparrow\rangle^g|1_p\rangle \end{array} \begin{array}{c} \begin{array}{ccc} |\uparrow\uparrow\downarrow\rangle^g|1_p\rangle & |\uparrow\downarrow\uparrow\rangle^g|1_p\rangle & |\downarrow\uparrow\uparrow\rangle^g|1_p\rangle \end{array} \\ \begin{pmatrix} \frac{-J^g_{QQ}}{4} + \hbar\omega & \frac{J^g_{CQ}}{2} & \frac{J^g_{QQ}}{2} \\ \frac{J^g_{CQ}}{2} & \frac{J^g_{QQ} - 2J^g_{CQ}}{4} + \hbar\omega & \frac{J^g_{CQ}}{2} \\ \frac{J^g_{QQ}}{2} & \frac{J^g_{CQ}}{2} & \frac{-J^g_{QQ}}{4} + \hbar\omega \end{pmatrix} \end{array} \tag{7.8}$$

$$H^{2e}_{L-S} = \begin{array}{c} \\ |\uparrow\uparrow\downarrow\rangle^e|0_p\rangle \\ |\uparrow\downarrow\uparrow\rangle^e|0_p\rangle \\ |\downarrow\uparrow\uparrow\rangle^e|0_p\rangle \end{array} \begin{array}{c} \begin{array}{ccc} |\uparrow\uparrow\downarrow\rangle^e|0_p\rangle & |\uparrow\downarrow\uparrow\rangle^e|0_p\rangle & |\downarrow\uparrow\uparrow\rangle^e|0_p\rangle \end{array} \\ \begin{pmatrix} \frac{-J^e_{QQ}}{4} & \frac{J^e_{CQ}}{2} & \frac{J^e_{QQ}}{2} \\ \frac{J^e_{CQ}}{2} & \frac{J^e_{QQ} - 2J^e_{CQ}}{4} & \frac{J^e_{CQ}}{2} \\ \frac{J^e_{QQ}}{2} & \frac{J^e_{CQ}}{2} & \frac{-J^e_{QQ}}{4} \end{pmatrix} \end{array} \tag{7.9}$$

$$\tilde{B}_2 = \begin{pmatrix} B_{-1} + B_0 - B_1 & 0 & 0 \\ 0 & B_{-1} - B_0 + B_1 & 0 \\ 0 & 0 & -B_{-1} + B_0 + B_1 \end{pmatrix}, \tag{7.10}$$

where I is a 3×3 identity matrix.

$$H^3_{L-S} = \begin{array}{c} \\ |g\rangle|1_p\rangle \\ |e\rangle|0_p\rangle \end{array} \begin{array}{c} \begin{array}{cc} |g\rangle|1_p\rangle & |e\rangle|0_p\rangle \end{array} \\ \begin{pmatrix} H^{3g}_{L-S} + \tilde{B}_3 & VI \\ VI & H^{3e}_{L-S} + \tilde{B}_3 \end{pmatrix} \end{array} \tag{7.11}$$

$$H^{3g}_{L-S} = \begin{array}{c} \\ |\uparrow\downarrow\downarrow\rangle^g|1_p\rangle \\ |\downarrow\uparrow\downarrow\rangle^g|1_p\rangle \\ |\downarrow\downarrow\uparrow\rangle^g|1_p\rangle \end{array} \begin{array}{c} \begin{array}{ccc} |\uparrow\downarrow\downarrow\rangle^g|1_p\rangle & |\downarrow\uparrow\downarrow\rangle^g|1_p\rangle & |\downarrow\downarrow\uparrow\rangle^g|1_p\rangle \end{array} \\ \begin{pmatrix} \frac{-J^g_{QQ}}{4} + \hbar\omega & \frac{J^g_{CQ}}{2} & \frac{J^g_{QQ}}{2} \\ \frac{J^g_{CQ}}{2} & \frac{J^g_{QQ} - 2J^g_{CQ}}{4} + \hbar\omega & \frac{J^g_{CQ}}{2} \\ \frac{J^g_{QQ}}{2} & \frac{J^g_{CQ}}{2} & \frac{-J^g_{QQ}}{4} + \hbar\omega \end{pmatrix} \end{array} \tag{7.12}$$

$$H^{3e}_{L-S} = \begin{array}{c} \\ |\uparrow\downarrow\downarrow\rangle^e|0_p\rangle \\ |\downarrow\uparrow\downarrow\rangle^e|0_p\rangle \\ |\downarrow\downarrow\uparrow\rangle^e|0_p\rangle \end{array} \begin{array}{c} \begin{array}{ccc} |\uparrow\downarrow\downarrow\rangle^e|0_p\rangle & |\downarrow\uparrow\downarrow\rangle^e|0_p\rangle & |\downarrow\downarrow\uparrow\rangle^e|0_p\rangle \end{array} \\ \begin{pmatrix} \frac{-J^e_{QQ}}{4} & \frac{J^e_{CQ}}{2} & \frac{J^e_{QQ}}{2} \\ \frac{J^e_{CQ}}{2} & \frac{J^e_{QQ} - 2J^e_{CQ}}{4} & \frac{J^e_{CQ}}{2} \\ \frac{J^e_{QQ}}{2} & \frac{J^e_{CQ}}{2} & \frac{-J^e_{QQ}}{4} \end{pmatrix} \end{array} \tag{7.13}$$

$$\tilde{B}_3 = \begin{pmatrix} B_{-1} - B_0 - B_1 & 0 & 0 \\ 0 & -B_{-1} + B_0 - B_1 & 0 \\ 0 & 0 & -B_{-1} - B_0 + B_1 \end{pmatrix}, \tag{7.14}$$

where I is a 3×3 identity matrix.

$$H^4_{L-S} = \begin{array}{c} \\ |\downarrow\downarrow\downarrow\rangle^g|1_p\rangle \\ |\downarrow\downarrow\downarrow\rangle^e|0_p\rangle \end{array} \begin{array}{c} \begin{array}{cc} |\downarrow\downarrow\downarrow\rangle^g|1_p\rangle & |\downarrow\downarrow\downarrow\rangle^e|0_p\rangle \end{array} \\ \begin{pmatrix} \frac{J^g_{QQ}+2J^g_{CQ}}{4} + \hbar\omega - \tilde{B}_1 & V \\ V & \frac{J^e_{QQ}+2J^e_{CQ}}{4} - \tilde{B}_1 \end{pmatrix} \end{array}. \quad (7.15)$$

Recalling the readout scheme, there are two ways to measure the qubit:

- Method I

  Tune ω to be ω_R so that we can get Rabi oscillation between $|\uparrow\uparrow\uparrow\rangle^g$ and $|\uparrow\uparrow\uparrow\rangle^e$. If scattered photons are observed, we can say the qubit is in $|\uparrow\rangle$. Because $|\uparrow\uparrow\uparrow\rangle$ does not couple with any other states by Heisenberg exchange interaction, in order for Rabi oscillation to occur, the frequency we need is

  $$\omega_R = \frac{J^e_{QQ} + 2J^e_{CQ}}{4} - (\frac{J^g_{QQ} + 2J^g_{CQ}}{4}) + \omega_0. \quad (7.16)$$

  Meanwhile, we cannot get Rabi oscillation between $|\uparrow\uparrow\downarrow\rangle^g$ and $|\uparrow\uparrow\downarrow\rangle^e$ only if ω_R is not accidently equal to the laser frequency that can make out Rabi oscillation between $|\uparrow\uparrow\downarrow\rangle^g$ and $|\uparrow\uparrow\downarrow\rangle^e$. So if we did not observe scattered photons we can say the qubit is in $|\downarrow\rangle$.

- Method II

  We can tune the laser frequency ω to get Rabi oscillation between $|\uparrow\uparrow\downarrow\rangle^g$ and $|\uparrow\uparrow\downarrow\rangle^e$. This method is slightly more complicated because $|\uparrow\uparrow\downarrow\rangle$ is coupled to the other two states $|\uparrow\downarrow\uparrow\rangle$ and $|\downarrow\uparrow\uparrow\rangle^g$ by exchange couplings. Therefore, if the exchange couplings are much smaller than the energy levels splitting created by magnetic field, the energy level will be shifted and the corresponding eigenstate is the mixture of these states. If $B_i >> J^e_{CQ} >> J^e_{QQ}$, the eigenstates are approximately, $|\uparrow\downarrow\uparrow\rangle$,$\frac{1}{\sqrt{2}}(|\uparrow\uparrow\downarrow\rangle + |\downarrow\uparrow\uparrow\rangle)$, and $\frac{1}{\sqrt{2}}(|\uparrow\uparrow\downarrow\rangle - |\downarrow\uparrow\uparrow\rangle)$. So we should tune the laser frequency to get Rabi oscillation between energy levels $\frac{1}{\sqrt{2}}(|\uparrow\uparrow\downarrow\rangle^g - |\downarrow\uparrow\uparrow\rangle^g)$ and $\frac{1}{\sqrt{2}}(|\uparrow\uparrow\downarrow\rangle^e - |\downarrow\uparrow\uparrow\rangle^e)$, or $\frac{1}{\sqrt{2}}(|\uparrow\uparrow\downarrow\rangle^g + |\downarrow\uparrow\uparrow\rangle^g)$ and $\frac{1}{\sqrt{2}}(|\uparrow\uparrow\downarrow\rangle^e + |\downarrow\uparrow\uparrow\rangle^e)$. In other words, $\hbar\omega'_R$ is equal to the difference between the eigenvalues of the above two states.

7.4.2 Numerical results

Readout method I

We tune the laser frequency $\omega_R - \omega_0 = 0.0049725$ to get the resonance between $|\uparrow\uparrow\uparrow\rangle^g$ and $|\uparrow\uparrow\uparrow\rangle^e$. The populations of $|\uparrow\uparrow\uparrow\rangle^g$, $|\uparrow\uparrow\uparrow\rangle^e$, $|\uparrow\uparrow\downarrow\rangle^g$ and $|\uparrow\uparrow\downarrow\rangle^e$ are shown in Figure 7.5 below.

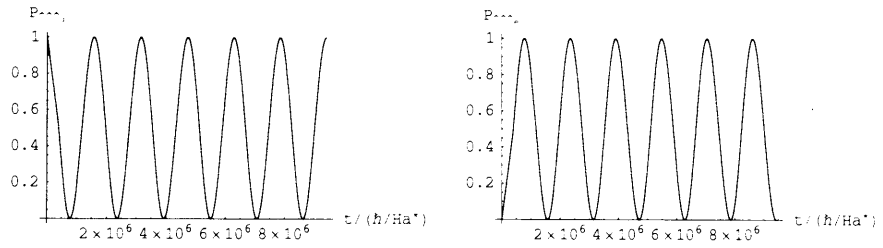

(a)$P_{\uparrow\uparrow\uparrow_g}$ (b)$P_{\uparrow\uparrow\uparrow_e}$

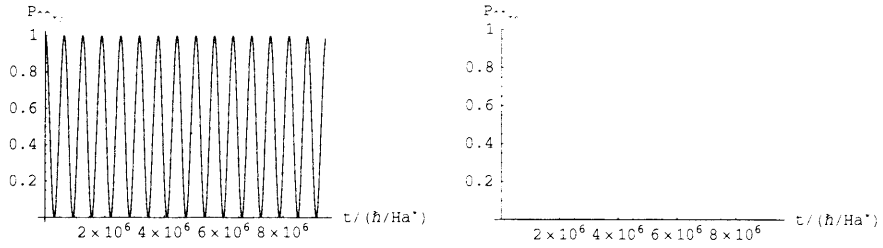

(c)$P_{\uparrow\uparrow\downarrow_g}$ (d)$P_{\uparrow\uparrow\downarrow_e}$

Fig. 7.5: Readout process when we tune the laser to get resonance between $|\uparrow\uparrow\uparrow\rangle^g$ and $|\uparrow\uparrow\uparrow\rangle^e$. Populations of several related spin states are plotted as functions of time. Because $J^e >> J^g, J_{CQ} > J_{QQ}$, and $B_i >> J$, we can select the parameters: $J^g_{QQ} = 0.00001, J^g_{QC} = 0.0001, J^e_{QQ} = 0.0001, J^e_{QC} = 0.01, V = 0.000002, B_{-1} = B_1 = 0.5, B_0 = 0.3$. At the moment we assume that V is smaller than the exchange couplings. The time unit is $\hbar$/Hatree* $\approx 10^{-14}$second according to data from the previous chapters. Notice Rabi oscillation between $|\uparrow\uparrow\uparrow\rangle^g$ and $|\uparrow\uparrow\uparrow\rangle^e$, but no Rabi oscillation between $|\uparrow\uparrow\downarrow\rangle^g$ and $|\uparrow\uparrow\downarrow\rangle^e$.

From Figure(7.5), we can see the Rabi oscillation between $|\uparrow\uparrow\uparrow\rangle^g$ and $|\uparrow\uparrow\uparrow\rangle^e$, but no Rabi oscillation between $|\uparrow\uparrow\downarrow\rangle^g$ and $|\uparrow\uparrow\downarrow\rangle^e$, when we tune the laser to be on resonance between $|\uparrow\uparrow\uparrow\rangle^g$ and $|\uparrow\uparrow\uparrow\rangle^e$. In addition we also find that the populations of other excited spin states $|\uparrow\downarrow\uparrow\rangle$ and $|\downarrow\uparrow\uparrow\rangle$ are always very small. In other words no population is in the excited states of those three spin states with total $S_z = 1/2$, so no photons can be emitted spontaneously from those three spin states, but there is lots of population in the excited state of $|\uparrow\uparrow\uparrow\rangle$, so the probability of spontaneous emission is much larger from $|\uparrow\uparrow\uparrow\rangle_e$.

Readout method II

When we keep the parameters unchanged and tune the laser to be resonant between $|\uparrow\uparrow\downarrow\rangle^g$ and $|\uparrow\uparrow\downarrow\rangle^e$ with $\omega_R - \omega_0 = -0.0000675$, the exchange interactions interrupt the pure Rabi oscillation. As shown in Figure 7.6–Figure 7.8 there is no Rabi oscillation between $|\uparrow\uparrow\uparrow\rangle^g$ and $|\uparrow\uparrow\uparrow\rangle^e$, meanwhile there are several transitions between $|\uparrow\uparrow\downarrow\rangle^g$, $|\uparrow\uparrow\downarrow\rangle^e$, $|\downarrow\uparrow\uparrow\rangle^g$, and $|\downarrow\uparrow\uparrow\rangle^e$.

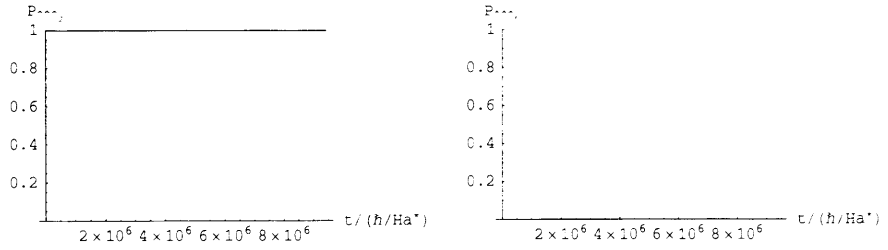

(a)$P_{\uparrow\uparrow\uparrow_g}$ (b)$P_{\uparrow\uparrow\uparrow_e}$

Fig. 7.6: Readout process when we tune the laser to get resonance between $|\uparrow\uparrow\downarrow\rangle^g$ and $|\uparrow\uparrow\downarrow\rangle^e$. The populations of several spin states are plotted as a function of time. Notice that no Rabi oscillation between $|\uparrow\uparrow\uparrow\rangle^g$ and $|\uparrow\uparrow\uparrow\rangle^e$

7.4.3 Comments on the readout method II: perturbation theory

In this section, we will use time-dependent perturbation theory to treat the Hamiltonian H^{2gx}_{L-S}, which is

$$H^2_{L-S} = \begin{array}{c} \\ |g\rangle|1_p\rangle \\ |e\rangle|0_p\rangle \end{array} \begin{array}{c} \begin{array}{cc} |g\rangle|1_p\rangle & |e\rangle|0_p\rangle \end{array} \\ \begin{pmatrix} H^{2g}_{L-S} + \tilde{B}_2 & VI \\ VI & H^{2e}_{L-S} + \tilde{B}_2 \end{pmatrix} \end{array} \tag{7.17}$$

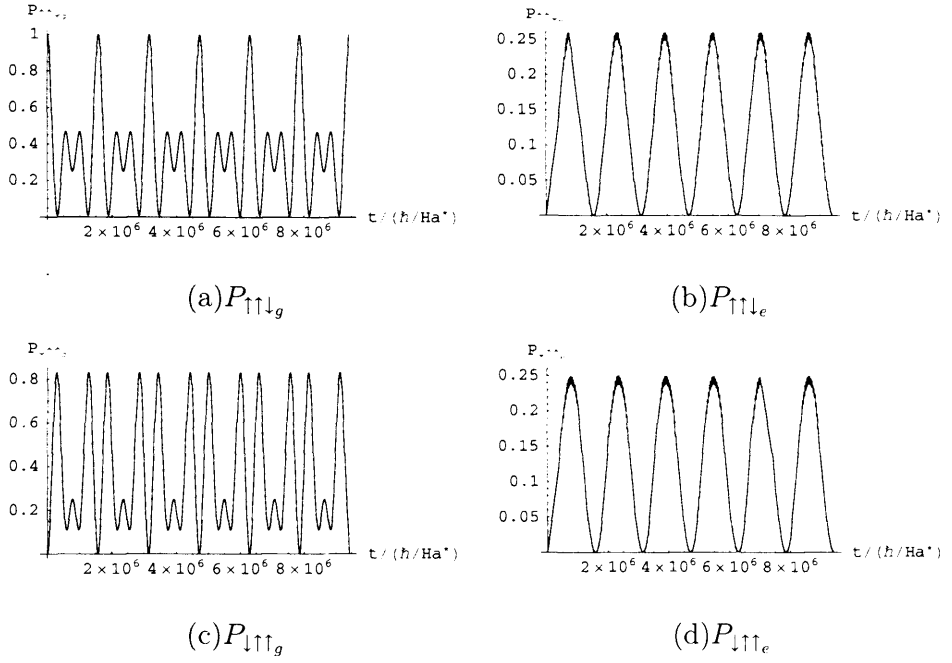

(a)$P_{\uparrow\uparrow\downarrow_g}$ (b)$P_{\uparrow\uparrow\downarrow_e}$

(c)$P_{\downarrow\uparrow\uparrow_g}$ (d)$P_{\downarrow\uparrow\uparrow_e}$

Fig. 7.7: Readout process when we tune the laser to get resonance between $|\uparrow\uparrow\downarrow\rangle^g$ and $|\uparrow\uparrow\downarrow\rangle^e$. The populations of several spin states are plotted as a function of time. Notice that Rabi oscillation is perturbed by the exchange couplings.

$$H^{2g}_{L-S} = \begin{array}{c} \\ |\uparrow\uparrow\downarrow\rangle^g|1_p\rangle \\ |\uparrow\downarrow\uparrow\rangle^g|1_p\rangle \\ |\downarrow\uparrow\uparrow\rangle^g|1_p\rangle \end{array} \begin{array}{c} \begin{array}{ccc} |\uparrow\uparrow\downarrow\rangle^g|1_p\rangle & |\uparrow\downarrow\uparrow\rangle^g|1_p\rangle & |\downarrow\uparrow\uparrow\rangle^g|1_p\rangle \end{array} \\ \begin{pmatrix} \frac{-J^g_{QQ}}{4}+\hbar\omega & \frac{J^g_{CQ}}{2} & \frac{J^g_{QQ}}{2} \\ \frac{J^g_{QQ}}{2} & \frac{J^g_{QQ}-2J^g_{CQ}}{4}+\hbar\omega & \frac{J^g_{CQ}}{2} \\ \frac{J^g_{QQ}}{2} & \frac{J^g_{CQ}}{2} & \frac{-J^g_{QQ}}{4}+\hbar\omega \end{pmatrix} \end{array} \tag{7.18}$$

$$H^{2e}_{L-S} = \begin{array}{c} \\ |\uparrow\uparrow\downarrow\rangle^e|0_p\rangle \\ |\uparrow\downarrow\uparrow\rangle^e|0_p\rangle \\ |\downarrow\uparrow\uparrow\rangle^e|0_p\rangle \end{array} \begin{array}{c} \begin{array}{ccc} |\uparrow\uparrow\downarrow\rangle^e|0_p\rangle & |\uparrow\downarrow\uparrow\rangle^e|0_p\rangle & |\downarrow\uparrow\uparrow\rangle^e|0_p\rangle \end{array} \\ \begin{pmatrix} \frac{-J^e_{QQ}}{4} & \frac{J^e_{CQ}}{2} & \frac{J^e_{QQ}}{2} \\ \frac{J^e_{QQ}}{2} & \frac{J^e_{QQ}-2J^e_{CQ}}{4} & \frac{J^e_{CQ}}{2} \\ \frac{J^e_{QQ}}{2} & \frac{J^e_{CQ}}{2} & \frac{-J^e_{QQ}}{4} \end{pmatrix} \end{array} \tag{7.19}$$

$$\tilde{B}_2 = \begin{pmatrix} B_{-1}+B_0-B_1 & 0 & 0 \\ 0 & B_{-1}-B_0+B_1 & 0 \\ 0 & 0 & -B_{-1}+B_0+B_1 \end{pmatrix}, \tag{7.20}$$

where I is a 3×3 identity matrix. And by using first-order time-dependent perturbation theory, we can see why we got several transitions in the readout method II.

Time-dependent perturbation theory

First we introduce time-dependent perturbation theory. Assuming the unperturbed Hamiltonian $\hat{H}_0\Psi_k^{(0)} = E_k^{(0)}\Psi_k^{(0)}$ can be solved exactly, substituting into time-dependent Schrödinger equation, we get the eigenfunctions of $\hat{H} = \hat{H}_0 + V$, where V is the perturbation.

$$\Psi = \sum a_k(t)\Psi_k^{(0)} \tag{7.21}$$

$$i\hbar\partial(\Psi_k^{(0)})/\partial(t) = \hat{H}_0\Psi_k^{(0)} \tag{7.22}$$

$$i\hbar\partial(\Psi)/\partial(t) = (\hat{H}_0 + V)\Psi \tag{7.23}$$

$$i\hbar\partial(a_m)/\partial(t) = \sum_k V_{mk}(t)a_k \tag{7.24}$$

$$V_{mk}(t) = V_{mk}e^{i/\hbar(E_m^{(0)} - E_k^{(0)})t}. \tag{7.25}$$

Assuming $a_m = a_m^{(0)} + a_m^{(1)}$, then

$$\tag{7.26}$$

$$i\hbar\partial(a_m^{(1)})/\partial(t) = \sum_k V_{mk}(t)a_k^{(0)}. \tag{7.27}$$

After getting a_m,we can construct the density matrix,

$$\rho_{mn} = a_m a_n^* e^{i/\hbar(-E_m^{(0)} + E_n^{(0)})t}. \tag{7.28}$$

Transforming matrix

Our idea is that

- use the matrix X_0 constructed by eigenvectors of the spin Hamiltonian to diagonalise the matrix.

$$X_0 = \begin{pmatrix} EM_g & 0 \\ 0 & EM_e \end{pmatrix}, \tag{7.29}$$

  where EM_g, EM_e are the matrices constructed from the eigenvectors of $H_{L-S}^{2g} + \tilde{B}_2$ and $H_{L-S}^{2e} + \tilde{B}_2$ respectively.

- use the matrix X to diagonalize the Hamiltonian further.

$$X = \begin{pmatrix} A & B \\ C & D \end{pmatrix} \tag{7.30}$$

$$A = \begin{pmatrix} \frac{1}{\sqrt{2}} & 0 & 0 \\ 0 & 1 & 0 \\ 0 & 0 & 1 \end{pmatrix} \tag{7.31}$$

$$B = \begin{pmatrix} \frac{1}{\sqrt{2}} & 0 & 0 \\ 0 & 0 & 0 \\ 0 & 0 & 0 \end{pmatrix} \tag{7.32}$$

$$C = \begin{pmatrix} \frac{1}{\sqrt{2}} & 0 & 0 \\ 0 & 0 & 0 \\ 0 & 0 & 0 \end{pmatrix} \tag{7.33}$$

$$D = \begin{pmatrix} -\frac{1}{\sqrt{2}} & 0 & 0 \\ 0 & 1 & 0 \\ 0 & 0 & 1 \end{pmatrix} \tag{7.34}$$

- extract the off-diagonal terms as the perturbations, so we can analyze how the external factors, e.g., exchange couplings, disturb the Rabi oscillation.
- use time-dependent perturbation theory to calculate the first order perturbation. See if it is consistent with the previous precise result.

Therefore the total Hamiltonian is

$$\hat{H} = X X_0^{-1} H_{L-S}^2 X_0 X, \tag{7.35}$$

By now we have got $\hat{H}$, we can consider the matrix constructed by the diagonal terms of $\hat{H}$ as $\hat{H}_0$, and the matrix constructed by the off-diagonal terms in $\hat{H}$ is considered as the perturbation. If we use the parameters in the readout method II, one can see the off-diagonal terms in $\hat{H}$ are much smaller than diagonal terms. So we can use first-order perturbation theory to calculate the density matrix, and then transform it to the original basis using X_0 and X.

Numerical results

We can select the same parameters as the readout method II. We found the populations of each spin states from perturbation theory are nearly the same as those previous precise results (Figure 7.8). Due to the exchange couplings between electrons, the transforming matrices X_0, X transform $V \times I$ a diagonal matrix to a

matrix with off-diagonal terms, so the exchange couplings may disturb the Rabi oscillations if we use the readout method II.

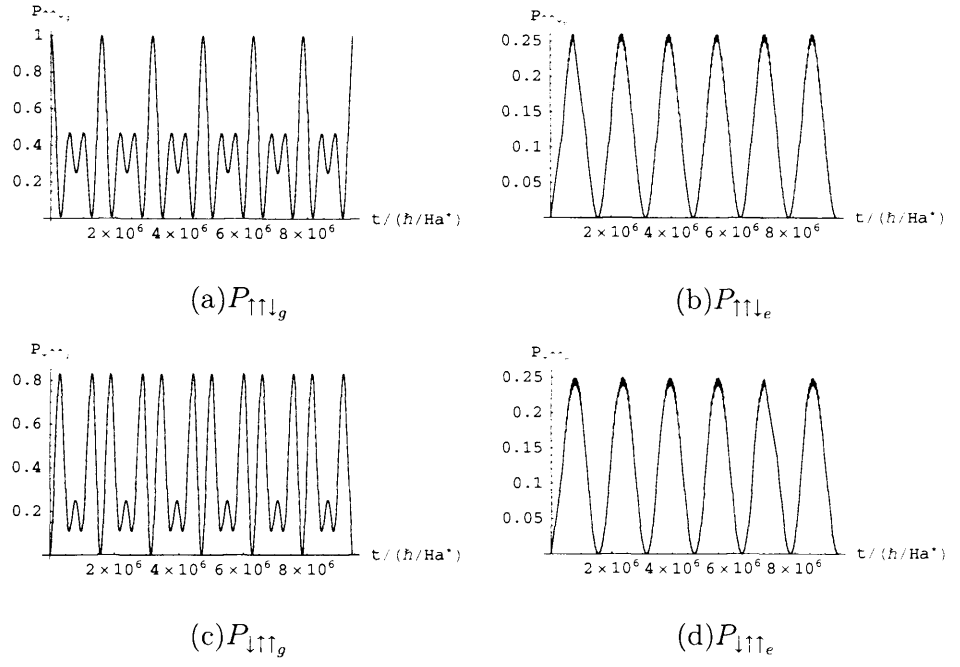

(a)$P_{\uparrow\uparrow\downarrow_g}$ (b)$P_{\uparrow\uparrow\downarrow_e}$

(c)$P_{\downarrow\uparrow\uparrow_g}$ (d)$P_{\downarrow\uparrow\uparrow_e}$

Fig. 7.8: Readout process when we tune the laser to get resonance between $|\uparrow\uparrow\downarrow\rangle^g$ and $|\uparrow\uparrow\downarrow\rangle^e$. The populations of several spin states calculated from time-dependent perturbation theory are plotted as a function of time. Notice that Rabi oscillation is perturbed by the exchange couplings. The lower peak oscillation in (a) comes from fluctuation of spin-spin couplings.

7.5 Readout with considering spontaneous decay rate

7.5.1 The Markovian limit and Lindblad equation

The spontaneous decay process involves the interaction between the system being considered and the environment. In the Markovian limit the Lindblad equation describes the time evolution of the reduced density matrix of the system being considered. The theory of quantum operations supposes that things just 'happen' to the system's density matrix–we don't ask why, or how fast. Now let us start looking at the dynamics, but let's do so on a timescale that has to satisfy two conditions.

- it should be small compared with the characteristic timescale of the system–so the system density matrix only evolves 'a little bit' in this time interval (i.e.

$\ll \tau_S$).

- But it should also be long compared with the time over which the environment 'forgets' its information about the system.

¿From the above two conditions, one can derive the Lindblad master equation to be [55],

$$\frac{d\hat{\rho}_S}{dt} = \frac{1}{i\hbar}[\hat{H}, \hat{\rho}_S] + \sum_k \left[\hat{L}_k \rho_S \hat{L}_k^\dagger - \frac{1}{2}\{\rho_S, \hat{L}_k^\dagger \hat{L}_k\}\right], \tag{7.36}$$

where $\{\hat{A}, \hat{B}\}$ represents the anti-commutator $\hat{A}\hat{B} + \hat{B}\hat{A}$. $\hat{\rho}_S$ is the reduced density matrix of the system after we trace out the freedoms of the environment, and $\hat{L}_k$ is the Lindblad operator.

7.5.2 Apply Lindblad equation to the laser-atom interaction

In the last four sections we have calculated the density matrix which satisfies

$$\frac{d\hat{\rho}_S}{dt} = \frac{1}{i\hbar}[\hat{H}, \hat{\rho}_S]. \tag{7.37}$$

This is closed system only including control-qubit system and photons. Now we can add some Lindblad operators which correspond to spontaneous emissions of electric dipole type. For simplification we assume that the spontaneous decay rate is the same for all the excited spin states. So Lindblad equation for our problem is

$$\frac{d\hat{\rho}_S}{dt} = \frac{1}{i\hbar}[\hat{H}, \hat{\rho}_S] + \gamma \sum_k \left[\hat{L}_k \rho_S \hat{L}_k^\dagger - \frac{1}{2}\{\rho_S, \hat{L}_k^\dagger \hat{L}_k\}\right], \tag{7.38}$$

where γ is the spontaneous emission rate. Because this kind of Lindblad operator only de-excites the excited states to ground and does not involve changing spin, we can also separately deal with the total density matrix.

- For the sub-space spanned by $\uparrow\uparrow\uparrow_g$ and $\uparrow\uparrow\uparrow_e$, Lindblad operator is

$$L_{\uparrow\uparrow\uparrow} = \begin{array}{c} \\ |g\rangle \\ |e\rangle \end{array} \begin{array}{c} \begin{array}{cc} |g\rangle & |e\rangle \end{array} \\ \begin{pmatrix} 0 & 1 \\ 0 & 0 \end{pmatrix} \end{array} \tag{7.39}$$

- For the sub-space spanned by $\uparrow\uparrow\downarrow_{g,e}$, $\uparrow\downarrow\uparrow_{g,e}$, and $\downarrow\uparrow\uparrow_{g,e}$, Lindblad operators are 6×6 matrixes:

$$L_i = \begin{array}{c} \\ |g\rangle \\ |e\rangle \end{array} \begin{array}{c} \begin{array}{cc} |g\rangle & |e\rangle \end{array} \\ \begin{pmatrix} \hat{0} & l_i \\ \hat{0} & \hat{0} \end{pmatrix} \end{array} \tag{7.40}$$

$$l_1 = \begin{pmatrix} 1 & 0 & 0 \\ 0 & 0 & 0 \\ 0 & 0 & 0 \end{pmatrix} \tag{7.41}$$

$$l_2 = \begin{pmatrix} 0 & 0 & 0 \\ 0 & 1 & 0 \\ 0 & 0 & 0 \end{pmatrix} \tag{7.42}$$

$$l_3 = \begin{pmatrix} 0 & 0 & 0 \\ 0 & 0 & 0 \\ 0 & 0 & 1 \end{pmatrix} \tag{7.43}$$

$$\hat{0} = \begin{pmatrix} 0 & 0 & 0 \\ 0 & 0 & 0 \\ 0 & 0 & 0 \end{pmatrix}. \tag{7.44}$$

We will do the numerical calculation on this sub-space.

- similarly for the other sub-spaces.

7.5.3 *Numerical calculation*

¿From Figure 7.10, we can see that: (i) The population of $|\uparrow\uparrow\downarrow\rangle^e$ decay to zero approximate as a rate of γ; (ii)no Rabi oscillation is driven between $|\uparrow\uparrow\downarrow\rangle^g$ and $|\uparrow\uparrow\downarrow\rangle^e$; (iii) there is a little population on the excited states; (iv) the population of $|\downarrow\uparrow\uparrow\rangle^e$ arises because the qubit-qubit coupling flips the spins before the spontaneous decay.(v) The resonance between $|\uparrow\uparrow\downarrow\rangle^g$ and $|\downarrow\uparrow\uparrow\rangle^g$ as this figure shows results from double-photon effect. Because these two states are degenerate(in this model), the laser drives the ground to excited state, and the excited state decays quickly to another ground state.

7.6 *Conclusion*

We have presented several calculations of the readout process. We started by neglecting spontaneous decay, then introduced a perturbation-theory calculation to highlight the important interactions occurring in readout method II, and finally introduced a description of spontaneous decay into the readout process.

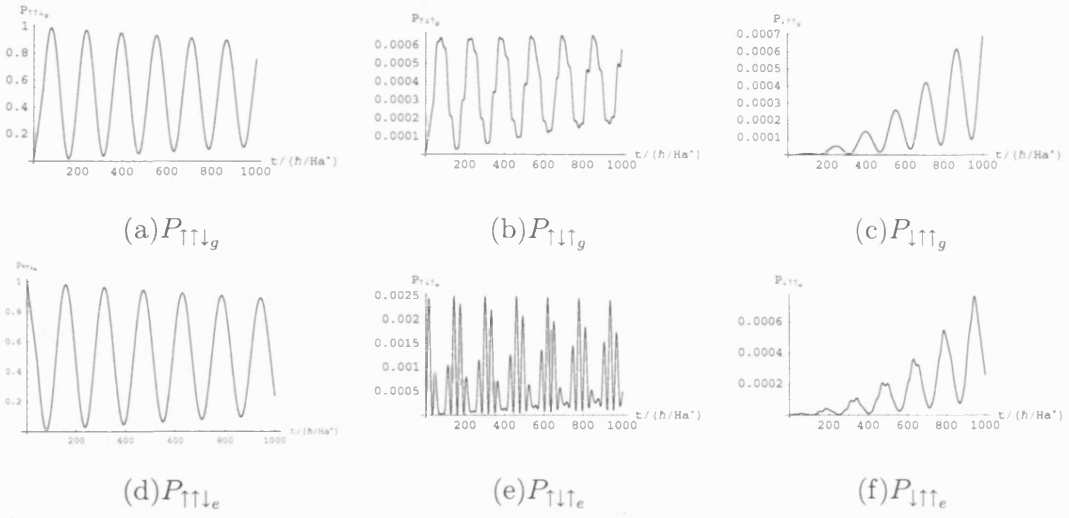

Fig. 7.9: Readout process considering spontaneous decay when we tune the laser to get a resonance between $|\uparrow\uparrow\downarrow\rangle^g$ and $|\uparrow\uparrow\downarrow\rangle^e$. We can select the parameters to be $J^g_{QQ} = 0.00004, J^e_{QQ} = 0.0001, J^g_{CQ} = 0.0001, J^e_{CQ} = 0.001, B_{-1} = 0.5, B_0 = 0.3, B_1 = 0.5, \Delta = -0.0000675, \gamma = 1/3000$ (unit:$Hartree^\star$), where Δ is tuned to have resonance between $|\uparrow\uparrow\downarrow\rangle^g$ and $|\uparrow\uparrow\downarrow\rangle^e$, and the initial state is $|\uparrow\uparrow\downarrow\rangle^e$ because we expect to see the effect of the spontaneous decay. Here $V = 0.02 \gg \gamma$. The related populations of several spin states are plotted as a function of time. Notice that Rabi oscillation is driven between $|\uparrow\uparrow\downarrow\rangle^g$ and $|\uparrow\uparrow\downarrow\rangle^e$.

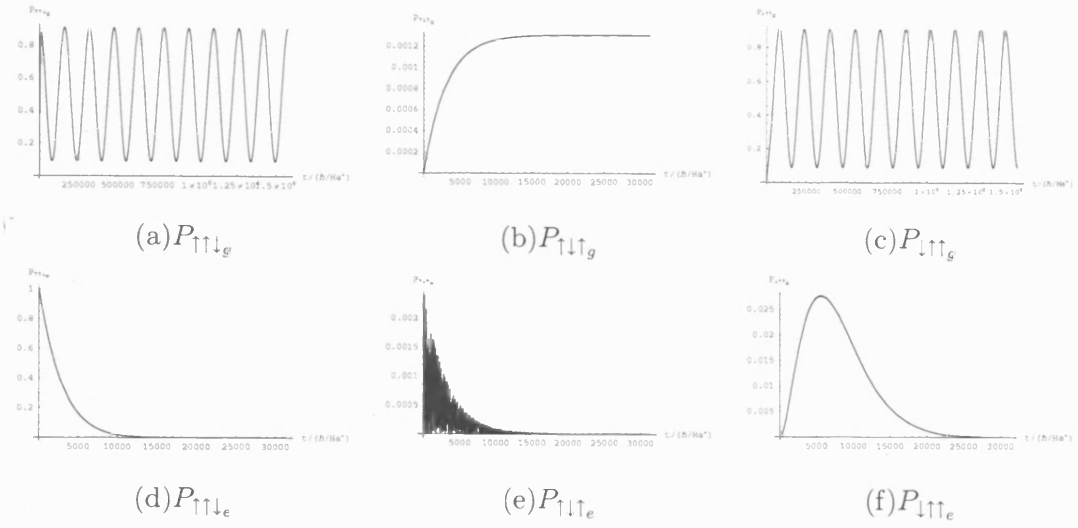

(a)$P_{\uparrow\uparrow\downarrow_g}$ (b)$P_{\uparrow\downarrow\uparrow_g}$ (c)$P_{\downarrow\uparrow\uparrow_g}$

(d)$P_{\uparrow\uparrow\downarrow_e}$ (e)$P_{\uparrow\downarrow\uparrow_e}$ (f)$P_{\downarrow\uparrow\uparrow_e}$

Fig. 7.10: Readout process considering spontaneous decay when we tune the laser to get a resonance between $|\uparrow\uparrow\downarrow\rangle^g$ and $|\uparrow\uparrow\downarrow\rangle^e$. Here $V = 0.0000002 \ll \gamma$. The related populations of several spin states are plotted as a function of time. (a)P_1: the population of $|\uparrow\uparrow\downarrow\rangle^g$; (b)$P_2$: the population of $|\uparrow\downarrow\uparrow\rangle^g$; (c)$P_3$: the population of $|\downarrow\uparrow\uparrow\rangle^g$, and (d)$P_4$: the population of $|\uparrow\uparrow\downarrow\rangle^e$; (e)$P_5$: the population of $|\uparrow\downarrow\uparrow\rangle^e$; (f)$P_6$: the population of $|\downarrow\uparrow\uparrow\rangle^e$.

Our conclusions are as follows,

- The readout method I is the best method because $|\uparrow\uparrow\uparrow\rangle$ is not coupled with any other spin states if we only consider a Heisenberg spin Hamiltonian.

- Several interesting phenomena occur in readout method II because there are exchange couplings between different states within the spin subspace with total $S_z = 1/2$. These exchange couplings disturb the readout process, as can be seen from our density matrix calculation and our time-dependent perturbation theory calculation.

- If we introduce a spontaneous decay rate γ, and if γ is much smaller than the oscillation driving strength V, we can observe lightly damped Rabi oscillations in favourable circumstances, leading to significant population of the excited states. On the other hand, if γ is much larger than V, we cannot see Rabi oscillations and observe only decay of the excited-state population at a rate γ.

- In addition to our calculations, a very important parameter in the problem is the linewidth of the laser, i.e., how accurate the equals sign in the equation 7.16 should be in order to attain resonance. This determines the total number

of scattered photons.

Part II

EXCHANGE CALCULATION IN METAL-PHTHALOCYANINE DIMER

8. INTRODUCTION TO PORPHYRIN AND PHTHALOCYANINE

8.1 The potential of organic systems for quantum information processing

The second part of this thesis deals with a completely different class of material: porphyrins and other closely related tetrapyrrolic pigments. These are very different from the conventional semiconductors of the first part. Why are they an interesting alternative for quantum information processing?

Porphyrins have a relatively complex molecular structure, but combine this with good optical properties and the ability to bind divalent metal atoms. Recalling the control-qubit system outlined in Chapter 1, we know that the nature and properties of the control species are critically important for the ability to compute and read out within our scheme. An ideal control should have a very long excited-state lifetime and create well-defined exchange interactions between specific qubits in order to implement quantum gate operations. Porphyrins have an extremely long excited-state lifetime owing to their conjugated molecular structure. In addition, since they can bind specific transition-metal atoms having spin degrees of freedom, there is a natural association of a "control" system with a single qubit. This association can be extended to multiple qubits by engineering porphyrin derivatives in which multiple metals are coordinated by a common ring system. Finally, as will be shown by the experiments and theory reported here, the combination of chemical control (through synthesis) and physical control (through film deposition) enables one to specify the environment of a given control-qubit system more closely than is possible using the alloy disorder of an inorganic semiconductor.

Taken together, these factors make porphyrins very promising candidates for the implementation of qubits and the storage of quantum information via their metal electron spins. This is the motivation for the research reported here, devoted to the exchange interactions between metal-porphyrin molecules, and their role in controlling the magnetic properties.

8.2 The nature of porphyrin-like organic systems

The tetrapyrrolic pigments occur widely in nature, and they play very important roles in various biological processes. For example, Heme [the iron(II) protoporphyrin-IX complex] as shown in Figure 8.1 is the prosthetic group in hemoglobin and myoglobin, which are responsible for oxygen transport and storage in living tissues. Chlorophyll (see Figure 8.1), another kind of porphyrin-like organic system containing magnesium, plays a very important role in photosynthesis. There are several different kinds of Heme and chlorophyll; in Figure 8.1, we show the most common ones: Heme-B and chlorophyll-C.

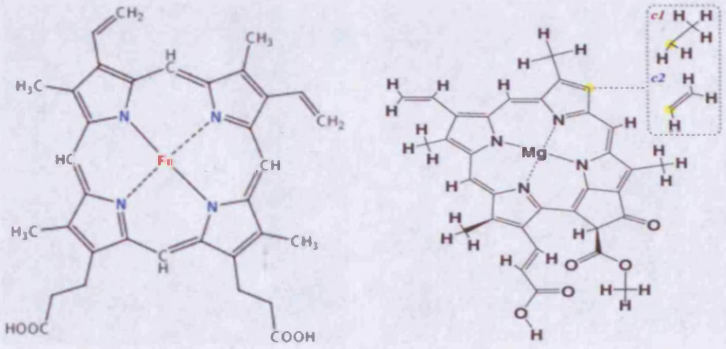

Fig. 8.1: Molecular structure diagram of Heme-B and chlorophyll-C.

The word porphyrin has its origins in the classical world of ancient Greece. In those days, the Greek word *porphura* was used to describe the color purple. This immediately tells us something about one of the most important features of porphyrin(P): their intense purple color. Porphyrins were originally used as purple pigments.

A more detailed definition is [57] "porphyrins are a large class of deeply colored red or purple, fluorescent crystalline pigments, of natural or synthetic origin, having in common a substituted aromatic macrocyclic ring consisting of four pyrrole-type residues, linked together by four methine bridging groups." (See Figure 8.2). Pyrrole itself is a five-membered ring of four carbon atoms and one nitrogen atom. To each of the atoms in this ring a hydrogen atom is also bound. The most interesting thing about porphyrins is that even a very small variation on the basic structural theme of a tetrapyrrolic macrocycle will lead to a wide diversity of biochemical functions. For example, one metal 2^+ ion can be fitted in the center of porphyrins. Four benzenes and four nitrogen atoms can substitute particular C and H atoms on the macrocyclic ring in porphyrin, so we can have metal-free phthalocyanine(Pc) as

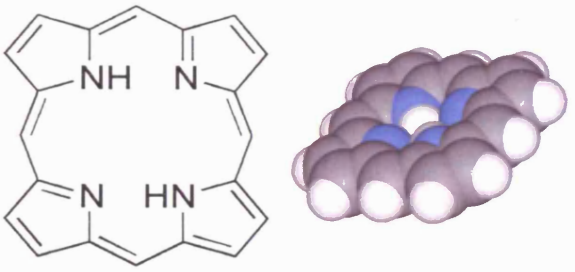

Fig. 8.2: 2D and 3D molecular structure diagrams of porphyrins.

shown in Figure 8.3. We can also obtain a metal phthalocyanine by fitting a metal ion in the center of Pc. (See Figure 8.3). Of particular interest for our work are the transition metal phthalocyanines Cu(II)Pc and Mn(II)Pc; these have several phases [66] including the α phase, most often found in thin films, in which the stacking angle is 65°, and the β phase, most often found in powders, in which the stacking angle is 45°. The main function of porphyrins and porphyrin-like compounds in nature

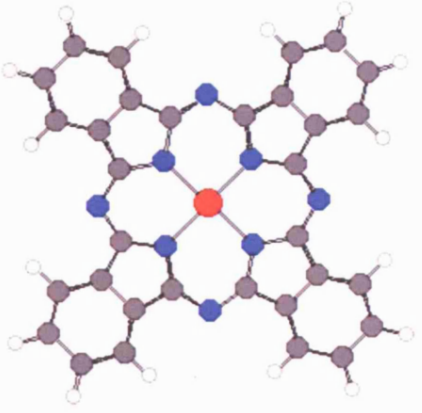

Fig. 8.3: Molecular structure of metal-Phthalocyanine. Red solid circle: metal ion; blue solid circle: Nitrogen atom; grey solid circle: Carbon atom; hollow circle: Hydrogen atom.

is to bind metal atoms, which act as centers for significant biochemical events. For example, protoporphyrin IX in heme complexes iron which, in hemoglobin and myoglobin, reversibly binds oxygen so that it can be transported around the body (hemoglobin) or stored in muscle tissue (myoglobin).

Another important biochemical event indirectly involving porphyrin-like compounds is photosynthesis. Without photosynthesis, there could be no life: not only does photosynthesis provide the oxygen we breathe, it also gives us most of the energy driving living things. Photosynthesis does this by trapping energy in sun-

light and uses it to convert carbon dioxide and water into carbohydrates. Plants use carbohydrates in their own metabolism, and the animals eat the plants in their metabolism, too. The key molecule for the early stages of photosynthesis is chlorophyll, which involves a Mg^{2+} ion trapped by a porphyrin-like structure. Here, the function of the macrocycle is to capture photons of light in the near-ultraviolet (400 nm) and red (650 – 700 nm) regions of the visible spectrum. The function of the metal is also to modulate the light-absorbing and energy-transfer properties of the chlorophyll and bind water which provides electrons for photosynthetic process. In the reduced porphyrin macrocycle of chlorophyll, the conjugated system of double bonds is ideally suited to this task, while the substituents around the macrocycle serve to fine-tune its light-absorption characteristics.

8.3 Electronic structure and optical properties of porphyrin-like organic systems

In the last section we saw that the porphyrin-like organic system, chlorophyll plays an important role in photosynthesis, so it is necessary to understand the optical properties of porphyrin-like systems. Indeed, although the main concern of this thesis is not optical properties but magnetism, optical properties are an aspect we should look into. Before we introduce optical properties of a porphyrin-like system, we should have some knowledge about its electronic structure because the electronic structure determines optical properties directly.

8.3.1 Electronic structure of porphyrin-like organic system

In this section our main concern is the electronic structure of metalloporphyrin. There are two types of metalloporphyrins: regular metalloporphyrins which contain regular metal, i.e., closed-shell metal; irregular metalloporphyrins which contain irregular metal, i.e., partly-filled-shell metal. We first introduce two simple models: Circular box model and PPP model (§8.3.1.A) for the electronic structure of regular metalloporphyrins. Then we will introduce the electronic structure calculation of Cu(II)Pc (§8.3.1.B) and Mn(II)Pc (§8.3.1.C) both of which contain irregular metals.

A. A simple model for electronic structure for regular metalloporphyrins

The simplest useful theory [58, 59] treats the 16-member ring with 18 electrons as a circular free-electron wire. One-electron orbitals of the form $\exp(i\mu\phi)$ will have energy $\hbar^2\mu^2/2mR^2$, where m is the electron mass, R is the ring radius, and μ is an integer quantum number. In the ground state, a simple one-electron picture

predicts that orbitals with $\mu = 0, \pm1, \pm2, \pm3, \pm4$ are occupied. The lowest-energy excited states then arise from four transitions $\mu = \pm4 \rightarrow \nu = \pm5$, which give the system a total angular momentum $L_z = \pm1$ or ±9. Each transition gives one singlet state with $S = 0$, and a triplet of states with $S = 1$. According to Hund's rules, the lowest-energy excited state should be a triplet, and the singlets with $L_z = \pm1$ should have a higher energy than $L_z = \pm9$ (see Figure 8.4). Since the ground state has $L_z = 0$, the normal selection rule $\delta L_z = \pm1$ for electric dipole transitions means that such transitions are allowed to the higher singlet, but forbidden to the lower one, in a one-electron picture. As we shall see in §8.3.2, both sets of transitions are in fact associated with optical absorptions: the high-energy 'B band' with the $L_z = \pm1$ singlet, and the lower-energy 'Q band' with the $L_z = \pm9$ singlet. In this picture the Q-band transitions are made 'quasi-allowed' by Coulomb interactions between electrons (not included in the simple one-electron picture) which mix the $L_z = \pm1$ and $L_z = \pm9$ states.

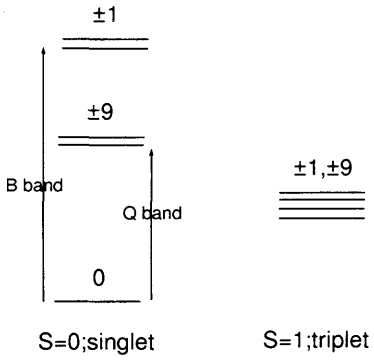

Fig. 8.4: An energy level diagram for circular box model associated with absorption spectra is shown.

A slightly more accurate model is Pariser-Parr-Pople (PPP) theory [60]; the essence of this method is to separate the loosely bound π electrons from the remaining 'core' and to treat electron interaction among the π electrons explicitly. The one-electron energy levels can be calculated by a self-consistent field procedure. For the tetraaza-porphyrin the positions of the one-electron levels associated with the ring are shown in Figure 8.5; other porphyrin-like organic systems have similar state alignment. The highest filled states have a_{1u}, a_{2u} symmetry and correspond to the $\mu = \pm4$ states of the free-electron model split in the D_{4h} environment, while the lowest empty (LUMO) states have e_g symmetry and correspond to the $\mu = \pm5$ orbitals. Coulomb interactions between electrons will cause the singlet transitions

including $a_{1u} \rightarrow e_{gx}, a_{2u} \rightarrow e_{gx}, a_{1u} \rightarrow e_{gy}$, and $a_{2u} \rightarrow e_{gy}$ to mix. The B band and Q band are then understood as mixtures of these single transitions, as described above.

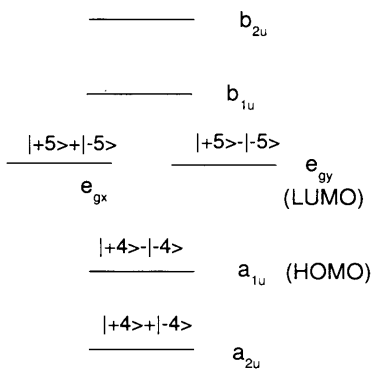

Fig. 8.5: A ring state energy level diagram of tetraaza-porphyrin for PPP model

B. Previous electronic structure calculations of Cu(II)Pc

In order to understand the electronic structure of metal-Pc systems, we need to understand how metal-derived orbitals are introduced into these schemes. This is most simply done within the Iterative Extended Hückel (IEH) model, which seeks to solve the Schrödinger equation with an effective potential using a self-consistent charge procedure for all the valence electrons of the molecule [61]. Figure 8.6, shows the resulting alignments of metal electron states and ring states.

CuPc molecule has D_{4h} symmetry, which possesses eight irreducible representations: a_{1g} ,a_{1u}, b_{1g}, b_{1u}, a_{2g}, a_{2u}, b_{2g}, b_{2u}, e_g, and e_u. A schematic of the highest occupied and lowest empty levels is shown in Figure 8.6: of the five spatial states ($a_{1g}(d_{z^2})$, $b_{2g}(d_{xy})$, $2 \times e_g$ (d_{xz} and d_{yz}), b_{1g} ($d_{x^2-y^2}$)) produced by the splitting of the Cu d-states in the D_{4h} environment, only the b_{1g} state is singly occupied (lying within the HOMO-LUMO gap of the molecule), while all the others are filled (in the IEH model, lying below the a_{1u} and a_{2u} states of the ring system). The symmetry of the overall many-electron state within the IEH model is $^2B_{1g}$ [61], where the superscript '2' refers to spin multiplicity.

C. Previous electronic structure calculations of Mn(II)Pc

The electronic structure and magnetism of Mn(II)Pc has been studied extensively [65, 66]. The molecular structure of Mn(II)Pc is shown in Figure 8.3.

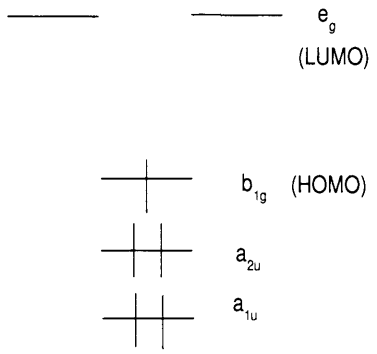

Fig. 8.6: The electronic structure of Cu(II)Pc calculated by Zerner and Gouterman within IEH model [61];a_{1u}, a_{2u}, e_g are π electron states. b_{1g} is metal electron state.

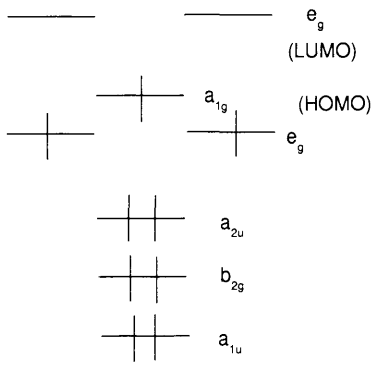

Fig. 8.7: The electronic structure of Mn(II)Pc calculated by Zerner and Gouterman within IEH model [61].

The electronic structure of MnPc is more complicated than that of CuPc. The Mn^{2+} ion possesses a total of five 3d valence electrons. In the free ion, Hund's rules result in a high-spin state with $S = 5/2$ and all five d-levels singly occupied; however, from measurements of the saturation magnetic moments [65], it is known that only three electrons are unpaired in MnPc and form an $S = 3/2$ state. This results from the working of the Coulomb interaction in the D_{4h} symmetry of the complexed ion: in the most common picture, the d states split to form b_{1g}, a_{1g}, e_g, and b_{2g} states (going from high energy to low energy). Of these, the low-energy b_{2g} state is completely filled, and the high-energy b_{1g} state empty. The remaining three orbitals (one a_{1g}, two e_g) are singly occupied; the Coulomb interaction then favours the alignment of these three spins, so their spin state is fully symmetric, and their spatial state antisymmetric. Meanwhile, the LUMO (lowest unoccupied molecular orbital) of the Pc ring has e_g symmetry (See Figure 8.7). The overall symmetry of the resulting state is $^4A_{2g}$ [65].

This picture of the electronic structure is not the only one. Liao *et. al* [62] used DFT methods and found an electronic configuration in which the three unpaired electrons occupy the a_{1g}, b_{2g}, and one e_g state while the other e_g state is doubly occupied, to give an overall symmetry ^4E_g. This calculation is in agreement with the more recent magnetic circular dichroism (MCD) and UV-vis measurements [63] of the molecule in an argon matrix but different from the early magnetic measurements of solid MnPc. It is possible that the ^4E_g configuration may be favoured in the isolated molecule or in the argon matrix, with the $^4A_{2g}$ state favoured in the bulk material.

8.3.2 Optical properties of porphyrin-like organic system

In this section we first describe the absorption and emission spectra of regular metalloporphyrin in §8.3.2.A, then optical properties of irregular metalloporphyrin in §8.3.2.B, and at the end we present a summary of optical properties of metalloporphyrin.

A. Absorption and emission spectra of regular metalloporphyrin

All the regular metalloporphyrins share the following general features in their absorption spectra [56]:

- Q bands: Two visible bands are seen between 500 and 600 nm, which are separated by about 1250 cm^{-1}. The lower-energy band is due to the pure electronic transition to the lowest singlet excited state, meanwhile the higher-

energy one includes one mode of vibrational excitation. The origin of Q bands can be quite well explained by the simple theory that treats metal porphyrin as a free electron wire ring (see §8.3.1). According to this simple theory the origin of Q bands is identified as the excitation from the singlet ground state to the lowest singlet excited state which, although it consists primarily of states with $L_z = \pm 9$, nonetheless has a non-zero admixture of $L_z = \pm 1$ states due to the coulomb interaction.

- B bands: An exceedingly intense band appears between 380 and 420 nm. The origin of B bands is identified as the excitation from the ground state to the higher ($L_z = \pm 1$)singlet excited state, which is allowed by selection rule even in the absence of mixing by the Coulomb interaction.

- N,L,M bands: These bands appear at still higher energies, but are weaker than Q and B bands.

The emission spectrum is also closely related to the energy level alignment. Figure 8.8 [56] shows an energy level diagram applicable to describe the emission from porphyrin-like molecule with singlet ground states. The energy level alignment in Figure 8.8 is basically the same as that in Figure 8.4 in which singlet state is the ground state and the lowest excited state is a triplet. Excitation from the ground state S_0 to any singlet excited states S_x induces a very fast radiationless decay to the lowest excited singlet S_1. From S_1 the molecule can emit fluorescence radiation $S_1 \rightarrow S_0$ with rate k_f, can decay non-radiatively $S_1 \rightarrow S_0$ with rate k_1, or can transfer to the lowest triplet $S_1 \rightarrow T_1$ with rate k_2. If the system is in the lowest triplet T_1, from T_1 the molecule can emit phosphorescence radiation $T_1 \rightarrow S_0$ with rate k_p, radiationless decay $T_1 \rightarrow S_0$ with rate k_3, or can be reexcited to S_1 with rate k_{-2}, and such repopulation of S_1 can lead to delayed fluorescence.

The spectra, lifetimes, and quantum yields can be observed for fluorescence and phosphorescence. Quantum yields Φ refer to the ratio of photons in to photons out. The spectra of delayed fluorescence are the same as the fluorescence one, but have different lifetimes and quantum yields.

B. Absorption and emission spectra of irregular metalloporphyrins

In the above context, we discussed the optical properties of regular metalloporphyrin. For irregular metalloporphyrin the emission spectrum is different from the normal spectrum of the regular metalloporphyrin, and the absorption spectrum is also different in most cases.

There are two types of irregular absorption spectra:

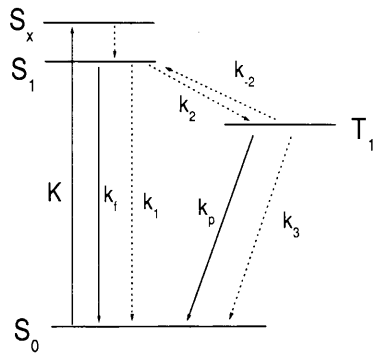

Fig. 8.8: An energy level diagram applicable to describe the emission from regular porphyrin molecule with singlet ground states.

- *Hypso* absorption spectra are similar to normal absorption spectra, but blue shift. Transition metal porphyrins of Group VIII and IB with metal configuration d^{6-9} show this kind of spectrum. The reason for the blue shift is that the mixture of the empty $e_g(\pi^*)$ and filled $d\pi$ raises the energy of $e_g(\pi^*)$, and hence the energy gap between $e_g(\pi^*)$ and top filled states $a_{2u}(\pi), a_{1u}(\pi)$.

- *Hyper* absorption spectra show significant extra bands additional to Q, B, and N. The reason for this is that there are extra metal orbitals from which electronic transitions can be made.

For the emission spectra of irregular porphyrin, we have three types:

- *Phosphorescent* metalloporphyrins show very weak fluorescence, $\Phi_f < 10^{-3}$, even in many cases no fluorescence can be observed. Meanwhile the phosphorescence varies in a wide range of $(10^{-4}, 1)$.

- *Luminescent* ones contain paramagnetic metals. In this case there is no singlet or triplet, so we can not characterize the emission as fluorescence or phosphorescence. The emission yields are larger than 10^{-4}.

- *Non-radiative* ones show very weak emission.

The optical properties of our concerned metal-Pc are similar to metalloporphyrins, but in the emission spectra no fluorescence was observed. Recently, Kumar *et al.* [64] studied the optical absorption and emission spectra of various metal-Pcs including ZnPc, MnPc, and CuPc, etc in dimethyl formamide solvent. In their work

Q band and B band are identified, but the emission spectra are poor due to the non-radiative collisional relaxation process in solvent media.

So far we have introduced the absorption and emission spectra of regular and irregular porphyrins. Table 8.1 below summarizes the porphyrin spectra. Here

Emission\Absorption	Normal	Hypso	Hyper	Definition
Fluorescent	Regular	–	–	$\Phi_f > 10^{-3}; \Phi_{em} > 10^{-3}$
Phosphorescent	–	Irregular	Irregular	$\Phi_f < 10^{-3}; \Phi_p > 10^{-4}$
Luminescent	Irregular	Irregular	Irregular	$\Phi_{em} > 10^{-4}$
Radiationless	Irregular	Irregular	Irregular	$\Phi_{em} < 10^{-4}$

Tab. 8.1: Absorption and emission spectra of regular and irregular porphyrins. Φ_f refers to quantum yield of fluorescence. Φ_{em} refers to total emission.

normal absorption means that for $\lambda > 320$nm there are only (π, π^*) bands, Q, B, N,L, and $\lambda(Q) > 570$nm. The difference between normal and hypso absorptions is $\lambda(Q) < 570$nm in hypso absorption. Whereas hyper absorption does not originate from (π, π^*) transitions.

9. MAGNETISM IN THE METAL-PC ORGANIC SYSTEM: A PERTURBATION APPROACH

9.1 Experimental studies of magnetism in CuPc and MnPc

The magnetism of metal-Pc was extensively studied by Barraclough and Yamada [65, 66]. In 1998, Yamada [66] performed magnetic measurements on both a β-Mn(II)Pc crystal (stacking angle 45°) and Mn(II)Pc thin film (stacking angle 65°). They found that the β phase shows a ferromagnetic interaction, while the thin-film α phase is antiferromagnetic. They explained their findings in terms of superexchange pathways operating through nitrogen-nitrogen intermolecular contacts.

Recently Heutz [67] *et al.* have performed further magnetic measurements on CuPc and MnPc. The results are shown in the following tables. As shown in Table 9.1 and Table 9.2, the MnPc powder presents strong ferromagnetism, while in the MnPc film a weak anti-ferromagnetism appears; the CuPc powder has very weak ferromagnetism, but the CuPc film is strongly anti-ferromagnetic.

Note that the magnetic properties are determined by the structure (α versus β), not by the sample morphology (powder versus thin film). The results confirm the previously measured difference between the α and β phases of MnPc, and also show that a corresponding difference exists for CuPc, although in this case the β phase is paramagnetic, rather than ferromagnetic. We can describe such magnetic systems in terms of an effective magnetic moment $\vec{S}_i$ associated with each center i (corresponding to one molecule in this case). The simplest form for the coupling between magnetic moments i, j is the well-known Heisenberg Hamiltonian $J_{ij}\vec{S}_i \cdot \vec{S}_j$ where J_{ij} is called the exchange constant. We would like to gain both a quantitative understanding of the magnitudes of the exchange constants in Mn(II)Pc and Cu(II)Pc, and a picture of the physics driving their dependence on the crystal

Sample(phase)	MnPc powder (β)	MnPc film(α)
$\theta_p(K)$	11.45	-1.61
$J_x(K)$	-	-

Tab. 9.1: Magnetic properties of the MnPc samples measured by Heutz *et al.*.

Sample(phase)	CuPc powder (β)	CuPc film(α)	CuPc film (β)	Templated film(α)
$\theta_p(K)$	0	-1.79	0	-2
$J_{ex}(K)$	-0.05	1.45	0	1.6

Tab. 9.2: Magnetic properties of the CuPc samples measured by Heutz *et al.*.

structure; our aim in this chapter is to gain a microscopic understanding of these structure-dependent magnetic properties.

9.2 DFT calculations of metal-Pc molecules

First we need to understand the nature of the one-electron states in the molecules. We used the Gaussian 98 code [68] to perform a DFT calculation on single isolated metal-Pc molecules. We selected the B3LYP [69] exchange-correlation functional, of which we give further details in Chapter 10. In the present calculation we use the Kohn-Sham states emerging from the calculation as a basis to perform a perturbative calculation of the exchange constants. The basis set is 6-31G [70], consisting of six independent Gaussian functions for the core electron atomic orbitals, three Gaussian functions for the inner part of the valence shell, and one Gaussian function for the outer part.

9.2.1 Cu(II)Pc

According to our Gaussian DFT calculation the electronic structure of Cu(II)Pc is $^2B_{1g}$, but the energy level order is slightly different from that found in the early extended Hückel calculations by Gouterman *et al.* [61]. Our level scheme is shown in Figure 9.1; the slight differences in energy-level ordering are not, however, expected to have a major effect on the forms of the states themselves. An important check that our results are reasonable is the distribution of charge between the metal atom and the Pc ring. We therefore calculated the Mulliken charge on the Cu atom in each state; the results are shown in Figure 9.1.

We first introduce the definition of the Mulliken charge. The normalization condition for a one-electron molecular orbital $\psi_i(\vec{r})$ reads

$$1 = \int d\vec{r}\psi_i^*(\vec{r})\psi_i(\vec{r}) = \sum_{\nu,\mu=1}^{K} C_{\nu i}^* C_{\mu i} \int d\vec{r} b_\nu^*(\vec{r}) b_\mu^*(\vec{r}) \tag{9.1}$$

$$= \sum_{\nu,\mu=1}^{K} C_{\nu i}^* C_{\mu i} S_{\nu\mu} \tag{9.2}$$

$$= \sum_{\nu,\mu=1}^{K} P_{\mu\nu}^{(i)} S_{\nu\mu} \tag{9.3}$$

$$= \mathrm{tr}[P^{(i)}S], \tag{9.4}$$

where $b_\nu(\vec{r})$ are the atomic basis functions, $C_{\nu i}$ are the expansion coefficients of molecular orbital i in this atomic basis, and $P^{(i)}$ is the bond-order matrix corresponding to molecular orbital i. The complete bond-order matrix (or one-electron density matrix) is then $P = \sum_i f_i P^{(i)}$, where f_i is the occupancy of state i. The Mulliken charge contribution from orbital i is then defined as the *partial* trace of $P^{(i)}S$

$$\rho_M(A)^i = \sum_{\mu \in A} (P^{(i)}S)_{\mu\mu}, \tag{9.5}$$

where the sum is restricted just to basis functions that are centered on atom A. This definition is only meaningful if the basis set consists of basis functions that can each be unambiguously associated with an atomic site. The total Mulliken charge is $\rho_M(A) = Z_A - \sum_i f_i \rho_M(A)^i$, where Z_A is the atomic number of atom A.

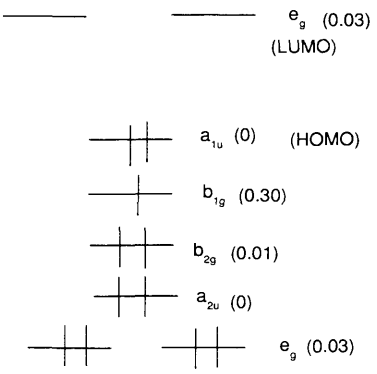

Fig. 9.1: Our Gaussian calculation of the electronic structure of Cu(II)Pc. The contribution to the Mulliken charge on Cu atom is shown in brackets.

From the Mulliken population analysis we can identify b_{1g} as a metal d-orbital which is hybridized with the Pc ring (Mulliken charge 0.30 is of order 1, but less than 1). The total Mulliken charge on copper is +0.97; this is positive, as expected, but less than the nominal valence of +2 because of hybridization with the ring. The total Mulliken spin density on the copper atom (defined analogously to the charge density, but counting up-spin states as positive and down-spin as negative) is 0.68; this is consistent with the existence of one singly-occupied orbital, with a spin mainly but not entirely localized on the copper atom. The eigenvalues of states near the Fermi energy are shown in Table 9.3.

State symmetry	Eigenvalue(Hartree)	Mulliken charge on Cu
e_g(LUMO)	−0.1025	0.03
a_{1u}(HOMO)	−0.1876	0
b_{1g}	−0.2404	0.3
b_{2g}	−0.2516	0.01
a_{2u}	−0.2525	0
e_g	−0.2536	0.03

Tab. 9.3: The symmetries, energy level alignments, and Mulliken charges on Cu of Cu(II)Pc DFT calculation using Gaussian code corresponding to Figure 9.1.

State symmetry	Eigenvalue(Hartree)	Mulliken charge on Mn
e_g(LUMO)	−0.0980	0.03
a_{1u}(HOMO)	−0.1880	0
b_{2g}	−0.2222	0.72
e_g	−0.2353	0.39
a_{2u}	−0.2490	0
a_{1g}	−0.2535	0.80

Tab. 9.4: The symmetries, energy level alignments, and Mulliken charges on Mn of Mn(II)Pc DFT calculation using Gaussian code corresponding to Figure 9.2.

We found that the occupied molecular orbital with the largest Kohn-Sham eigenvalue is not the singly-occupied b_{1g} state, but the a_{1u} state (which, as described in §8.3.1, is derived from the Pc ring and cannot hybridize with the metal d-states). This highlights the importance of two-electron Coulomb terms in determining the configuration: doubly occupying the b_{1g} state would incur a large Coulomb penalty because the charges would spend much of their time localized in the Cu 3d states, whereas the double-occupancy penalty for the more diffuse a_{1u} state is much smaller.

9.2.2 Mn(II)Pc

For MnPc, our Gaussian calculation gave the overall electronic configuration $^4A_{1g}$, with three singly-occupied one-electron levels having a_{1g} and e_g (twice) symmetry. The total Mulliken charge on Mn is +1.14; again this is of the same order, but somewhat less than, the nominal +2 valence. The Mulliken spin density on Mn is +3.1. The eigenvalues and symmetries of the states near the Fermi energy are shown in Table 9.4.

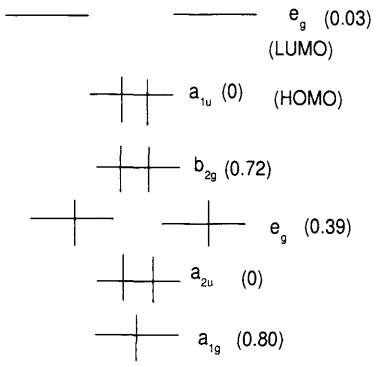

Fig. 9.2: Our Gaussian calculation of the electronic structure of Mn(II)Pc. The contribution to the Mulliken charge on the Mn atom is shown in brackets.

9.3 Exchange interactions

In order to introduce our nomenclature for the various processes contributing to the exchange interactions between spins, we follow the arguments of Anderson [71]. His original paper considered interactions between magnetic ions in ionic crystals such as MnO and MnF_2, but very similar arguments apply in the case of the organic compounds studied here.

9.3.1 Direct exchange

The direct exchange interaction originates from a quantum exchange term of the Coulomb interaction between d electrons on neighbouring ions. [71]

$$J_{direct} = -2\langle n_1(1)n_2(2)|\frac{e^2}{r_{12}}|n_1(2)n_2(1)\rangle, \tag{9.6}$$

where n_1, n_2 are the orthogonal localized d electron orbitals on sites $1, 2$. We can see that such a direct exchange interaction always gives rise to ferromagnetic interactions, because the expectation value can be written as the classical electrostatic self-energy of the 'exchange charge' distribution $n_1 n_2$. We should also notice that the above formula is true only if the orbitals are orthogonal.

9.3.2 Super exchange

The direct exchange interaction was calculated as the expectation value of the Coulomb interaction in the ground state of the localized electron system, but spin-spin interactions can also arise from the terms in the Hamiltonian that tend to *delocalize* the electrons, treated to second order in perturbation theory.

To see how this works, consider a localized d-electron system, in which the on-site Coulomb interaction U is large compared to the transfer matrix element between electrons at neighbouring sites. The system then becomes a Mott insulator: the on-site Coulomb interaction hinders the motion of d-electrons in the crystal and keeps them localized. The perturbation expansion must be carried out around this insulating reference state; therefore, the on-site Coulomb interaction U is included in the unperturbed Hamiltonian and the transfer matrix elements $b_{n-n'}$ are treated as a perturbation.

In the perturbation expansion for the energy, the first-order term (the expectation value of the transfer matrix elements) is zero because all electrons are localised to a single site; the second-order term is given by the process where an electron at ion n transfers to a neighbouring ion n' and after that one of the two electrons at n' returns to the original ion n. By this process electrons at n and at n' exchange positions with each other. However, only when the spins at n and n' are antiparallel to each other is this process possible; this generates a contribution to the exchange interaction at second order, which can be written as

$$J_{super} = 2\frac{|b_{n-n'}|^2}{U}. \tag{9.7}$$

If we go on to consider the third-order terms in $b_{n-n'}$, we obtain the third-order contribution to super-exchange, and so on. This is especially important when the magnetic atoms are separated by non-magnetic species, for example inorganic anions or organic ligands. It is then necessary to take the hopping perturbation to higher order in order to reach an excited state in which an electron is transferred onto a neighbouring magnetic site. Note also that the superexchange may vanish, because the transfer matrix elements depend not only on the distance between magnetic ions n and n', but also on the symmetry of the orbitals. So the superexchange interaction depends on the relative positions of magnetic ions and the non-magnetic species. In fact, we have already introduced this kind of interaction in Chapter 4, where we use it to understand the physical origin of ferromagnetic interactions in the control-qubit system.

9.3.3 Indirect exchange

The indirect exchange interaction between electronic spins is similar to the indirect exchange interaction between nuclear spins. The indirect exchange scheme was first invented by Ruderman and Kittel [72], and independently, by Bloembergen and Rowland [73] in molecular physics; these authors studied the effective long-range interaction between nuclear spins due to the hyperfine coupling with the common

sea of conduction electrons [72] or common valence electrons [73]. Briefly, a magnetic atom polarizes the spins of the conduction electrons in its neighbourhood; the resultant spin polarization is not well localized in the vicinity of the atom, but delocalizes. In the case of a metal, the induced spin density is oscillatory and long-ranged. A second magnetic atom experiences an interaction with this induced spin polarization; it may be ferromagnetic or anti-ferromagnetic. The net result is an indirect exchange interaction with the first magnetic atom

$$J_{indirect} = \frac{J^2 t}{\text{energy penalty}}, \tag{9.8}$$

where J is the interaction of each magnetic atom with the spin polarization, t is the transfer matrix element for the spin polarization from one site to another, and the energy penalty is the energy involved in creating the spin polarization. Later, we will introduce operators to describe this process more formally in metal phthalocyanines.

9.4 Super-exchange calculation

We aim to understand the mechanism of exchange couplings between neighbouring MnPc and CuPc molecules observed in experiments [66, 67]. We first consider the super-exchange contributions.

9.4.1 CuPc

As explained in §9.3.2, the super-exchange contribution generally dominates when considering the interaction between localized spins in insulating materials. However, CuPc is an example of a situation where this interaction is expected to be negligible. This is because the unpaired spin is located in a b_{1g} orbital, but there is no low-energy state of the same symmetry in the ligand available to hybridize with it. Therefore, as long as the symmetry of the molecule remains D_{4h} (believed to be an excellent approximation even in the crystal) the spin-carrying electron is 'tied' to the Cu site and no super-exchange can take place except by direct hopping from the Cu orbitals to the neighbouring molecule.

9.4.2 MnPc calculation

In the case of MnPc, the individual molecular spins have $S = 3/2$, so the total spin of a pair of MnPc molecules A and B could be $0, 1, 2, 3$. We therefore need, in principle, three independent parameters in the spin Hamiltonian to characterize fully the relative energies of these states. If we neglect spin-orbit coupling, the Hamiltonian

must be invariant under simultaneous rotations of both spins and therefore must have the form

$$\hat{H} = J_1(\vec{S}_A \cdot \vec{S}_B) + J_2(\vec{S}_A \cdot \vec{S}_B)^2 + J_3(\vec{S}_A \cdot \vec{S}_B)^3, \tag{9.9}$$

where J_1, J_2, J_3 are exchange couplings. We can find all three parameters from the 4×4 matrix spanned by the states with $M_S = 0$: $|(3/2)_A, (-3/2)_B\rangle$, $|(1/2)_A, (-1/2)_B\rangle$, $|(-1/2)_A, (1/2)_B\rangle$, and $|(-3/2)_A, (3/2)_B\rangle$. Our strategy will be to construct this part of the spin Hamiltonian by perturbation theory. For the moment we concentrate on superexchange interactions as defined above; in other words, we include only intermediate states where

- one electron is transferred between adjacent Mn ions via the ligand e_g state;
- no direct electron transfer between Mn ions is possible.

These requirements lead us to consider the following three kinds of typical configuration as shown in Figure 9.3. In the third configuration (Figure 9.3(3)) one

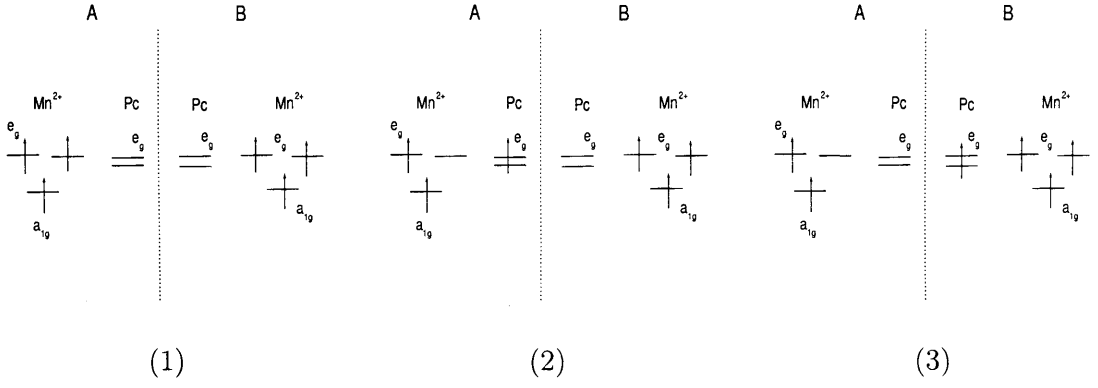

Fig. 9.3: Three types of typical singlet-electron configurations are shown. (1) is the ground state in which no electron is hopping; (2) is an intra-molecule transfer from Mn e_g state (although this can be Mn a_{1g} state) to ligand e_g state; (3) is an inter-molecule transfer from Mn e_g state to the ligand e_g state of the neighbouring molecule.

electron is transferred from the A molecule to the B molecule, where it can interact with Mn spin: it is through this interaction that the spin projections m_A and m_B associated with the two molecules can change, thereby coupling the four spin states: $|(3/2)_A, (-3/2)_B\rangle$, $|(1/2)_A, (-1/2)_B\rangle$, $|(-1/2)_A, (1/2)_B\rangle$, and $|(-3/2)_A, (3/2)_B\rangle$. We assume that the interaction between a spin-1/2 in the ligand e_g state and a spin-3/2 localised on the Mn is of the form

$$\hat{H}_p = K\vec{s} \cdot \vec{S}, \tag{9.10}$$

where the spin quantum numbers are $s = 1/2$ and $S = 3/2$. The perturbation to the Hamiltonian consists of two parts: one is the matrix representation of Hamiltonian in the equation 9.10:

$$\hat{H}_p = \begin{array}{c} \\ |(3/2)_A,(-3/2)_B\rangle \\ |(1/2)_A,(-1/2)_B\rangle \\ |(-1/2)_A,(1/2)_B\rangle \\ |(-3/2)_A,(3/2)_B\rangle \end{array} \begin{array}{c} \begin{array}{cccc} |(3/2)_A,(-3/2)_B\rangle & |(1/2)_A,(-1/2)_B\rangle & |(-1/2)_A,(1/2)_B\rangle & |(-3/2)_A,(3/2)_B\rangle \end{array} \\ \begin{pmatrix} -3/4K & 1/2K & 0 & 0 \\ 1/2K & -1/12K & 2/3K & 0 \\ 0 & 2/3K & -1/12K & 1/2K \\ 0 & 0 & 1/2K & -3/4K \end{pmatrix} \end{array}. \quad (9.11)$$

The other part consists of hopping terms which can move the system between the three types of configuration shown in Figure 9.3. Note that in D_{4h} symmetry, the e_g states of Mn can hybridize effectively with the e_g states of the ring, thereby enabling the system to make transitions between configurations of types (1) and (2); the existence of unpaired spins in the e_g states is what makes super-exchange processes much more important in the case of MnPc.

There are 25 spatial configurations like typical types (1), (2) and (3) shown in Figure 9.3 and each has four possible spin states, giving a total of 100 states. We construct the 100 × 100 Hamiltonian matrix, and extract the effective Hamiltonian within the 4 × 4 low-energy subspace by the same method used in §4.4. We find that it can be written in the form (9.9), with parameters

$$\begin{aligned} J_1 &= \frac{4}{3}K[\frac{t_{pmg}^2}{(-E_g+2u_{gx}-3v_{pmn})^2}+\frac{t_{pmx1}^2}{(e_g-E_g+u_{gx}+u_{xx}-3v_{pmn})^2} \\ &\quad +\frac{t_{pmx2}^2}{(e_g-E_g+u_{gx}+u_{xx}-3v_{pmn})^2}]+O(t^3); \qquad (9.12) \\ J_2 &= \frac{4}{9}K^2[\frac{t_{pmg}^2}{(-E_g+2u_{gx}-3v_{pmn})^3}+\frac{t_{pmx1}^2}{(e_g-E_g+u_{gx}+u_{xx}-3v_{pmn})^3} \\ &\quad +\frac{t_{pmx2}^2}{(e_g-E_g+u_{gx}+u_{xx}-3v_{pmn})^3}]+O(t^3); \qquad (9.13) \\ J_3 &= \frac{4}{27}K^3[\frac{t_{pmg}^2}{(-E_g+2u_{gx}-3v_{pmn})^4}+\frac{t_{pmx1}^2}{(e_g-E_g+u_{gx}+u_{xx}-3v_{pmn})^4} \\ &\quad +\frac{t_{pmx2}^2}{(e_g-E_g+u_{gx}+u_{xx}-3v_{pmn})^4}]+O(t^3), \qquad (9.14) \end{aligned}$$

where t_{pmg}, t_{pmx1} and t_{pmx2} are the inter-molecular hopping integrals shown in Fig. (9.4), E_g and e_g are the energies of ligand and metal e_g states relative to the energy level of a_{1g} state, u_{gx} is Coulomb interaction between the a_{1g} and e_g levels, u_{xx} is the Coulomb interaction between two degenerate Mn e_g states, v_{pmn} is the Coulomb interaction between the Mn and Pc states.

9.4.3 Comment on the calculations

We note several features of this result. First, the dominant terms are those proportional to t^2, i.e. where electrons are exchanged once between the molecules, as

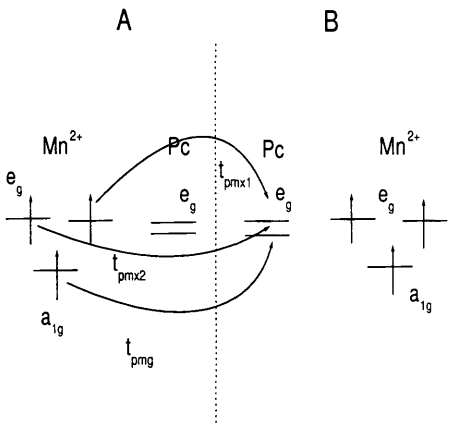

Fig. 9.4: The possible inter-molecular transitions.

expected in a super-exchange process. Second, the leading term in J_1 is proportional to Kt^2, in J_2 to K^2t^2, and in J_3 to K^3t^2; this is because $\hat{H}_p$ only couples states in which m_A and m_B alter by one unit of angular momentum. Finally, assuming the Coulomb energies are all large and positive, J_1 is *always* the same sign as K, irrespective of the values of the various hopping terms. In general we expect that K will be positive, corresponding to antiferromagnetic coupling in our sign convention, and therefore J_2 will also lead to a positive (antiferromagnetic) coupling *independent of the orientation of the molecules.*

The argument of Yamada et al.

Our conclusion about the failure of the superexchange interaction to change sign contrasts sharply with the explanation given by Barraclough *et al.* [65] and by Yamada *et al.* [66] for their experimental results, which they ascribe to the competition between different superexchange pathways operating via nitrogen atoms. These authors claim that two pathways, one operating via the a_{1g} state on the Mn atoms, the other via the e_g state, give opposite contributions to the sign of the exchange coupling, where E_g refers to ligand state:

- $[e_g \rightarrow E_g \rightarrow e_g] \Rightarrow$ anti-ferromagnetism
- $[a_{1g} \rightarrow E_g \rightarrow a_{1g}] \Rightarrow$ ferromagnetism.

However, this argument fails to take into account correctly the spin algebra—in particular, it ignores the fact that the three electron spins on each Mn atom are

in fact tied together via strong intra-atomic interactions, and so cannot be flipped independently.

9.5 Indirect exchange calculation

9.5.1 CuPc calculation

In this section we present the indirect exchange calculation between two Cu(II)Pc molecules. As shown in Figure 9.5, the metal unpaired electron spin can polarize the electron spin on the ligand by the two-body Coulomb interaction; and then the spin polarization can transfer to the neighbouring molecule by orbital hybridization. The metal unpaired spin of the neighbouring molecule experiences this spin polarization, and effectively interacts with the unpaired spin in the other molecule. Because the LUMOs are e_g states, we should consider the filled states with the same symmetry; in the other words, another pair of filled e_g states for the indirect exchange.

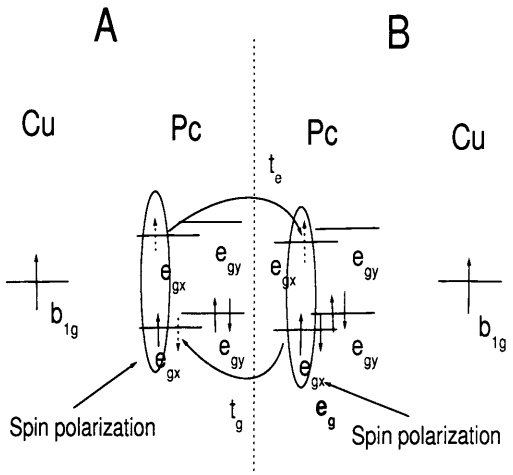

Fig. 9.5: Cu(II)Pc electron configuration and indirect exchange scheme diagram. This scheme involves two filled e_g states and two empty e_g states(LUMO).

The two-body Coulomb interaction may be represented as

$$\hat{v} = \sum_{\sigma\sigma'} \sum_{ABDE} [\int d\vec{r} d\vec{r}' \psi_A^*(\vec{r}) \psi_B^*(\vec{r}') \frac{1}{|\vec{r} - \vec{r}'|} \psi_D(\vec{r}') \psi_E(\vec{r})] \times c_{A,\sigma}^\dagger c_{B,\sigma'}^\dagger c_{D,\sigma'} c_{E,\sigma}, \tag{9.15}$$

where c and $c^\dagger$ are the electron annihilation and creation operators; A, B, D, E may represent a Cu orbital or a Pc orbital. The important terms in equation 9.15 are

those which rearrange electrons on the Cu atom and the ligand, but preserve the total number of electrons on each; thus one of (A, B) should correspond to a Cu state, i.e., metal b_{1g} state and one to a Pc state, e.g., ligand e_g state and similarly for (D, E).

Now we aim to calculate the matrix elements of $\hat{v}$ among ground state and spin-polarized states. To simplify the calculation, for the moment we consider only one component of the e_g doublet, e_{gx} or e_{gy}. If we use the symbol $|S_{\mathrm{Cu}}, S_{\mathrm{Pc}}\rangle$ to describe the metal spin state and ligand spin state within one molecule: then we need to consider the following two groups of spin states.

1. First, we consider states with total z-spin within one molecule $M_{\mathrm{tot}} = +1/2$. All of these can be produced by starting from a spin-up electron on the Cu, and the ligand ground state, and acting with the operator (9.15) to exchange a pair of electrons between the ligand and the metal. These states are $|(1/2), g\rangle$, $|(1/2), (S = 0, M = 0)\rangle$, $|(1/2), (S = 1, M = 0)\rangle$, and $|(-1/2), (S = 1, M = 1)\rangle$, where '$g$' refers to the ligand filled state; $(S = 0, M = 0)$ refers to the spin-polarized ligand singlet state as shown in Figure 9.6, and so on.

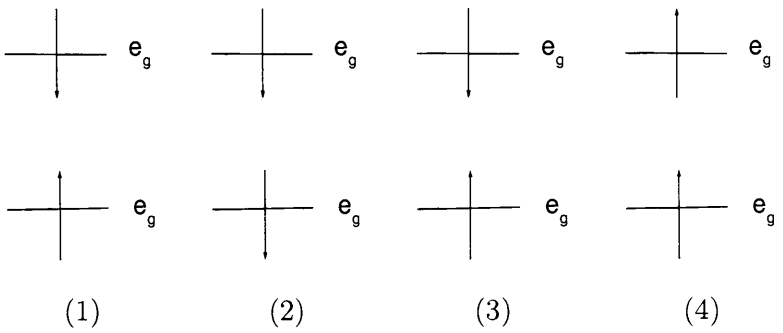

Fig. 9.6: Four spin-polarized states:(1)$|S = 0, M = 0\rangle$,(2)$|S = 1, M = -1\rangle$,(3)$|S = 1, M = 0\rangle$,and (4)$|S = 1, M = 1\rangle$.

Now we need to calculate the matrix elements of $\hat{v}$ between these states; to do this, it is convenient to represent the states themselves in terms of annihilation and creation operators:

$$|(1/2), g\rangle = c^{\dagger}_{b\uparrow} c^{\dagger}_{G\uparrow} c^{\dagger}_{G\downarrow} |0\rangle \tag{9.16}$$

$$|(-1/2), (S = 1, M = 1)\rangle = c^{\dagger}_{b\downarrow} c^{\dagger}_{G\uparrow} c^{\dagger}_{X\uparrow} |0\rangle, \tag{9.17}$$

where $|0\rangle$ is the empty state. 'X' refers to the spatial LUMO state of the ligand; 'G' refers to the filled states, and 'b' refers to metal b_{1g} state. Now we

can take the matrix element simply as

$$\begin{aligned}
&\langle(-1/2),(S=1,M=1)|\hat{\nu}|(1/2),g\rangle \qquad (9.18)\\
&=2\langle(-1/2),(S=1,M=1)|(c^\dagger_{X\uparrow}c^\dagger_{b\downarrow}c_{G\downarrow}c_{b\uparrow})c^\dagger_{b\uparrow}c^\dagger_{G\uparrow}c^\dagger_{G\downarrow}|0\rangle\\
&=-2\{X,b|b,G\}\langle(-1/2),(S=1,M=1)|c^\dagger_{b\downarrow}c^\dagger_{G\uparrow}c^\dagger_{X\uparrow}|0\rangle\\
&=-2\{X,b|b,G\}\langle(-1/2),(S=1,M=1)||(-1/2),(S=1,M=1)\rangle\\
&=-2\{X,b|b,G\},
\end{aligned}$$

where $\{a,b|c,d\}=\int d\vec{r}d\vec{r}'a(\vec{r})^*b(\vec{r}')^*\frac{1}{|\vec{r}-\vec{r}'|}c(\vec{r})d(\vec{r}')$.

Repeating for each pair of states, we can reach the following matrix representation of $\hat{v}$ among the four states with $M=+1/2$:

$$\hat{v}_{(\frac{1}{2})}=\begin{pmatrix} 0 & \beta & \alpha & -\sqrt{2}\alpha\\ \beta & 0 & 0 & \gamma\\ \alpha & 0 & 0 & \delta\\ -\sqrt{2}\alpha & \gamma & \delta & 0\end{pmatrix}, \qquad (9.19)$$

where

$$\alpha=2\{X,b|b,G\} \qquad (9.20)$$

$$\beta=[4\{b,X|b,G\}-2\{X,b|b,G\}]/\sqrt{2} \qquad (9.21)$$

$$\gamma=-[2\{b,G|G,b\}-2\{b,X|X,b\}]/\sqrt{2} \qquad (9.22)$$

$$\delta=[-2\{b,G|G,b\}-2\{b,X|X,b\}]/\sqrt{2} \qquad (9.23)$$

2. The states with total spin $M_{\rm tot}=-1/2$, $|(-1/2),g\rangle$, $|(-1/2),(S=0,M=0)\rangle$, $|(-1/2),(S=1,M=0)\rangle$, and $|(1/2),(S=1,M=-1)\rangle$, give rise to the following matrix elements:

$$\hat{v}_{(-\frac{1}{2})}=\begin{pmatrix} 0 & \beta & -\alpha & \sqrt{2}\alpha\\ \beta & 0 & 0 & -\gamma\\ -\alpha & 0 & 0 & \delta\\ \sqrt{2}\alpha & -\gamma & \delta & 0\end{pmatrix}. \qquad (9.24)$$

To get the leading terms in the effective Hamiltonian, we need consider a pair of molecules, A and B. Suppose $M_s^{\rm total}=M_s^{{\rm Cu}_A}+M_s^{{\rm Pc}_A}+M_s^{{\rm Cu}_B}+M_s^{{\rm Pc}_B}=0$. In this situation, we have 14 states if we only consider e_{gx} component and assume there is only one electron-hole pair on the two CuPcs. If we use the symbol

$|S_{\mathrm{Cu}_A}, S_{\mathrm{Pc}_A}|S_{\mathrm{Cu}_B}, S_{\mathrm{Pc}_B}\rangle$to label the spin states of two molecules, these states are

$$|1\rangle = |1/2, g| - 1/2, g\rangle \tag{9.25}$$
$$|2\rangle = |1/2, (S = 0, M = 0)| - 1/2, g\rangle \tag{9.26}$$
$$|3\rangle = |1/2, (S = 1, M = 0)| - 1/2, g\rangle \tag{9.27}$$
$$|4\rangle = |1/2, g| - 1/2, (S = 0, M = 0)\rangle \tag{9.28}$$
$$|5\rangle = |1/2, g| - 1/2, (S = 1, M = 0)\rangle \tag{9.29}$$
$$|6\rangle = |1/2, (S = 1, M = -1)|1/2, g\rangle \tag{9.30}$$
$$|7\rangle = |1/2, g|1/2, (S = 1, M = -1)\rangle \tag{9.31}$$
$$|8\rangle = | - 1/2, , (S = 1, M = 1)| - 1/2, g\rangle \tag{9.32}$$
$$|9\rangle = | - 1/2, g| - 1/2, (S = 1, M = 1)\rangle \tag{9.33}$$
$$|10\rangle = | - 1/2, g|1/2, g\rangle \tag{9.34}$$
$$|11\rangle = | - 1/2, (S = 0, M = 0)|1/2, g\rangle \tag{9.35}$$
$$|12\rangle = | - 1/2, (S = 1, M = 0)|1/2, g\rangle \tag{9.36}$$
$$|13\rangle = | - 1/2, g|1/2, (S = 0, M = 0)\rangle \tag{9.37}$$
$$|14\rangle = | - 1/2, g|1/2, (S = 1, M = 0)\rangle. \tag{9.38}$$

In these states four groups of states $\{|1\rangle, |2\rangle, |3\rangle, |8\rangle\}$, $\{|1\rangle, |4\rangle, |5\rangle, |7\rangle\}$, $\{|6\rangle, |10\rangle, |11\rangle, |12\rangle\}$, and $\{|9\rangle, |10\rangle, |13\rangle, |14\rangle\}$ are respectively coupled by $\hat{v}_{(\frac{1}{2})}$ or $\hat{v}_{(-\frac{1}{2})}$. Meanwhile, six groups of states: $\{|2\rangle, |4\rangle\}$, $\{|3\rangle, |5\rangle\}$, $\{|6\rangle, |7\rangle\}$,$\{|8\rangle, |9\rangle\}$, $\{|11\rangle, |13\rangle\}$, and $\{|12\rangle, |14\rangle\}$ are coupled by the spin polarization transfer matrix element t which hops a spin-polarized excitation from ligand A to ligand B. We assume this amplitude is the same for singlet and spin-1 states.

We can now apply perturbation theory to this problem as in Chapter 4; the perturbation includes the Coulomb interaction $\hat{v}$ which can spin-polarize a ligand, and the hopping t that transfers this polarization from one molecule to another. We find that the leading term J_1 in the spin-$\frac{1}{2}$ couplings:

$$J_1 = \frac{4\alpha^2 t}{(U_g - U_x - E_x - 2exj)^2}; \tag{9.39}$$
$$\tag{9.40}$$
$$U_g = \{G, G|G, G\} \tag{9.41}$$
$$U_x = \{G, X|G, X\} \tag{9.42}$$
$$exj = \{G, X|X, G\}, \tag{9.43}$$

where U_g is the Coulomb interaction between two electrons in the ground state, U_x is the Coulomb interaction between electron and hole within one molecule,exj is the

electron-hole exchange integral, and E_x is the intra-molecule one-electron energy gap. To calculate the exciton coupling t we consider the four states below (See Figure 9.7), and do a simple Green's function perturbation theory calculation. We find $t = \frac{2t_e t_g}{E_x + U_x}$, where $t_{g,e}$ are the single-particle transfer integrals in the filled and LUMO e_g states (i.e. for the electron and hole parts of the spin polarization).

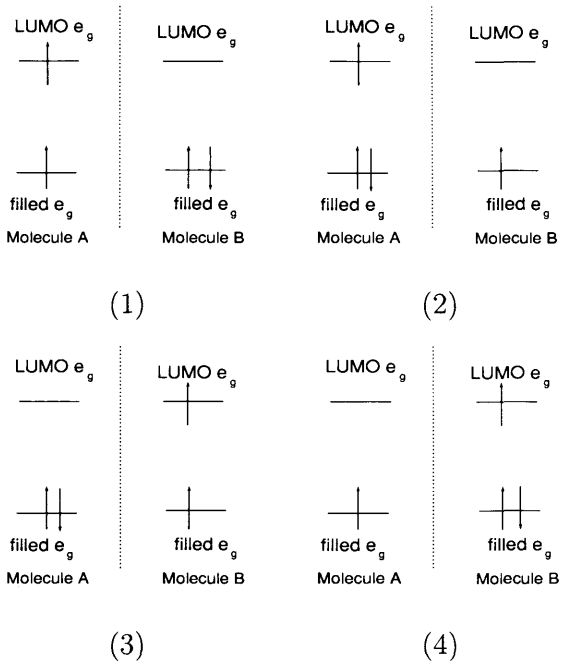

Fig. 9.7: The four states we need to consider to calculate the polarized triplet state as the example.

In our single-molecule Cu(II)Pc DFT calculation (see §9.2.1) we identified ligand e_g states are LUMOs and the single-occupied b_{1g} state as largely Cu-derived (Mulliken population on coppers 0.3). So the four indices in the two-electron integrals $\{\alpha, \beta|\gamma, \delta\}$ relevant to the perturbation theory may involve one entry for an e_g LUMO state, two entries for the b_{1g} state, and one entry for a doubly-filled ligand state: the highest-lying such states are a_{1u}, a_{2u}, or b_{2g}. However, because a_{1u} and a_{2u} are odd under inversion, but b_{1g} and e_g are even, the two-electron integrals involving a_{1u} and a_{2u} are zero. Furthermore b_{2g} transforms like xy in D_{4h} symmetry, b_{1g} like $x^2 - y^2$, and $e_{gx,y}$ like zx, zy. The two-electron integral involving b_{2g} is therefore odd in either y or in x depending which e_g state appears. So, in fact the only important doubly-occupied states are the filled e_g states which appear slightly below the a_{1u} and a_{2u}.

Now, we need to calculate the single-electron transfer integrals t_e and t_g and their dependence on stacking angles. At this point we recall that the e_g LUMO in

fact consists of two states, $e_{gx,y}$. So the total transfer integral reads

$$t = t^x + t^y; \tag{9.44}$$

$$t^x = \frac{t_e^x t_g^x}{u} \tag{9.45}$$

$$t^y = \frac{t_e^y t_g^y}{u} \tag{9.46}$$

$$t_e^i = \langle e_{g,i}^{1,u} | \hat{H}_{core} | e_{g,i}^{2,u} \rangle \tag{9.47}$$

$$t_g^i = \langle e_{g,i}^{1,o} | \hat{H}_{core} | e_{g,i}^{2,o} \rangle \tag{9.48}$$

$$i = x, y \tag{9.49}$$

where $\hat{H}_{core}$ is two-molecule core Hamiltonian including kinetic and potential energies of two molecules which can be calculated using Gaussian 98 codes. The symbols $1, 2$ refer to these two molecules, and $e_g^{1,2}$ refer to e_g single-molecule state belonging to molecule 1 or 2. The symbols u, o mean 'unoccupied' and 'occupied'.

Semi-numerical calculation of inter-molecule transfer integrals

We have used Gaussian 98 codes to work out the two-molecule core Hamiltonian, and we can use the single-molecule orbital coefficients to calculate the above transfer integrals t_e, t_g in several different molecular configurations. We fix one molecule and move the other molecule, meanwhile we keep the two molecule planes parallel. The distance between these two planes is 3.4 Angstroms as shown in Figure 9.8. We change the angle from 20 degrees to 90 degrees with the step being 5 degrees. Because α, u, and E_x are intra-molecule terms, so the indirect exchange only depends on inter-molecule single-electron transfer integrals as shown in Figure 9.9.

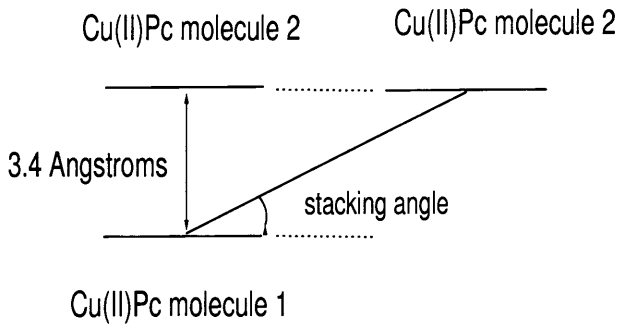

Fig. 9.8: The spatial configuration of two Cu(II)Pc molecules.

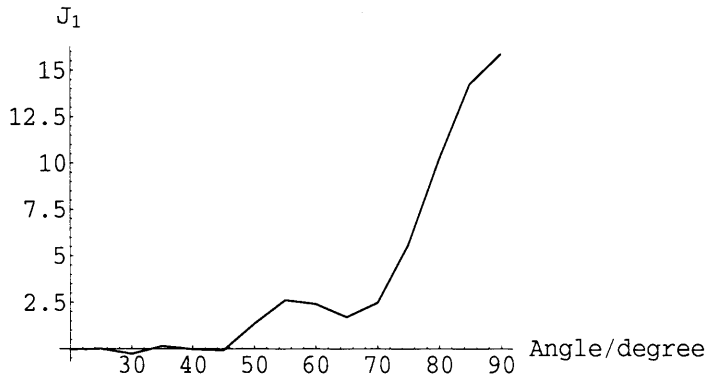

Fig. 9.9: In this figure when the angle is equal to 45 degrees, J_1 is equal to -0.0691195. When the angle is equal to 65 degrees, J_1 is equal to 1.71449.

9.5.2 Mn(II)Pc calculation

The Mn(II)Pc calculation is more complicated because there are three unpaired electrons per molecule which occupy a_{1g}, and e_g states, so it is necessary to use group theory to simplify the 2-electron integral calculation. We know that $\frac{1}{|\vec{r}-\vec{r}'|}$ belongs to the identity representation. We now need to find the symmetry properties of the products of pairs of one-electron functions that appear in Equation 9.15: first, we consider the products of two e_g states. Eventually, we will consider the scattering between filled and empty e_g levels in the molecule, through interaction with the e_g states of the Mn ion. To do this, we need the elements of the matrix X such that

$$X^{-1}[e_g \otimes e_g]X \;=\; a_{1g} \oplus b_{1g} \oplus a_{2g} \oplus b_{2g}, \tag{9.50}$$

which are the Clebsch-Gordan coefficients for the product representation $e_g \otimes e_g$. We can label them as $X(\alpha, ij)$ where α refers to one of the irreducible representations appearing on the right of equation (9.50), and i, j label the functions transforming as e_g. We find

$$X = \begin{array}{c} \\ xx \\ xy \\ yx \\ yy \end{array} \begin{array}{c} \begin{array}{cccc} a_{1g} & a_{2g} & b_{1g} & b_{2g} \end{array} \\ \begin{pmatrix} 1/\sqrt{2} & 0 & 1/\sqrt{2} & 0 \\ 0 & 1/\sqrt{2} & 0 & 1/\sqrt{2} \\ 0 & -1/\sqrt{2} & 0 & 1/\sqrt{2} \\ 1/\sqrt{2} & 0 & -1/\sqrt{2} & 0 \end{pmatrix} \end{array}. \tag{9.51}$$

Using these results, we can rewrite $\hat{v}$ as:

$$\hat{v} = \sum_{\sigma,\sigma'}\sum_{\alpha}\int d\vec{r}d\vec{r}'\Psi^{(\alpha)*}\frac{1}{|\vec{r}-\vec{r}'|}\Psi^{(\alpha)}\sum_{ABDE}X(\alpha,AB)X^*(\alpha,DE) \times c^{\dagger}_{A,\sigma}c^{\dagger}_{B,\sigma'}c_{D,\sigma'}c_{E,\sigma}, \tag{9.52}$$

We can write $\hat{v}$ in shortened form as:

$$\hat{v} = \frac{1}{2}\sum_{\alpha}\int d\vec{r}d\vec{r}'\Psi^{(\alpha)*}\frac{1}{|\vec{r}-\vec{r}'|}\Psi^{(\alpha)}\sum_{\sigma,\sigma'}\hat{O}^T M^{\alpha}\hat{P}; \tag{9.53}$$

$$\hat{O} = \begin{pmatrix} C^{\dagger}_{x,\sigma}C^{\dagger}_{x,\sigma'} \\ C^{\dagger}_{x,\sigma}C^{\dagger}_{y,\sigma'} \\ C^{\dagger}_{y,\sigma}C^{\dagger}_{x,\sigma'} \\ C^{\dagger}_{y,\sigma}C^{\dagger}_{y,\sigma'} \end{pmatrix} \tag{9.54}$$

$$\hat{P} = \begin{pmatrix} C_{x,\sigma'}C_{x,\sigma} \\ C_{x,\sigma'}C_{y,\sigma} \\ C_{y,\sigma'}C_{x,\sigma} \\ C_{y,\sigma'}C_{y,\sigma} \end{pmatrix} \tag{9.55}$$

$$M^{A_{1g}} = \begin{pmatrix} 1 & 0 & 0 & 1 \\ 0 & 0 & 0 & 0 \\ 0 & 0 & 0 & 0 \\ 1 & 0 & 0 & 1 \end{pmatrix} \tag{9.56}$$

$$M^{A_{2g}} = \begin{pmatrix} 0 & 0 & 0 & 0 \\ 0 & 1 & -1 & 0 \\ 0 & -1 & 1 & 0 \\ 0 & 0 & 0 & 0 \end{pmatrix} \tag{9.57}$$

$$M^{B_{1g}} = \begin{pmatrix} 1 & 0 & 0 & -1 \\ 0 & 0 & 0 & 0 \\ 0 & 0 & 0 & 0 \\ -1 & 0 & 0 & 1 \end{pmatrix} \tag{9.58}$$

$$M^{B_{2g}} = \begin{pmatrix} 0 & 0 & 0 & 0 \\ 0 & 1 & 1 & 0 \\ 0 & 1 & 1 & 0 \\ 0 & 0 & 0 & 0 \end{pmatrix} \tag{9.59}$$

$$\Psi^{(A_{1g})} = \frac{1}{\sqrt{2}}(|xx\rangle + |yy\rangle) \tag{9.60}$$

$$\Psi^{(A_{2g})} = \frac{1}{\sqrt{2}}(|xy\rangle - |yx\rangle) \tag{9.61}$$

$$\Psi^{(B_{1g})} = \frac{1}{\sqrt{2}}(|xx\rangle - |yy\rangle) \tag{9.62}$$

$$\Psi^{(B_{2g})} = \frac{1}{\sqrt{2}}(|xy\rangle + |yx\rangle). \tag{9.63}$$

We use X, Y to label the ligand e_{gx}, e_{gy} states, and x, y to label Mn e_{gx}, e_{gy} orbitals. Now we introduce operators which create electron-hole excitations with different spin symmetries on the Pc:

$$a_i^S = \frac{1}{\sqrt{2}}(a_i^{+\uparrow\downarrow} + a_i^{+\downarrow\uparrow}); a_i^T = \frac{1}{\sqrt{2}}(a_i^{+\uparrow\downarrow} - a_i^{+\downarrow\uparrow}) \tag{9.64}$$

$$a_i^{+\uparrow\uparrow} = c_{ix\uparrow}^\dagger c_{ig\downarrow}; a_i^{+\uparrow\downarrow} = c_{ix\downarrow}^\dagger c_{ig\downarrow} \tag{9.65}$$

$$a_i^{+\downarrow\uparrow} = c_{ix\uparrow}^\dagger c_{ig\uparrow}; a_i^{+\downarrow\downarrow} = c_{ix\downarrow}^\dagger c_{ig\downarrow}, \tag{9.66}$$

where i runs over the two orientations of the ligand e_g states ($i = X,\ Y$), and also operators characterizing the spin degrees of freedom:

$$S_j^z = \frac{1}{2}(n_{j\uparrow} - n_{j\downarrow}) \tag{9.67}$$

$$S_j^\dagger = c_{j\uparrow}^\dagger c_{j\downarrow} \tag{9.68}$$

$$S_j^- = c_{j\downarrow}^\dagger c_{j\uparrow}, \tag{9.69}$$

where j runs over all the e_g states of the Mn ion and the ligand: $j = X_x, X_g, Y_x, Y_g, x, y$. Using these operators, we can expand $\hat{v}$ as,

$$\hat{v} = \hat{v}_1 + \hat{v}_2 + \hat{v}_3 + \text{spin-independent terms}, \tag{9.70}$$

where

$$\begin{aligned} \hat{v}_1 = {} & (a_X^S + a_Y^S)(2\sqrt{2}(P_3 + P_4 - P_1/2 - P_2/2)) \\ & +2\sqrt{2}a_X^T(P_1 S_x^z + P_2 S_y^z) + 2\sqrt{2}a_Y^T(P_2 S_x^z + P_1 S_y^z) \\ & +2S_x^\dagger(P_1 a_X^{\dagger\downarrow\downarrow} + P_2 a_Y^{\dagger\downarrow\downarrow}) + 2S_y^\dagger(P_1 a_Y^{\dagger\downarrow\downarrow} + P_2 a_X^{\dagger\downarrow\downarrow}) \\ & -2S_x^-(P_1 a_X^{\dagger\uparrow\uparrow} + P_2 a_Y^{\dagger\uparrow\uparrow}) - 2S_y^-(P_1 a_Y^{\dagger\uparrow\uparrow} + P_2 a_X^{\dagger\uparrow\uparrow}) \end{aligned} \tag{9.71}$$

$$\hat{v}_2 = 2(n_{x\uparrow}[-P_5 n_{X_x\uparrow} - P_6 n_{Y_x\uparrow}] + n_{x\downarrow}[-P_5 n_{X_x\downarrow} - P_6 n_{Y_x\downarrow}] + \tag{9.72}$$

$$
\begin{aligned}
& n_{y\uparrow}[-P_5 n_{Y_x\uparrow} - P_6 n_{X_x\uparrow}] + n_{y\downarrow}[-P_5 n_{Y_x\downarrow} - P_6 n_{X_x\downarrow}] + \\
& S_x^{\dagger}[-P_5 S_{X_x}^{-} - P_6 S_{Y_x}^{-}] + S_y^{\dagger}[-P_5 S_{Y_x}^{-} - P_6 S_{X_x}^{-}] + \\
& S_x^{-}[-P_5 S_{X_x}^{\dagger} - P_6 S_{Y_x}^{\dagger}] + S_y^{-}[-P_5 S_{Y_x}^{\dagger} - P_6 S_{X_x}^{\dagger}]) \\
\hat{v}_3 \;=\; & 2(n_{x\uparrow}[-P_5' n_{X_g\uparrow} - P_6' n_{Y_g\uparrow}] + n_{x\downarrow}[-P_5' n_{X_g\downarrow} - P_6' n_{Y_g\downarrow}] + \\
& n_{y\uparrow}[-P_5' n_{Y_g\uparrow} - P_6' n_{X_g\uparrow}] + n_{y\downarrow}[-P_5' n_{Y_g\downarrow} - P_6' n_{X_g\downarrow}] + \\
& S_x^{\dagger}[-P_5' S_{X_g}^{-} - P_6' S_{Y_g}^{-}] + S_y^{\dagger}[-P_5' S_{Y_g}^{-} - P_6' S_{X_g}^{-}] + \\
& S_x^{-}[-P_5' S_{X_g}^{\dagger} - P_6' S_{Y_g}^{\dagger}] + S_y^{-}[-P_5' S_{Y_g}^{\dagger} - P_6' S_{X_g}^{\dagger}]),
\end{aligned}
\tag{9.73}
$$

and

$$P_1 = \{x, X_x | X_g, x\} + \{y, Y_x | Y_g, y\} \tag{9.74}$$

$$P_2 = \{x, Y_x | Y_g, x\} + \{y, X_x | X_g, y\} \tag{9.75}$$

$$P_3 = \{X_x, x | X_g, x\} + \{Y_x, y | Y_g, y\} \tag{9.76}$$

$$P_4 = \{X_x, y | X_g, y\} + \{Y_x, x | Y_g, x\} \tag{9.77}$$

$$P_5 = \{x, X_x | X_x, x\} + \{y, Y_x | Y_x, y\} \tag{9.78}$$

$$P_6 = \{x, Y_x | Y_x, x\} + \{y, X_x | X_x, y\} \tag{9.79}$$

$$P_5' = \{x, X_g | X_g, x\} + \{y, Y_g | Y_g, y\} \tag{9.80}$$

$$P_6' = \{x, Y_g | Y_g, x\} + \{y, X_g | X_g, y\}. \tag{9.81}$$

Using this form of $\hat{v}$, we can build the Hamiltonian matrix for two sets of wave functions: those in which the total z-component of spin on one molecule (Mn plus ligand) is respectively $+3/2$ and $+1/2$. We label the individual states as $|S_{\mathrm{Mn(II)}}, S_{\mathrm{Pc}}\rangle$; the first is the spin configuration of Mn, and second is the spin configuration of Pc in the X or Y spatial component.)

1. The $+3/2$ states are $|(3/2), g\rangle$, $|(3/2), (S = 0, M = 0)\rangle$, $|(3/2), (S = 1, M = 0)\rangle$, $|(1/2), (S = 1, M = 1)\rangle$, and the corresponding matrix is

$$\hat{v}_{\frac{3}{2}} = \begin{pmatrix} 0 & \beta & \frac{3}{2}\alpha & -\sqrt{\frac{3}{2}}\alpha \\ \beta & 0 & 0 & \gamma \\ \frac{3}{2}\alpha & 0 & 0 & \sqrt{6}\delta \\ -\sqrt{\frac{3}{2}}\alpha & \gamma & \sqrt{6}\delta & 0 \end{pmatrix}, \tag{9.82}$$

where $\alpha = 2\sqrt{2}/3(P_1 + P_2), \beta = 2\sqrt{2}(P_3 + P_4 - 1/2P_1 - 1/2P_2), \gamma = \sqrt{6}/3(P_5' + P_6' - P_5 - P_6), \delta = 1/3(-P_5' - P_6' - P_5 - P_6)$.

2. The $+1/2$ states are $|(1/2), g\rangle$, $|(1/2), (S = 0, M = 0)\rangle$, $|(1/2), (S = 1, M = 0)\rangle$, $|(-1/2), (S = 1, M = 1)\rangle$, $|(3/2), (S = 1, M = -1)\rangle$, and the matrix of

Coulomb interaction $\hat{v}$ is

$$\hat{v}_{\frac{1}{2}} = \begin{pmatrix} 0 & \beta & 1/2\alpha & -\sqrt{2}\alpha & \sqrt{3/2}\alpha \\ \beta & 0 & 0 & 2/\sqrt{3}\gamma & -\gamma \\ 1/2\alpha & 0 & 0 & 2\sqrt{2}\delta & \sqrt{6}\delta \\ -\sqrt{2}\alpha & 2/\sqrt{3}\gamma & 2\sqrt{2}\delta & 0 & 0 \\ \sqrt{3/2}\alpha & -\gamma & \sqrt{6}\delta & 0 & 0 \end{pmatrix}. \tag{9.83}$$

To get the leading terms in the effective Hamiltonian in the equation 9.9, we need consider the situation where the total z-direction angular momentum on *both* molecules is $M_{total} = M_s^{\mathrm{Mn}_A} + M_s^{\mathrm{Mn}_B} + M_s^{\mathrm{Pc}} = 2$. In this situation, we have 18 states if we only consider X component and assume there is only one electron-hole pair in total on the two Mn(II)Pc molecules. These 18 states are made up as follows:

$$(M_s^{\mathrm{Mn}_A} = 3/2, M_s^{\mathrm{Mn}_B} = 1/2, M_s^{\mathrm{Pc}} = 0) \rightarrow 5 \text{ states} \tag{9.84}$$

$$(M_s^{\mathrm{Mn}_A} = 1/2, M_s^{\mathrm{Mn}_B} = 3/2, M_s^{\mathrm{Pc}} = 0) \rightarrow 5 \text{ states} \tag{9.85}$$

$$(M_s^{\mathrm{Mn}_A} = 1/2, M_s^{\mathrm{Mn}_B} = 1/2, M_s^{\mathrm{Pc}} = 1) \rightarrow 2 \text{ states} \tag{9.86}$$

$$(M_s^{\mathrm{Mn}_A} = 3/2, M_s^{\mathrm{Mn}_B} = -1/2, M_s^{\mathrm{Pc}} = 0) \rightarrow 2 \text{ states} \tag{9.87}$$

$$(M_s^{\mathrm{Mn}_A} = -1/2, M_s^{\mathrm{Mn}_B} = 3/2, M_s^{\mathrm{Pc}} = 0) \rightarrow 2 \text{ states} \tag{9.88}$$

$$(M_s^{\mathrm{Mn}_A} = 3/2, M_s^{\mathrm{Mn}_B} = 3/2, M_s^{\mathrm{Pc}} = -1) \rightarrow 2 \text{ states.} \tag{9.89}$$

When we apply perturbation theory to this problem, the perturbation includes both the Coulomb interaction $\hat{v}$ discussed above, and the hopping t which transfers an electron-hole pair from one Mn(II)Pc to another. We found the leading term of spin-$\frac{3}{2}$ couplings J_1 to be:

$$J_1 = \frac{3\alpha^2 t}{(U_g - U_x - E_x - 2exj)^2}, \tag{9.90}$$

where the definitions of U_g, U_x, E_x, exj, t_e and t_g are the same as those in the Cu(II)Pc calculation. So far we only consider one component of ligand e_g states, so similar with Cu(II)Pc calculation we should combine the transfer integrals which respectively involve x or y components,i.e, $t = t^x + t^y$. By the similar procedure to Cu(II)Pc, we find a weak ferromagnetic interaction when the stacking angle is 45° but a relatively strong anti-ferromagnetic interaction for 65°.

9.6 Conclusion and discussion

From P.T. calculations of Cu(II)Pc and Mn(II)Pc we can see that the exchange interaction between two Cu(II)Pc molecules is dominated by indirect exchange. But

in Mn(II)Pc both super-exchange and indirect exchange contribute. The sign of the indirect exchange interaction in both cases is dependent on the sign of inter-molecule electron transfer integrals; however, the most important terms in the super-exchange are always positive (anti-ferromagnetic).

In the case of the Cu(II)Pc dimer, when the stacking angle is 65 degrees, the indirect exchange is predicted to be anti-ferromagnetic, while when the stacking angle is 45 degrees, the indirect exchange is very weakly ferromagnetic. Both these results agree qualitatively with the experimental observations (see §9.1).

The main discrepancy with the experiments is in the case of Mn(II)Pc, where our P.T. calculations do not give very strong ferromagnetism which was shown in experiments. This is probably because the true exchange interaction involves the competition between super-exchange (always antiferromagnetic) and indirect exchange (predicted to be once again anti-ferromagnatic at 65°, weakly ferromagnetic at 45°), as well as possibly other routes. The different mechanisms involve different intra-molecular couplings, and so this competition is very difficult to quantify on the basis of model calculations.

At this point, therefore, we can claim only a qualitative understanding of spin-1/2 couplings between Cu(II)Pc. To go beyond this a complete electronic structure calculation of the two-molecule system will be needed; this is reported in the next chapter.

10. *AB INITIO* DFT CALCULATION OF EXCHANGE INTERACTION IN CUPC DIMER

10.1 Introduction

In the last chapter, we described a model calculation for the indirect exchange between two Cu(II)Pc molecules, but it is only a qualitative calculation which gives the trends in the exchange interaction. In order to obtain quantitative information, and also to benchmark our perturbation theory, we need an *ab initio* calculation for the biradical exchange interaction; this enables a direct comparison of our theoretical results with experimental measurements, and also gives additional information such as: the unpaired electron orbitals in each molecule, charge distributions, spin densities, and other electronic properties. In this chapter we describe density functional theory (DFT) calculations, using the broken-symmetry concept [76] and Gaussian 98 code [68] to quantify the exchange.

10.2 Previous work on DFT calculations of exchange constants in molecule dimers

It is necessary to compute the energies of high-spin and low-spin states in order to calculate magnetic coupling constants. This causes problems in DFT calculations, because they do not allow the use of pure spin eigenfunctions for the low-spin states, since (unlike the high-spin states) they cannot be accurately described within a single Kohn-Sham determinant. So one has to use instead a so-called 'broken-symmetry' method, in which the magnetic orbitals are localized in different radical centres, with their spins oppositely-aligned.

The first attempt to calculate a magnetic coupling constant as a singlet-triplet splitting of the excited states of closed-shell molecules was made by Bagus and Bennett [74] using $X\alpha$ scattered wave methods, and developed by Ziegler [75]. Noodleman [76] proposed the broken-symmetry approach to magnetic couplings; Yamaguchi *et al.*, [77] made a significant contribution to broken-symmetry unrestricted Hartree-Fock (UHF) calculations for the magnetic coupling in the framework of $X\alpha$. They used the spin vector model and ab initial UHF to calculate the exchange in-

teraction for ironsulfur clusters in ferredoxins. They found the spin vector model is useful for a localized representation of complex antiferromagnetic spin couplings between the high-spin iron atoms (ions).

The broken-symmetry approach has been applied to the metal radical system and the results are very good [78]. But treating exchange and correlation at only the $X\alpha$ or UHF level can give at best qualitative results for magnetic couplings. Later Martin and Illas [79, 80] checked the performances of different exchange-correlation functionals in the calculation of magnetic couplings, and found the choice of exchange functionals is extremely important, while the role of the correlation functional is minor. Martin and Illas found it necessary to mix half Generalised Gradient Approximations (GGA) and half Hartree-Fock exchange to reach quantitative agreement with the experimental values. But the proportions of the mixture are still semi-empirical: the well-known hybrid functional B3LYP [69, 81, 82] which mixes about one quarter Hartree-Fock exchange also gives good results for some di-nuclear molecules and organic biradicals.

Recently, based on the idea that the lowest energy with total zero z-component of total spin is a good approximation to the lowest singlet, Ruiz [84] proposed to use B3LYP and considered the energy of broken-symmetry state as that of the singlet to calculate the magnetic coupling in organic biradical and dinuclear complexes. However, this approach has been criticised by other authors [85].

10.3 Molecule Geometry

We now describe the calculation of the exchange interactions in a Copper(II)-Phthalocyanine (Cu(II)Pc) dimer. As described in §9.1 this material has two phases: a thin film (stacking angle 65°) and a powder (stacking angle 45°). We performed DFT calculations on Cu(II)Pc dimers with these two stacking angles.

10.4 Calculation Methods

10.4.1 Broken-symmetry concept

In principle, one can calculate the exchange coupling in a biradical by using an *ab initio* Self-Consistent Field-Configuration Interaction (SCF-CI) calculation. However, in practice, this approach is very expensive because several different weakly-coupled electron pairs may be involved, and as a result the CI expansion converges only slowly.

As an alternative, in 1980 Noodleman [76] proposed that the exchange coupling in

a molecular or atomic dimer can be calculated by the difference between the energies of an antiferromagnetic state which contains nonorthogonal magnetic orbitals, and of the highest-spin state. He considered the interaction of two identical high-spin monomers with oppositely aligned spins, and proposed a single-configuration model to represent this antiferromagnetic state. When the magnetic orbitals of the two subunits interact to form an overall low-spin state (for example, one up and one down), a state of mixed spin symmetry and lowered spatial symmetry is obtained. Noodleman referred to this as the 'mixed-spin' or 'broken-symmetry' state. The energy of the broken-symmetry state is a specific weighted average of the energies of the pure spin states: if the magnetic centres have spins S_1 and S_2, the exchange coupling is [76]

$$J = \frac{E_T - E_{BS}}{2S_1S_2}. \tag{10.1}$$

The calculation of the total energies E_T and E_{BS} can in principle be done using DFT or UHF methods; we have applied the technique using DFT.

10.4.2 B3LYP DFT calculation

We use the hybrid density functional B3LYP [69], which is already implemented within the Gaussian code [68], to calculate the total energies of the broken-symmetry and triplet states. These functionals have been found to give good descriptions of exchange interactions in other organic systems [80].

First of all, it is necessary to introduce the origin of B3LYP. Before Becke's exchange energy functional was proposed, gradient-corrected exchange energy functionals could not give the correct $1/r$ asymptotic behavior of the exchange density. In 1988 Becke [81] proposed his gradient-corrected exchange functional which gives the proper asymptotic limit. In addition, this functional fitted the Hartree-Fock exchange energy of a wide range of atoms and molecules very well. Becke's exchange functional reads:

$$E_X = E_X^{LDA} - \beta \sum_\sigma \int \rho_\sigma^{4/3} \frac{x_\sigma^2}{1 + 6\beta x_\sigma \sinh^{-1} x_\sigma} dr^3, \tag{10.2}$$

where β is a constant which can be determined by fitting to an exact Hartree-Fock exchange, $x_\sigma = \frac{|\nabla \rho_\sigma|}{\rho_\sigma^{4/3}}$. σ is a spin label (up or down).

In 1992, Becke [69] proposed a further exchange-correlation approximation,

$$E_{XC} = E_{XC}^{LSDA} + a_0(E_X^{exact} - E_X^{LSDA}) + a_X \Delta E_X^{B88} + \Delta E_C^{PW91}, \tag{10.3}$$

where $a_0 = 0.2, a_X = 0.72, a_C = 0.81$ are determined by fitting to the 56 atomization energies, 42 ionization potentials, 8 proton affinities, and 10 first-row atomic energies

in the G1 molecule set [83], and E_X^{exact} is the exact exchange energy. ΔE_X^{B88} is Becke's gradient correction for the exchange energy; ΔE_C^{PW91} is the 1991 gradient correction for correlation of Perdew and Wang [86]. In B3LYP functional, LYP and the VWN [87] correlation functional replace PW91. Since LYP [82] includes both local and non-local terms, the correlation functional used is actually: $a_C E_C^{LYP} + (1 - a_C) E_C^{VWN}$. In other words, VWN is used to provide the excess local correlation required, since LYP contains a local term essentially equivalent to VWN.

10.5 Calculation results

We carried out the energy calculation from the Gaussian code [68], using a 631–G basis (6 gaussian functions for the inner-shell wave functions, 3 for the inner part of valence shell, 1 for the outer part of valence shell) and the B3LYP or Unrestricted B3LYP(UB3LYP) exchange-correlation functionals [82, 69].

10.5.1 Cu(II)Pc

We can compare directly the total energies in our DFT calculations, and hence calculate directly the exchange splitting of eq. (10.1). In all cases we found it necessary to optimize carefully the occupancy of the Kohn-Sham orbitals in order to ensure that there is no charge disproportion between the molecules; our lowest-energy converged states have Mulliken charges of approximately +0.99, and nominal spin populations of ±0.68, on each Cu atom. Our numerical convergence is to 5×10^{-9} Hartree for $\theta = 45°$, and to 1×10^{-11} Hartree for $\theta = 65°$, and we find negligible spin contamination in our final wavefunctions ($\langle \hat{S}^2 \rangle = 2.0053$ for triplets, 1.0053 for broken-symmetry states, in each case).

We find that the broken-symmetry state is favoured in each case, corresponding to net antiferromagnetic coupling: for $\theta = 45°$ we have $E_{BS} - E_T = -1.1 \times 10^{-6}$ Hartree, and for $\theta = 65°$ we have $E_{BS} - E_T = -5.5 \times 10^{-6}$ Hartree.

System	E (Hartree)	Convergence	$\langle S^2 \rangle$	Cu charge	Cu spin
β, $\theta = 45°$, BS	-6614.125948827	0.1688×10^{-9}	1.0053	0.99;0.99	-0.68;0.68
β, $\theta = 45°$, triplet	-6614.125947894	0.4602×10^{-9}	2.0053	0.99;0.99	0.68;0.68
α, $\theta = 65°$, BS	-6614.116522	0.9521×10^{-11}	1.0053	0.98;0.98	-0.68;0.68
α, $\theta = 65°$, triplet	-6614.116517	0.9882×10^{-11}	2.0053	0.98;0.98	0.68;0.68

10.5.2 Conclusion

We have shown that a consistent picture of the magnetism in CuPc dimers can be constructed by using the broken-symmetry approach [76]. As expected, we find that

the spin densities on two of the copper atoms are opposite in the broken-symmetry state, but the same in the triplet state; we also find that the expectation value of the total spin, $\langle \hat{S}^2 \rangle$, is very close to 1 in the broken-symmetry state, and 2 2 in the triplet state. This is consistent with the expected composition of the broken-symmetry state as an equal mixture of the singlet and ($M_S = 0$) triplet. It is remarkable that, despite the very different methodologies, the final results for the exchange constants computed using density-functional theory in the broken symmetry approoach are entirely consistent with out previous perturbation theory expressions (see Chapter 9).

A word of caution is in order here. We should remember that the energy differences computed from the DFT are very small (of order 0.1 meV, compared with an overall total energy of about 7×10^4 eV). In particular they are much smaller than the normal margin of error associated with a DFT calculation (normally taken to be around 0.1 eV for total energies). Their reliability therefore rests heavily on the cancellation of errors between the different spin states. The precise extent of this error cancellation is largely unknown, but in other calculations [79, 89] energy differences as small as 1 meV have been interpreted in terms of physical exchange energies. It is not clear whether the even smaller energy differences found in the present calculations are significant, but the qualitative agreement (over a range of tilt angles) with the perturbation theory is very encouraging. It is likely that, since they approach the problem from completely different limits, both these calculations are reliable in the region where they agree.

Part III

CONCLUSIONS

11. CONCLUSIONS AND SUGGESTIONS FOR FURTHER WORK

The first part of the thesis deals with various theoretical aspects of the proposal to implement quantum gates using spins bound at impurities in silicon and controlled by optical excitation, which is currently under investigation in UCL.

The first question addressed is the magnitude of the exchange interaction between donors, especially when these donors have states that lie deeper than predicted by effective-mass theory and/or when a complex of more than two defects is involved. To deal with deep impurities one has to go beyong effective-mass theory: I exploit a variant of the quantum defect method to obtain a donor wave function which is regular far from defect centre but divergent near the defect centre, and then choose a simple central-cell correction (a δ-function potential or a square-well potential) in order to make the wavefunction regular at the defect nucleus. This potential gives a natural way of incorporating information about the chemical nature of the deep donor in a manner that can then be used in a conventional Heitler-London type exchange calculation. The matched wave function can be well fitted by using a linear combination of Gaussian functions, providing a convenient form for the subsequent exchange calculation. Although the accuracy of exchange calculation depends on the accuracy of the Gaussian fitting, this procedure enables us to calculate the exchange interaction between two donor electrons having arbitrary binding energies, which can be adjusted to match the experimental binding energies of the species concerned.

As a special case of a defect complex, I consider a three-impurity system. This is particularly important for the proposed quantum gates since these envisage a so-called 'control atom' which can be placed in an excited state in order to enhance the exchange interactions between other donor atoms which carry the quantum information. I treat the symmetric case in which the 'control' is equidistant from the two 'qubits'. I perform a variational calculation in which the control electron is given the freedom to reside on different parts of the three-atom complex; I find that the exchange interaction between two qubits is increased when the control electron becomes delocalized around those three donor centers; this delocalization may induce the charge transfer from control atom to the qubit atoms and alter the exchange

interactions further, and that it is even possible for the exchange interaction between pairs of qubits in the system to become ferromagnetic. (This is impossible in a simple two-donor, two-electron system.) I find that these observations can be rationalized by using Green's function perturbation theory; furthermore, the origin of the ferromagnetic exchange interaction can be explained in terms of multi-centre exchange processes.

Following the calculation of the exchange interaction between immediate neighbours, I consider the effect of more distant neighbours (in particular, second nearest neighbours). I introduce the conditional probability distribution of second-nearest neighbour distances for a given first-neighbour distance, and calculate it within a simple continuous model. If the first nearest neighbour is found unusually far from our chosen dopant, then it is quite likely to find the second nearest neighbour immediately. Furthermore, I calculate the exchange interaction distribution for the first and second nearest-neighbours using the Herring-Flicker asymptotic form. I find, in accordance with above conclusion, that the more distant the first neighbour becomes, the larger is the ratio of the exchange interaction from second nearest neighbour to that from the first nearest neighbour. For comparison I also calculate the dipole-dipole interaction distribution. In the region of densities and separations we are interested in for practical devices, the dipole-dipole interaction from the second-nearest neighbour is actually larger than the exchange interaction.

One place where the effect of a second-nearest neighbour may limit the performance of the system is in the readout of the qubits. In order to understand these limitations, I consider the time evolution of a small group of spins including a qubit atom, a control atom, and a second-neighbour 'spectator'. Flip-flop processes between the spectator spin and the qubit and/or control limit the time available for readout. These processes can be suppressed by a strong magnetic field or by using a control atom with a different g factor from the qubit atom. Based on this calculation of the spin dynamics, I go on to simulate within the rotating wave approximation a full optical readout process, by performing a calculation in which the control-qubit system interacts with a single-frequency laser and considering two possible laser frequencies. Readout method I (in which the laser is tuned to a transition between $M_S = \pm 3/2$ states) is superior to method II (laser tuned to $M_S = \pm 1/2$ states) because the exchange interactions have less effect in the $\pm 3/2$ case. I also investigate the effect of spontaneous decay on the readout process: I find that if the spontaneous decay rate is too large, the readout may fail. On the other hand, many fluorescence photons must be emitted from the excited state of the control within one spin-flip time.

The second part concerns an alternative system for spin-controlled information processing (including possibly quantum information processing): the magnetic transition-metal phthalocyanines. I have concentrated on two systems: copper(II)-phthalocyanine (Cu(II)Pc) and manganese (II)-phthalocyanine (Mn(II)Pc).

Our theoretical study of the magnetism of CuPc dimers includes both a model Green's function calculation, to understand the roles of the competing processes, and *ab initio* DFT broken-symmetry calculations using the Gaussian package and the hybrid functional B3LYP to obtain more quantitative information. The results agree approximately with the magnetic measurements recently performed on this material. From the model calculation I find that the dominant exchange contribution comes from the so-called indirect exchange mechanism, which involves the transfer of a spin-polarized electron-hole pair from one molecule to another; this transfer depends on the stacking angle. The magnitude of the exchange interaction found from Gaussian DFT calculations roughly agrees with the experiment.

I also describe some model calculations of Mn(II)Pc dimers that include two competing processes: super-exchange and indirect exchange. In this case, because of the competition between the two and lack of knowledge of some of the intra-molecule interactions, it is more difficult to quantify the exchange interaction through the model calculation. I also describe a DFT calculation of this exchange interaction, which is ongoing.

Based on what I have described above, in future theoretical studies could be performed on several other things.

- First-principles calculations of the exchange interaction in a true periodic crystal structure, rather than in dimers. This could be done, for example, by using the CRYSTAL code [88]

- Benchmark calculations should be carried out against more accurate quantum chemistry approaches, e.g. coupled-cluster methods.

- Other organic systems, for example fused biporphyrins or the purely organic magnetic systems such as the TEMPO radical, could be investigated.

- Exchange couplings in electronically excited states could be calculated, opening the way to full optical control of the magnetic interactions.

Part IV

ACKNOWLEDGEMENT

12. ACKNOWLEDGEMENT

First of all, I would like to thank my supervisors Professor Andrew. Fisher and Dr. Tony Harker for continuous careful guidance, enlightening discussion, and kind encouragement throughout the past three years.

Many thanks to Professor Marshall Stoneham for giving me a chance to join Basic Technology project.

Many thanks to Thornton Greenland for the help and discussions about the Gaussian fitting, three-centre calculations, and readout calculations.

I really appreciate the help from Dr. Andy Kerridge when I did the perturbation theory and DFT calculations for the exchange in CuPc dimer.

I would like to thank Dan Wheatley for introducing many useful softwares.

Many thanks to Professor Gabriel Aeppli and Dr. Sandrine Heutz for giving me the chance to do some theoretical work on their new organic system.

Many thanks to all the members in London Centre for nano-technology.

At the end I thank my wife Ms. Yan Chen for her endless support to me.

BIBLIOGRAPHY

[1] Michael A. Nielsen and Isaac L. Chuang, 2000, *Quantum computation and quantum information.*, Cambridge University Press.

[2] D. G. Corey, A. F. Fahmy, and T. F. Havel,1997, *Ensemble quantum computing by NMR spectroscopy. Proc. Nat. Acad. Sci. USA*, 94,1634.

[3] I. L. Chuang, N. Gershenfeld, and M. Kubinec, 1998, *Experimental implementation of fast quantum searching.* Phys. Rev. Lett., 18,3408.

[4] Jones J. A., 2003, *Robust quantum information processing with techniques from liquid-state NMR Phil. Trans. R. Soc. Lond.* A 361, 1429.

[5] Ch. Ross *et al*, 1999 *Quantum state engineering on an optical transition and decoherence in a paul trap. Phys. Rev. Lett 83, 4713*

[6] Ferdinand Schmidt-Kaler, Hartmut Hffner, Mark Riebe,*et al.*, 2003, *Realization of the CiracZoller controlled-NOT quantum gate*, Nature 422, 408.

[7] P. Krger, A. Haase, M. Andersson and J. Schmiedmayer,2005, *Quantum Information Processing with Neutral Atoms on Atom Chips*,Quantum Information Processing, Second, Rev. and Enl.Edition.

[8] Kane, B. 1998, *A silicon-based nuclear spin quantum computer.* Nature 393, 133.

[9] Toshimasa Fujisawa, Tjerk H. Oosterkamp, Wilfred G. van der Wiel, *et al.*,1998, *Spontaneous Emission Spectrum in Double Quantum Dot Devices* Science 282, 932.

[10] T. Hayashi *et al.*, 2003, *Coherent manipulation of electronic states in double quantum dot. Phys. Rev. Lett 91 226804.*

[11] Divincenzo, 1996, Topics in quantum computers. In *Mesoscopic electron transport*, (ed. L. L. Sohn, L. P. Kowenhoven and G. Schon). Dordrecht: Kluwer.

[12] Nakamura, Y. Pashkin, Yu. A. and Tsai,J. 1999, *Coherent control of macroscopic quantum states in a single-Cooper-pair box.*, Nature, 398, 786.

[13] Vion,D., Aassime, A., Cottet, A.,et al. 2002, *Manipulating the quantum state of an electrical circuit.*, Science 296, 886.

[14] Mooij, J. E., Orlando, T.P., Levitov,L., et al. 1999, *Josephson persistent-current qubit.* Science 285, 1036.

[15] M Steffen, M. Ansmann, *et al.*, 2006, *Measurement of the Entanglement of Two Superconducting Qubits via State Tomography*, Science, 313, 1423.

[16] N. Katz, M. Ansmann, Radoslaw C. Bialczak,*et al.*, 2006, *Coherent state evolution in a superconducting qubit from partial-collapse measurement*,Science 312, 1498.

[17] T. Yamamoto, Yu. A. Pashkin, O. Astafiev, *et al.*,2003, *Demonstration of conditional gate operation using superconducting charge qubits*, Nature 425, 941.

[18] J. R. Petta, A. C. Johnson, J. M. Taylor, *et al.*, 2006, *Charge and spin manipulation in a few-electron double dot*, Physica E 34, 42-46.

[19] M. Mitic, S.E. Andresen, C. Yang,*et al.*, 2005, *Single atom Si nanoelectronics using controlled single-ion implantation*, Microelectronic Engineering, 78-79,279.

[20] Daniel Loss and David P. DiVincenzo, 1997, *Quantum computation with quantum dots*, Phys. Rev. A 57, 120.

[21] Almeida Murphy, T., Pawlick, Th., Weidinger, A., et al. 1996, *Observation of atomlike nitrogen in nitrogen-implanted solid C_{60}.* Phys. Rev. Lett. 77, 1075.

[22] Barnes, C., Shilton, J. and Robinson, A., 2000, *Quantum computation using electrons trapped by surface acoustic waves.* Phys. Rev. B 62, 8410.

[23] A.M.Stoneham, A.J.Fisher and P.T.Greenland,2003 *Optical driven silicon-based quantum gates with potential for high-temperature operation.* J.Phys.: Condensed Matter,15,L447.

[24] A.M.Stoneham, A.J.Fisher and P.T.Greenland,2002, *A gate for quantum information processing British Patent Application No 02050011.0(filed 4 March 2002)*

[25] A.M.Stoneham, 1975, *Theory of Defects in Solids (Oxford University Press).*

[26] N.Itoh and A.M.Stoneham, 2001, *Materials Modification by Electronic Excitation (Cambridge University Press).*

[27] F. Jelezko, I. Popa, A. Gruber, C. Tietz, and J. Wrachtrup, *et al.*, 2002 *Single spin states in a defect center resolved by optical spectroscopy*, Appl. Phys. Lett. 81, 2160.

[28] Forrest T. Charnock and T. A. Kennedy, 2001, *Combined optical and microwave approach for performing quantum spin operations on the nitrogen-vacancy center in diamond*, Phys. Rev. B 64, 041201.

[29] Theodore G. Castner, Jr., 1963, *Raman Spin-Lattice Relaxation of Shallow Donors in Silicon* , Phys. Rev. 130, 58.

[30] F Bridges, G Davies, J Robertson and A M Stoneham, 1990, *The spectroscopy of crystal defects: a compendium of defect nomenclature*, J. Phys.: Condens. Matter, 2, 2875.

[31] Luttinger J.M. and Kohn W., 1955, *Motion of Electrons and Holes in Perturbed Periodic Fields* , *Phys. Rev.* 97, 869

[32] C. Kittel and A.H. Mitchell, 1954, *Theory of donor and acceptor states in Silicon and Germanium*, *Phys. Rev.* 96, 1488.

[33] W. Kohn, J. M. Luttinger, 1955, *Theory of donor states in Silicon*, Physical Review, 98, 915.

[34] H. Barry Bebb, 1967, *Application of quantum defect techniques to photonization of Impurities in semiconductors*, *J. Phys. Chem. Solids*, 28, 2087

[35] John C. Slater, 1963, *Quantum theory of molecules and solids*

[36] Conyers Herring and Michael Flicker, 1964, *Asymptotic exchange coupling of two hydrogen atoms.*

[37] Hubert M. James and Albert Sprague Coolidge, 1933, *The ground state of the hydrogen molecule. J. Chem. Phys.* 1,825.

[38] W. Kolos, N. Wolonectz, 1965, *Potential energy for* $X\,\Sigma_g^+$, $b\Sigma_u^+$, *and* $C\Pi_u$ *states of Hydrogen molecule. J. Chem. Phys.* 43, 2429.

[39] K. Andres, *et al.*, 1981, *Low-temperature magnetic susceptibility in Si:P in the nonmetal region.*, *Phys. Rev. B* 24,244.

[40] Bellita Koiller, *et al.*, 2002, *Strain effect on silicon donor exchange: Quantum computer achitechture consideration Phys.Rev B*, 66, 115201

[41] Ari. Mizel, Daniel. A. Lidar, 2004, *Three-and four-body interactions in spin-based quantum computers Phys.Rev Lett.*, 92, 077903

[42] Boys. S. F, 1950, *Electronic Wave Functions. I. A General Method of Calculation for the Stationary States of Any Molecular System, Proc. Roy. Soc. A* 200, 542.

[43] W. Heisenberg, 1928, *Zur Theorie des Ferromagnetismus, Z.Phys*, 49, 619. 1.

[44] P.T.Greenland, 2004, *Some notes on the effective Hamiltonian QIP-04-PTG12-heff.*(unpublished)

[45] M. Roger, etc, 1983, *Magnetism in* He^3, Reviews of Modern Physics, 55, 1

[46] Hertz, 1909, Math. Ann, 67, 387

[47] S. Chandrasekhar, 1943, *Stochastic Problems in Physics and Astronomy*, Rev. Mod. Phys, 15, 1.

[48] Rugar D, *et al.*, 2004, *Single spin detection by magnetic resonance force microscopy*, Nature, 430,329.

[49] Durkan C and Welland ME.,2002, *Electronic spin detection in molecules using Scanning Tunnelling Microscopy assisted electron-spin resonance*, Appl. Phys. Lett. 80,458.

[50] Elzermann JM,*et al.*, *Single shot and read-out of an individual spin in a quantum dot*, Nature, 430, 431.

[51] F. Jelezko, I. Popa, A. Gruber, *et al.*, 2002, *Single spin states in a defect center resolved by optical spectroscopy*,App. Phys. Lett. 81, 2160.

[52] F. Jelezko, T. Gaebel, I. Popa, M. Domhan, A. Gruber, and J. Wrachtrup, 2004, *Observation of Coherent Oscillation of a Single Nuclear Spin and Realization of a Two-Qubit Conditional Quantum Gate*,Phys. Rev. Lett. 93,130501.

[53] F Jelezko, *et al.*, 2004, *Read-out of single spins by optical spectroscopy*, J. Phys.: Condens. Matter 16 R1089.

[54] Blatt, *et al.*, 2003, *Implementation of Deutsch-Jozsa algorithm on an ion-trapped quantum computer*, Nature, 421,48.

[55] Francesco Petruccione, H.-P. Breuer, 2002, *The Theory of Open Quantum Systems*,Oxford University Press.

[56] David Dolphin, 1978, *The porphyrins New York ; London : Academic Press.*

[57] Lionel R. Milgrom, 1997, *The coulors of life (Oxford Universtiy Press).*

[58] W.T.Simpson, 1949, *On the theory of the π-electron system in porphines*, J.Chem.Phys. 17,1218.

[59] H. Kuhn, 1949, *A quantum-mechanical theory of light absorption of organic dyes and similar compounds*, J.Chem.Phys. 17,1198.

[60] R. G. Parr, 1963, *Quantum Theory of Molecular Electronic Transitions*, Benjamin, New York.

[61] Zerner and Gouterman, 1960, Theor. Chim. Acta 4, 44.

[62] Mengsheng Liao, 2005, *et al.,DFT Study of Unligated and Ligated ManganeseII Porphyrins and Phthalocyanines*, Inorg. Chem. 44, 1941.

[63] Bryce E. Williamson, Thomas C. VanCott, *et al.*, 1992, *Determination of the ground state of manganese phthalocyanine in an argon matrix using magnetic circular dichroism and absorption spectroscopy*, J. Am. Chem. Soc. 114, 2412.

[64] G.A.Kumar, J. Thomas *et al.*, 2000, *Optical absorption and emission spectra studies of Phthalocyanine molecules in DMF.*, J. Porphyrins Phthalocyanines,5, 456.

[65] C. G. Barraclough,R. L. Martin, and S. Mitra, 1970, *Paramagnetic Anisotropy, Electric structure, and Ferromagnetism in Spin S=3/2 Manganese (2) Phthalocyanine*, The Journal of Chemical Physics, 53, 1638.

[66] Hiroyuki Yamada, *et al.*, 1998, *Preparation and magnetic properties of manganese(2) phthalocyanine thin films*, Journal of Chemical Physics, 108, 10256.

[67] Sandrine Heutz, *et al.*, 2006,*Using polymorphism to switch magnetism in molecular films*, to be submmited to Nature.

[68] M. J. Frisch, *et al.*, Gaussian 98 (Gaussian, Inc., Pittsburgh, PA, 1998).

[69] A. D. Becke, 1993, *Density-functional thermochemistry. III. The role of exact exchange.* J. Chem. Phys. 98, 5648.

[70] R. Ditchfield, W. J. Hehre and J. A. Pople, 1970,*Self-consistent molecular-orbital methods.IX. An extended Gaussian-type basis for molecular-orbital studies of organic molecules* J. Chem. Phys. 54, 724.

[71] P. W. Anderson, 1959, *New Approach to the Theory of Superexchange Interactions.* Phys, Rev, 115, 2-13.

[72] M. A. Ruderman and C. Kittel,1954, *Indirect exchange coupling of nuclear magnetic moments by conduction electrons*, Phys. Rev. 96, 99.

[73] N. Bloembergen and T. J. Rowland, 1955, *Nuclear spin exchange in solid:* Tl^{203} *and* Tl^{205} *magnetic resonance in Thallium and Thallic oxide*, Phys, Rev, 97, 1679.

[74] P. S. Bagus, B. I. Bennett, 1974,*Singlet-triplet splittings as obtained from the X-scattered wave method: A theoretical analysis*, Int. J. Quantum. Chem. 9, 143.

[75] Ziegler. T, *et al.*, 1977,Theo. Chim. Acta. 43,261.

[76] Louis Noodleman, 1980, *Valence bond description of antiferromagnetic couplings in transition metal dimers.* J. Chem. Phys. 74, 5737-5743.

[77] Yamaguchi. K, 1988, *et al.*,,*Antiferromagnetic spin couplings between iron ions in ironsulfur clusters. A localized picture by the spin vector model*,Chem. Phys. Lett. 164, 210.

[78] Andrea di Matteo and Vincenzo Barone, 1999, *Development and Validation of Effective Computational Strategies for the Study of Metal Nitroxide Complexes*, J. Phys. Chem. A. 103,7676.

[79] Richard L. Martin and Francesc Illas, 1997 *Antiferromagnetic Exchange Interactions from Hybrid Density Functional Theory*, Phys. Rev. Lett.79,1539.

[80] Fransesc Illas, *et al.*, 2000, *Magnetic coupling in biradicals, binuclear complexes, and wide-gap insulators: a survey of ab initio wave function and density functional theory approaches.* Theo. Chem. Acc, 104, 265-272.

[81] A. D. Becke, 1988,*Density funcitonal exchange-energy approximation with correct asymptotic behavior.* Phys. Rev. A 38, 3098.

[82] C. Lee, W. Yang and R. G. Parr,1988, *Development of the Colle-Salvetti correlation-energy formula into a functional of the electron density.* Phys. Rev. B 37, 785-789.

[83] John A. Pople, Martin Head-Gordon, and Douglas J. Fox, 1989, *Gaussian-1 theory: A general procedure for prediction of molecular energies*, J.Chem.Phys, 90, 5622.

[84] Eliseo Ruiz, Pere Alemany *et al.*, 1996, *Toward the Prediction of Magnetic Coupling in Molecular Systems: Hydroxo- and Alkoxo-Bridged Cu(II) Binuclear Complexes*, J. Am. Chem. Soc. 119,1297.

[85] C. Adamo,V. Barone,*et al.*,2006, *Comment on "About the calculation of exchange coupling constants using density-functional theory: The role of the self-interaction error" [J. Chem. Phys. 123, 164110 (2005)]*, J.Chem.Phys.124, 107101.

[86] K. Burke, J. P. Perdew and Y. Wang, in *Electronic Density Functional Theory: Recent Progress and New Directions,Ed.* J. F. Dobson, G. Vignale and M. P. Das (Plenum, 1998).

[87] S. H. Vosko, L. Wilk and M. Nusair, 1980, *Accurate spin-dependent electron liquid correlation energies for local spin density calculations: a critical analysis*, Canadian J. Phys. 58, 1200-1211.

[88] C.Pisani, *Quantum-Mechanical Ab-initio calculation of the Properties of Crystalline Materials, Lecture Notes in Chemistry*, Vol. 67, Spinger Verlag, Heidelberg, 1996.

[89] L. Pisani, J. A. Chan, B. Montanari and N. M. Harrison, 2007, *Electronic structure and magnetic properties of graphitic ribbons*, Phys. Rev. B 75, 064418.